

In compliance with the
Canadian Privacy Legislation
some supporting forms
may have been removed from
this dissertation.

While these forms may be included
in the document page count,
their removal does not represent
any loss of content from the dissertation.

ENHANCEMENT OF THE FINITE DIFFERENCE TIME DOMAIN TECHNIQUE
AND ITS APPLICATION TO MICROWAVE DEVICES

By

NAGULA THARMA SANGARY, M.Eng. (McMaster University)

A Thesis
Submitted to the School of Graduate Studies
in Partial Fulfillment of the Requirements
for the Degree
Doctor of Philosophy

McMaster University
© Copyright by
Nagula T. Sangary,
February 2003

Doctor of Philosophy (2003)
(Electrical and Computer Engineering)

McMaster University
Hamilton, Ontario

TITLE: Enhancement of the Finite Difference Time Domain
Technique and its Application to Microwave Devices.

AUTHOR: Nagula T. Sangary, B.Sc. (Texas A&M University),
M.Eng. (McMaster University)

SUPERVISOR: Dr. N. Georgieva

SUPERVISORY

COMMITTEE: Dr. P. Jessop
Dr. P. Smith

NUMER OF PAGES: viii, 131

Abstract

Most intriguing and complicated scientific problems are solved with the aid of high-speed computers. Advancements in computer technology in conjunction with lower cost of computers have tremendously contributed to this effort. In this thesis, adopting the same philosophy, we explore the solutions to electromagnetic problems using a numerical technique, namely the Finite Difference Time Domain technique. This technique requires large computer resources: specifically, fast computing and large amount of computer memory. Therefore, our developments of this numerical technique focus on reducing both the computational time and computer memory requirements.

A unique line-of-sight (LoS) approximation to the equivalence principle, which is a far more efficient alternative to the standard equivalence principle, is introduced. This includes the theory associated with the LoS equivalence, the examination of the error due to the approximation, and the verification with simulations and measurements. The FDTD method is formulated by discretizing Maxwell's curl equations over a finite volume and approximating the derivatives with central difference approximations. The error due to this approximation depends directly on the method of implementation such as the non-uniform mesh. An experimental investigation of the numerical error due to the non-uniform FDTD technique is presented. In the area of active and passive microwave devices, a unique method of incorporating the device equations into the FDTD algorithm is presented. The measurement and simulation results verify this method. In addition to device analysis, new antennas for the use in Personal Communication Systems are presented. The finale to the thesis is an electromagnetic simulation software package that incorporates all the new techniques developed in the course of this work.

To the memory of my parents

Veerasingham Tharmasangary

(1923-1992)

and

Kanaganayakie Tharmasangary

(1928-2000)

Acknowledgements

I would like to thank my supervisor Dr. Natalia Georgieva and the other members of my committee Dr. P.M. Smith and Dr. P. Jessop, for their considerable patience and assistance over the excessively long gestation period of this thesis. I would like to express my gratitude to Dr. Natalia Georgieva, for her help in turning my ramblings into an actual thesis and for sacrificing her personal time that was spent in very valuable discussions.

Needless to say, that I am very grateful to all of my friends and colleagues at Research In Motion. Specially, I like to thank my friend Perry for listening patiently and giving me valuable feedback. I like to acknowledge some of my friends Enrique, Yihong and Geyi for engaging in helpful discussions in the theories of Electromagnetism. In addition, I like to thank my friends and former colleagues at McMaster University and Nortel Networks for providing the needed support.

Special thanks goes to my wife Christalyn and son Joshua. My wife's patience, encouragement, love, and guidance were essential for me to stay in course during the PhD program. My son's affection, his captivating smiles and the playtime he sacrificed were of enormous help.

My undying gratitude to my late parents, whose passion and dedication for education inspired me to peruse this PhD program. I like to thank my parents in-law, Rev. and Mrs. W. R. Aruliah, for filling the void left behind by my parents in providing the continued support. Finally, I would like to thank all our family members, specially, my uncle and aunt, Dr. and Mrs. K. Gnananathan, for their interest and support throughout my PhD program. Most of all, I thank God for everything in my life.

Contents

1. INTRODUCTION	1
1.1 Overview	1
1.2 Scope of the Thesis	4
1.3 Contribution to Technology	4
1.4 Thesis Outline	6
2. FDTD FORMALISM	7
2.1 Introduction	7
2.2 Non-uniform FDTD Formalism	8
2.3 Absorbing Boundaries	14
2.3.1 Perfectly Matched Layer (PML) Boundary	15
2.3.2 First Order Absorbing Boundary	18
2.4 Excitation Source	20
2.4.1 Gaussian Pulse Excitation Source Implementation	21
2.4.2 Sinusoidal Excitation Source Implementation	26
2.6 Summary	27
2.7 References	27
3. RADIATION PATTERN WITH NEW EQUIVALENCE	29
3.1 Introduction	29
3.2 Theoretical Discussion	31
3.2.1 Line of Sight Equivalence Principle	32
3.2.2 Standard Equivalence Principle	32
3.2.3 Surface Current Densities and Vector Potentials	35

3.2.4 Field at Point-of-Symmetry	38
3.2.5 The LoS Edge Currents.....	41
3.2.5.1 The Edge Currents Contribution to the Far-field.....	50
3.3 Application of the LoS Approach to a Practical Problem.....	58
3.3.1 A Numerical Example of the Application of LoS Approximation.....	60
3.3 Practical Examples with the LoS Approximation Using the FDTD Method	63
3.4.1 The Dielectric-covered Dipole Antenna.....	63
3.4.2 The Patch Antenna.....	66
3.5 Summary.....	68
3.8 References.....	69
 4. ANTENNA ANALYSIS WITH THE FDTD METHOD.....	71
4.1 Introduction.....	71
4.2 The Coaxial Transmission Line.....	72
4.3 Mobile Unit Antennas.....	74
4.3.1 Coupled Patch Antennas.....	74
4.3.2 Printed Sleeve Antenna.....	77
4.3.3 Sandwich Antenna	79
4.4 Window Antennas.....	82
4.5 Base Station Antennas	84
4.5.1 Co-Planer Patch Antenna.....	84
4.5.2 Printed Loop Antenna.....	86
4.6 Summary.....	87
4.7 References.....	87
 5. ERROR ANALYSIS OF THE NON-UNIFORM FDTD METHOD	88
5.1 Introduction.....	88
5.2 Second Order Error Analysis	90
5.2.1 Error Analysis with Homogeneous Dirichlet Boundary Conditions	91

5.2.2 Error Analysis with the Perfect Dispersive Boundary Conditions	95
5.2.3 Error Analysis with PML Absorbing Boundary Conditions.....	98
5.2.4 Error Analysis with Imperfectly Absorbing Boundary Conditions	99
5.3 Summary	100
5.5 References.....	101
6. MICROWAVE DEVICE ANALYSIS WITH FDTD METHOD	103
6.0 Introduction.....	103
6.1 Implementation of Device Current and Voltage.....	104
6.2 Formalism of Current and Voltage in the FDTD Method	106
6.2.1 Resistors.....	110
6.2.2 Capacitors	111
6.2.3 Inductors	111
6.2.4 Diodes	112
6.2.1 Voltage/Current Sources.....	113
6.2.4 Transistor	114
6.3 Simulation of Microwave Devices.....	115
6.4 Comparison between Single and Dual Source Excitation	127
6.5 Summary.....	129
6.6 References.....	129
7. CONCLUSION.....	130

Chapter 1

Introduction

1.1 Overview

The complexity of electromagnetic problems has forced many researchers and engineers to resort to their numerical solutions. With the advancement of modern computers, numerical analysis techniques are becoming more efficient and popular. Numerical solutions by their very nature are approximate solutions to the real problem, thus they have some inherent disadvantages relating to numerical and discretization approximation as well as long computational time. In many cases, the accuracy of the solution is linked to the length of computational time. The reduced accuracy in numerical solutions is due to the discrete value approximations of continuous functions and the finite element representations of the physical structures. The long computational time is mainly due to the large amount of computations needed when simulating electrically large structure. There are a number of techniques used in computational electromagnetism and among them the most popular are: the Method of Moments, the Finite Element Method, the Transmission Line Method, approximate analytical solutions, and the Finite Difference Time Domain method. Each one of these techniques has its advantages and disadvantages. The Finite Difference Time Domain technique is one of the most efficient and it is the subject of this study.

In the Finite Difference Time Domain (FDTD) technique, in the spatial domain and the time domain, finite differences are used to approximate the derivatives of Maxwell's equations. The FDTD technique does not involve any problem specific

functions such as the Green's function in the Method of Moments, nor does it require the solution to a system of equations as in the case of the Finite Element Method and the Transmission Line Method.

The FDTD technique, which is more versatile than other methods, seems to be the best technique for solving difficult electromagnetic problems. Despite this advantage, the FDTD technique has few drawbacks, namely the large memory and CPU time requirement. It is a common understanding that any new development of the FDTD technique should address these concerns and this thesis exclusively does that.

The implementation of FDTD technique in the spatial domain can be of different mesh forms, they are the uniform, the non-uniform, and the curvilinear. Each one of these forms has its benefits and drawbacks. An exhaustive investigation shows that the non-uniform FDTD technique is the most efficient algorithm with regards to CPU time and memory requirements. The non-uniform FDTD technique allows the use of fewer cells in the spatial domain to discretize a given problem. However if not implemented properly, it will affect the accuracy of the solution. Nevertheless, a compromise is achievable between the degree of non-uniformity and the accuracy of the solution. On the other hand, although the uniform mesh provides better accuracy, it results in an increased number of cells and longer computational time. Similarly, in the case of the curvilinear form, because of better conformity to the physical structure, one can obtain good accuracy using the same number of cells as in non-uniform case, however the difficulty in the implementation of this technique and the additional memory required for the storage of variables overshadow its advantage. This thesis contains techniques that improve the accuracy and the efficiency of the non-uniform FDTD method.

In this thesis, a new equivalence approach to the calculation of radiation pattern of antenna is introduced. Using this new equivalence approach, the computational time required for antenna pattern calculation can be reduced significantly.

In some analyses, specifically in the case of antenna analysis, it is important to have free space medium surrounding the antenna. In the case of the FDTD technique, the requirement of free space results in the use of a large mesh that takes more memory. The requirement for the mesh size can be reduced by truncation of the mesh along with the

use of absorbing boundaries that emulate free space. There are a number of Absorbing Boundary Conditions (ABC). Among them, the most accurate one is the Perfectly Matched Layer (PML) absorbing boundary, and the simplest one is the first-order absorbing boundary. In antenna analysis, the PML absorbing boundary condition is used for the cases that require high accuracy and the first order ABC are used for faster computation.

When using the FDTD technique for analysing the performance of antennas, it was found that the optimum configuration is the non-uniform mesh for fast computation, the PML for accuracy, and the “line-of-sight” equivalence principle for a faster calculation of radiation patterns. In some cases, even with a good absorbing boundary condition, the truncation of the mesh does not give an accurate representation of the real problem. These and other effects are discussed in Chapter 4. In designing antennas, only one’s imagination sets the limit on the shape and size of antennas, but the analysis becomes difficult when unconventional structures are used. In this respect, the FDTD technique becomes the most effective method of solving antenna problems and the demonstration of this is in Chapter 4.

The analysis of microwave/millimetre wave integrated circuits using electromagnetic simulators is becoming popular. This is because of the miniaturization of integrated circuits, which puts various devices in close proximity and the resulting effect is a strong electromagnetic field interaction between the devices. This effect is detrimental to high-speed circuits that need to operate over a wide frequency range. Therefore, the inference of this is that the EM simulations of high-speed circuits should be in three dimensions and the computation should be with measured circuit parameters used in the device model. Commonly used circuit simulators in the industry such as the Agilent Momentum and ADS, Ansoft HFSS, IE3D, and H-Spice do not address all the pertinent issues and Chapter 6 provides detailed discussion on this.

1.2 Scope of the Thesis

The aim of the thesis is to improve the FDTD technique in its application to microwave/millimetre wave integrated circuits. To this effect, it includes the implementation of new techniques to decrease the computational time, the FDTD error analysis, and the integration of device equations into the FDTD algorithm. All examples in the thesis are commonly used devices such as antennas, passive devices, active devices, and waveguide structures. In conjunction with the application of the FDTD technique, this thesis contains new antennas for the application in Personal Communication System and a detailed error analysis of the non-uniform FDTD technique.

1.3 Contribution to Technology

This thesis contains several contributions towards the advancement of electrical engineering and electromagnetic simulations, and they are as follows.

- (1) Introduction of a new equivalence principle to EM theory in antenna analysis.
- (2) Applications of the FDTD technique to passive and active microwave/millimetre wave components (devices).
- (3) Error analysis of the non-uniform FDTD technique.
- (4) Development of new antennas for the use in Personal Communication Systems.
- (5) Development of EM simulation tool, which is of commercial standard.

With the advancements in wireless communications, the demand for new antennas is on the rise. With this, there is a need for analysis tools that can accurately determine the performance of new antennas. In this thesis, we evaluate the performance of a few new antennas using the FDTD technique. The antennas used for the evaluation meet the typical requirements for Personal Communications Systems (PCS) and Cellular Systems (Cell), namely, they are physically small, they have attractive appearance and good gain. Since the frequency bands for PCS and Cell are at the lower end of the

microwave spectrum, the size requirement forces one to deviate from the traditional antenna design methods and adhere to more elaborate antenna shapes. In view of this, with new antenna shapes, the analysis also has to take an approach different from the techniques such as the Method of Moments, the Finite Element Method or other similar techniques. In this respect, the FDTD technique, which models the entire antenna structure along with the free space surrounding the antenna proves to be versatile.

This thesis contains the introduction of a new equivalence principle namely the “Line-Of-Sight Equivalence” for the calculation of radiation patterns of antennas. A different approach to calculate radiated fields from antennas when using numerical techniques is proposed and verified. The developments in Chapter 3 show that one can obtain the radiation pattern of an antenna with only one type of surface current that is in the line of sight from the observation point provided that certain conditions are satisfied. This procedure can be easily adapted to the calculation of radiation patterns of antennas with the Finite Difference Time Domain (FDTD) technique.

Errors in the FDTD techniques are mainly due to two factors. One is the discretisation of the physical structure, and the other is the finite difference approximation of the derivatives. Using a finer mesh with longer computational time reduces the first type of error. The second type of error, which is due to the finite difference approximation, needs separate treatment. In the FDTD algorithm, the use of uniform mesh in both time and space results in second-order accuracy. This conclusion follows directly from the fact that central finite differences are used. However, with a uniform mesh the power of the FDTD method is lost when one tries to analyse devices that involve fine details in certain regions and less detail in others. In such problems the use of a non-uniform mesh can increase the algorithm efficiency, because a fine mesh can be used in the region of detailed structure and a coarse mesh elsewhere. The use of non-uniform mesh results in less computer memory and faster computational time. However, this improvement comes at the expense of accuracy. At first glance, one might conclude that the non-uniform scheme has only first order accuracy. However, the presentation in Chapter 5 shows that when applied appropriately this scheme has global second order accuracy.

The implementation of the FDTD technique to microwave/millimetre wave integrated circuits is very challenging and it needs a few special considerations. These are; the proper integration of time-domain device equations into the FDTD algorithm, the use of more than one cell to represent the device in the physical structure, and the stability of the device equation used in the FDTD algorithm. Chapter 6 contains discussions on these and other issues.

In this thesis an EM simulation package is developed. The simulation package uses a user-friendly Matlab interface and the main engine of this simulation package includes all the advancements in the FDTD technique outlined in this thesis.

1.4 Thesis Outline

This thesis consists of seven chapters. Chapter 1 introduces the FDTD technique and the challenges encountered in its implementation. Chapter 2 gives the general formalism needed for the FDTD simulation such as: the non-uniform FDTD technique, the Perfectly Match Layer (PML) absorbing boundary, first order absorbing boundary and the excitation sources. In addition, Chapter 2 includes a detailed analysis of the Gaussian pulse excitation. Chapter 3 is dedicated to the theoretical development, and the experimental verification of the Line-Of-Sight equivalence principle and its application in obtaining radiation patterns.

Chapter 4 concerns the antenna analysis using the FDTD method and special considerations given to the modelling aspect of antennas, specifically the incorporated feed structure. In addition, Chapter 4 includes new antennas that have application in PCS wireless systems. Chapter 5 covers the error analysis of non-uniform orthogonal FDTD algorithm with focus on second order error analysis. Chapter 6 includes a detailed discussion on the application of the FDTD method to passive and active devices. In addition, Chapter 6 contains a unique implementation of device modelling using two contact (source) points. Simulation and measurement results are provided. Finally, Chapter 7 gives the conclusion to the thesis. Each chapter includes its respective reference section.

Chapter 2

FDTD Formalism

2.1 Introduction

As in every numerical technique, in the FDTD technique, the method of implementation plays a major role in its accuracy and effectiveness. Since the FDTD technique models physical structures, the mapping of the spatial coordinates to the FDTD algorithm is crucial. This mapping begins with the selection of a mesh or cell format that best represents the continuous space in discrete form. There are many such representations and among them, the most commonly used ones are the uniform, the non-uniform, and the curvilinear grids (or mesh). For our analysis, we have chosen the non-uniform mesh. In-depth discussions of its properties are contained in this and the subsequent chapters. In addition to the choice of mesh, as was stated in Chapter 1, the choice of absorbing boundary condition (ABC) also has a significant influence on the accuracy of the technique. In our analysis, we have used the most accurate one and the most common one, namely the perfectly matched layer (PML) absorbing boundary condition and the first order absorbing boundary condition, respectively. This chapter contains the formalism needed for the implementation of the non-uniform FDTD technique, the PML ABC, the first order ABC and the calculation of the return loss with specific excitation sources.

The choice of a non-uniform mesh over the uniform and the curvilinear are due to some of its advantages such as fewer cells, shorter computational time, simplicity of implementation and structural conformity to many practical problems. However, these

advantages come with a slight compromise in the accuracy, and the discussion of this is included Chapter 5.

In the application of absorbing boundary conditions, the PML and the first order ABC have their advantages and drawbacks. The first order ABC does not perform very well when the absorbing boundaries encounter oblique incident waves and the degree of accuracy depends on the obliqueness. However, one main advantage of the first order ABC is that it utilises the same field components used in the FDTD algorithm, and thus has no additional memory requirements. On the other hand, the PML gives accurate results for cases with oblique incident waves in applications such as obtaining the radiation pattern of an antenna, or in the analysis of waveguide structures that do not have a TEM mode. Unlike the first order ABC, the PML requires additional variables for the field components in the absorbing boundary regions, as well as additional computations with each time step. This results in an increase in the computational time for the PML ABC.

2.2 Non-uniform FDTD Formalism

The derivation of the formalism for the non-uniform FDTD algorithm begins with Maxwell's equations in isotropic media and they can be of integral [4] or differential form [1]. In addition, the non-uniform FDTD formalism is a particular case of the non-orthogonal FDTD, [3]-[6]. In the FDTD technique, the convenience of implementation dictates the choice between the integral and the differential form, and we choose the differential form. The differential form of Maxwell's equations in a homogeneous, source-free region is:

$$\frac{\partial \vec{E}}{\partial t} = \frac{1}{\epsilon} \nabla \times \vec{H} \quad (2.1)$$

$$\frac{\partial \vec{H}}{\partial t} = -\frac{1}{\mu} \nabla \times \vec{E} \quad (2.2)$$

In rectangular coordinates, these two differential equations are as follows.

$$\frac{\partial E_x}{\partial t} = \frac{1}{\varepsilon} \left[\frac{\partial H_z}{\partial y} - \frac{\partial H_y}{\partial z} \right] \quad (2.3)$$

$$\frac{\partial E_y}{\partial t} = \frac{1}{\varepsilon} \left[\frac{\partial H_x}{\partial z} - \frac{\partial H_z}{\partial x} \right] \quad (2.4)$$

$$\frac{\partial E_z}{\partial t} = \frac{1}{\varepsilon} \left[\frac{\partial H_y}{\partial x} - \frac{\partial H_x}{\partial y} \right] \quad (2.5)$$

$$\frac{\partial H_x}{\partial t} = -\frac{1}{\mu} \left[\frac{\partial E_z}{\partial y} - \frac{\partial E_y}{\partial z} \right] \quad (2.6)$$

$$\frac{\partial H_y}{\partial t} = -\frac{1}{\mu} \left[\frac{\partial E_x}{\partial z} - \frac{\partial E_z}{\partial x} \right] \quad (2.7)$$

$$\frac{\partial H_z}{\partial t} = -\frac{1}{\mu} \left[\frac{\partial E_y}{\partial x} - \frac{\partial E_x}{\partial y} \right] \quad (2.8)$$

These partial differential equations can be approximately put into discrete form with non-uniform spacing in the spatial and uniform spacing in the time domain. The non-uniform FDTD algorithm follows the reference scheme proposed by Yee [1] in which the electric field components are located along the edges of the cells, and the magnetic field components are located on the faces of the cells. This follows the leapfrog scheme given in [1], and Figures 2.1, 2.2 and 2.3 show the locations of the field components.

In order to define the field components in discrete form, a new notation is adopted, as defined in equations (2.9) and (2.10).

$$E_{x,y,z}^n(i, j, k) = E_{x,y,z}(x_i, y_j, z_k, t_n) \quad (2.9)$$

$$H_{x,y,z}^{n+\frac{1}{2}}(i, j, k) = H_{x,y,z}\left(x_i - \frac{\Delta x_i}{2}, y_j - \frac{\Delta y_j}{2}, z_k - \frac{\Delta z_k}{2}, t_n + \frac{\Delta t}{2}\right) \quad (2.10)$$

where

$$\Delta x(i) = x_i - x_{i-1}, \quad \Delta y(j) = y_j - y_{j-1}, \quad \Delta z(k) = z_k - z_{k-1}, \quad \Delta t = t_n - t_{n-1}. \quad (2.11)$$

In the definitions, the superscripts n and $(n+1/2)$ represent field components at time $n\Delta t$ and $(n+1/2)\Delta t$ respectively. For reasons of stability and simplicity, choice of term Δt in the FDTD algorithm is chosen it to be a constant. The value of this constant is determined by the stability condition as given in [1], and it is defined as $\Delta t \leq \Delta d_{\min}/c$, where Δd_{\min} is the smallest value of Δx_i , Δy_j or Δz_k , and c is the speed of light in free space. With these definitions, equation (2.3) in discrete form becomes

$$E_x^{n+1}(i, j, k) = E_x^n(i, j, k) + \frac{\Delta t}{\varepsilon} \left[\frac{H_z^{n+\frac{1}{2}}(i, j, k) - H_z^{n+\frac{1}{2}}(i, j-1, k)}{[\Delta y(j-1) + \Delta y(j)]/2} - \frac{H_y^{n+\frac{1}{2}}(i, j, k) - H_y^{n+\frac{1}{2}}(i, j, k-1)}{[\Delta z(k-1) + \Delta z(k)]/2} \right] \quad (2.12)$$

Similarly for E_y and E_z the equations (2.4) and (2.5) become

$$E_y^{n+1}(i, j, k) = E_y^n(i, j, k) + \frac{\Delta t}{\varepsilon} \left[\frac{H_x^{n+\frac{1}{2}}(i, j, k) - H_x^{n+\frac{1}{2}}(i, j, k-1)}{[\Delta z(k-1) + \Delta z(k)]/2} - \frac{H_z^{n+\frac{1}{2}}(i, j, k) - H_z^{n+\frac{1}{2}}(i-1, j, k)}{[\Delta x(i-1) + \Delta x(i)]/2} \right] \quad (2.13)$$

$$E_z^{n+1}(i, j, k) = E_z^n(i, j, k) + \frac{\Delta t}{\varepsilon} \left[\frac{H_y^{n+\frac{1}{2}}(i, j, k) - H_y^{n+\frac{1}{2}}(i-1, j, k)}{[\Delta x(i-1) + \Delta x(i)]/2} - \frac{H_x^{n+\frac{1}{2}}(i, j, k) - H_x^{n+\frac{1}{2}}(i, j-1, k)}{[\Delta y(j-1) + \Delta y(j)]/2} \right] \quad (2.14)$$

The expressions for H_x , H_y and H_z are derived in the same way and they are:

$$H_x^{n+\frac{1}{2}}(i, j, k) = H_x^{n-\frac{1}{2}}(i, j, k) - \frac{\Delta t}{\mu} \left[\frac{E_z^n(i, j+1, k) - E_z^n(i, j, k)}{\Delta y(j)} - \frac{E_y^n(i, j, k+1) - E_y^n(i, j, k)}{\Delta z(k)} \right] \quad (2.15)$$

$$H_y^{n+\frac{1}{2}}(i, j, k) = H_y^{n-\frac{1}{2}}(i, j, k) - \frac{\Delta t}{\mu} \left[\frac{E_x^n(i, j, k+1) - E_x^n(i, j, k)}{\Delta z(k)} - \frac{E_z^n(i+1, j, k) - E_z^n(i, j, k)}{\Delta x(i)} \right] \quad (2.16)$$

$$H_z^{n+\frac{1}{2}}(i, j, k) = H_z^{n-\frac{1}{2}}(i, j, k) - \frac{\Delta t}{\mu} \left[\frac{E_y^n(i+1, j, k) - E_y^n(i, j, k)}{\Delta x(i)} - \frac{E_x^n(i, j+1, k) - E_x^n(i, j, k)}{\Delta y(j)} \right] \quad (2.17)$$

The field component points for a large mesh are shown in Figure 2.1, and further definitions of these terms are shown in detail in Figures 2.2 and 2.3.

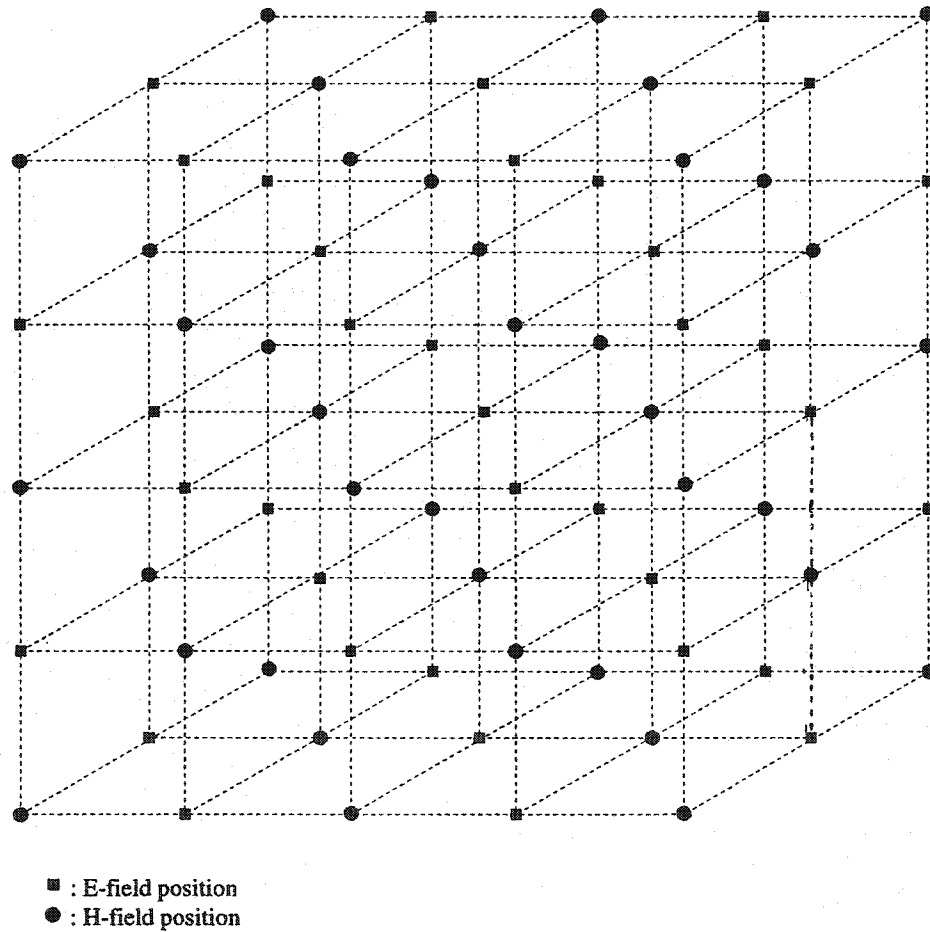


Figure 2.1: Typical mesh with field points.

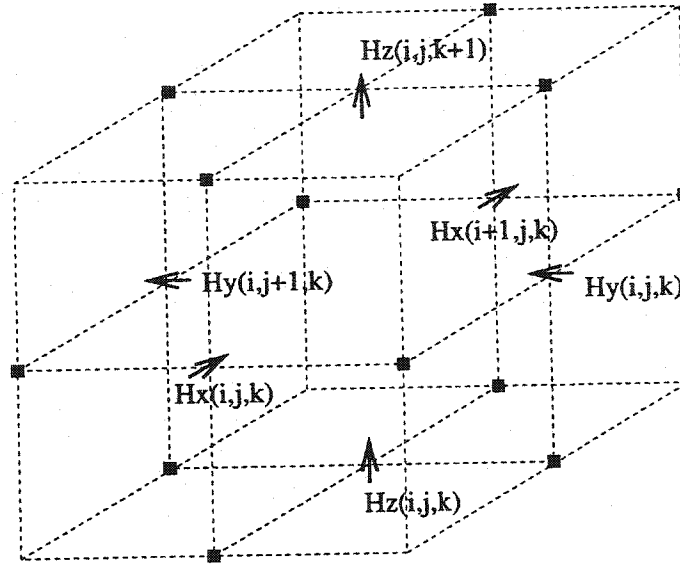


Figure 2.2: H-field points for a single cell.

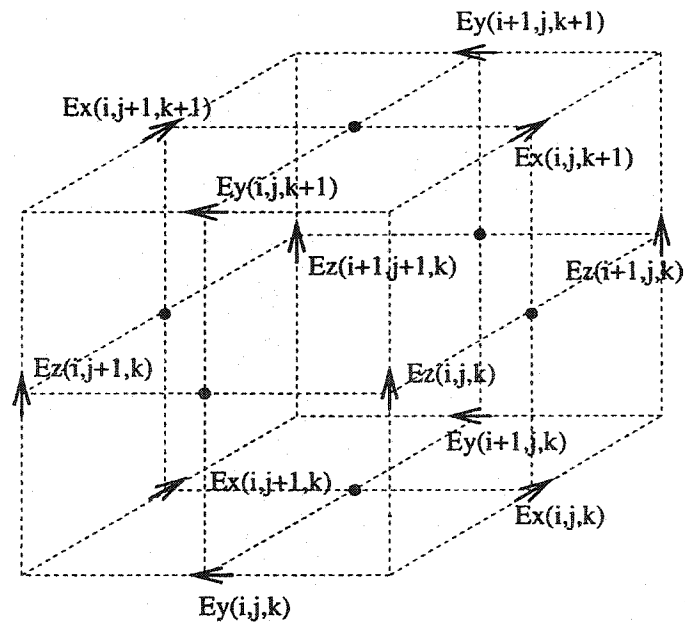


Figure 2.3: E-field points for a single cell.

2.3 Absorbing Boundaries

As in all electromagnetic problems, the boundary conditions are vital in obtaining a solution to the problem, and numerical solutions are no exception to this requirement. In numerical solutions such as in the FDTD technique, in order to obtain the solution to a given problem within a reasonable computational time, the truncation of the space and time domains within some boundary is an essential requirement. The truncation in the time domain is specific to the excitation source; the discussion on this is in Section 2.4. On the other hand, the truncation in space is somewhat complicated, and there are numerous implementation techniques available with varying degrees of accuracy and computational time. Among the various absorbing boundary conditions (ABC's), the most popular ones are the perfectly matched layer (PML) ABC, the first order ABC, and the second order ABC.

The PML ABC, being a mathematical model for absorbing boundaries, uses values for properties such as permittivity and permeability that are not physically realisable, but are highly effective in absorbing electromagnetic waves. When used with the FDTD technique, it is applied to the outer cells of the FDTD mesh. The first order boundary condition is also applied to the outer cells of the FDTD mesh and it is applied only to one layer of the surface. The first order ABC is applied with an assumption of normal incidence to the absorbing boundaries. The accuracy of the absorption, the computational time and the complexity of implementation determine the selection of the type of ABC. In the FDTD technique, we are primarily interested in antenna and microwave device analysis.

In antenna analysis, the FDTD computational domain must be enclosed in an absorbing box in order to simulate a free space environment surrounding the antenna. An easy first order ABC can be used in evaluating antennas and from this, the return loss of the antenna (S_{11}) is obtained with sufficient accuracy. However, in order to obtain the radiation pattern, the first order ABC is not helpful, and a more accurate ABC is necessary. The radiation pattern is obtained from the physical currents enclosing the antenna, and these are sensitive to the ABC when the ABC does not describe "free space" accuracy. A second order

ABC is more accurate: it absorbs plane waves impinging at two different angles; it is, however more difficult to implement, and computation takes longer than with the first order ABC; in summary the performance of the second order ABC does not compensate for its drawbacks. In this respect, the use of PML ABC seems ideal, because of its simplicity and flexibility. The PML regions are modelled as lossy media, in contrast with the other regions, and the performance of PML ABC can be improved by adding more layers. More layers lead to better absorption, the number of layers depends on the accuracy one wants to achieve and the physical dimensions and shape of the antenna. In our antenna analysis, we used a number of cells ranging from five to ten, depending on the antenna.

2.3.1 Perfectly Matched Layer (PML) Boundary

We present a formulation of the Perfectly Matched Layer (PML) that interfaces with the non-uniform FDTD scheme. To implement the PML, we split each field component E_i into two sub-components E_{ij} and E_{ik} . The same procedure applies to the magnetic field vector. With this the discretized form of Maxwell's curl equation in the PML region becomes

$$E_{xy}^{n+1}(i, j, k) = A_y(j) E_{xy}^n(i, j, k) + B_y(j) \left[\frac{H_z^{n+\frac{1}{2}}(i, j, k) - H_z^{n+\frac{1}{2}}(i, j-1, k)}{[\Delta y(j-1) + \Delta y(j)]/2} \right] \quad (2.18)$$

$$E_{xz}^{n+1}(i, j, k) = A_z(k) E_{xz}^n(i, j, k) + B_z(k) \left[\frac{H_y^{n+\frac{1}{2}}(i, j, k-1) - H_y^{n+\frac{1}{2}}(i, j, k)}{[\Delta z(k-1) + \Delta z(k)]/2} \right] \quad (2.19)$$

$$E_{yx}^{n+1}(i, j, k) = A_x(i) E_{yx}^n(i, j, k) + B_x(i) \left[\frac{H_z^{n+\frac{1}{2}}(i-1, j, k) - H_z^{n+\frac{1}{2}}(i, j, k)}{[\Delta x(i-1) + \Delta x(i)]/2} \right] \quad (2.20)$$

$$E_{yz}^{n+1}(i, j, k) = A_z(k) E_{yz}^n(i, j, k) + B_z(k) \left[\frac{H_x^{n+\frac{1}{2}}(i, j, k) - H_x^{n+\frac{1}{2}}(i, j, k-1)}{[\Delta z(k-1) + \Delta z(k)]/2} \right] \quad (2.21)$$

$$E_{zx}^{n+1}(i, j, k) = A_z(k) E_{yz}^n(i, j, k) + B_z(k) \left[\frac{H_x^{n+\frac{1}{2}}(i, j, k) - H_x^{n+\frac{1}{2}}(i, j, k-1)}{[\Delta z(k-1) + \Delta z(k)]/2} \right] \quad (2.22)$$

$$E_{zy}^{n+1}(i, j, k) = A_y(j) \times E_{zy}^n(i, j, k) + B_y(j) \left[\frac{-H_x^{n+\frac{1}{2}}(i, j-1, k) + H_x^{n+\frac{1}{2}}(i, j, k)}{[\Delta y(j-1) + \Delta y(j)]/2} \right] \quad (2.23)$$

$$H_{xy}^{n+\frac{1}{2}}(i, j, k) = C_y(j) H_{xy}^{n-\frac{1}{2}}(i, j, k) - D_y(j) \left[\frac{E_z^n(i, j+1, k) - E_z^n(i, j, k)}{\Delta y(j)} \right] \quad (2.24)$$

$$H_{xz}^{n+\frac{1}{2}}(i, j, k) = C_z(k) H_{xz}^{n-\frac{1}{2}}(i, j, k) - D_z(k) \left[\frac{E_y^n(i, j, k) - E_y^n(i, j, k+1)}{\Delta z(k)} \right] \quad (2.25)$$

$$H_{yx}^{n+\frac{1}{2}}(i, j, k) = C_x(i) H_{yx}^{n-\frac{1}{2}}(i, j, k) - D_x(i) \left[\frac{E_x^n(i, j, k+1) - E_x^n(i, j, k)}{\Delta z(k)} \right] \quad (2.26)$$

$$H_{yz}^{n+\frac{1}{2}}(i, j, k) = C_z(k) H_{yz}^{n-\frac{1}{2}}(i, j, k) - D_z(k) \left[\frac{E_z^n(i, j, k) - E_z^n(i+1, j, k)}{\Delta x(i)} \right] \quad (2.27)$$

$$H_{zx}^{n+\frac{1}{2}}(i, j, k) = C_x(i) H_{zx}^{n-\frac{1}{2}}(i, j, k) - D_x(i) \left[\frac{E_y^n(i+1, j, k) - E_y^n(i, j, k)}{\Delta x(i)} \right] \quad (2.28)$$

$$H_{zy}^{n+\frac{1}{2}}(i, j, k) = C_y(j) H_{zy}^{n-\frac{1}{2}}(i, j, k) - D_y(j) \left[\frac{-E_x^n(i, j, k) + E_x^n(i, j+1, k)}{\Delta y(j)} \right] \quad (2.29)$$

The total field components are given as $E_x = E_{xy} + E_{xz}$, $E_y = E_{yx} + E_{yz}$, $E_z = E_{zx} + E_{zy}$, and $H_x = H_{xy} + H_{xz}$, $H_y = H_{yx} + H_{yz}$, $H_z = H_{zx} + H_{zy}$. With m representing the coordinate indices x , y and z , l_m representing the length inside the PML region, the coefficients $A_m(l_m)$, $B_m(l_m)$, $C_m(l_m)$, and $D_m(l_m)$ are given as follows:

$$A_m(l_m) = \exp \left[\frac{-\sigma_m^*(l_m) \Delta t}{\epsilon} \right] \quad (2.30)$$

$$B_m(l_m) = - \frac{\exp \left[\frac{-\sigma_m^*(l_m) \Delta t}{\epsilon} \right] - 1}{\sigma_m^*(l_m)} \quad (2.31)$$

$$C_m(l_m) = \exp \left[\frac{-\sigma_m^*(l_m) \Delta t}{\mu} \right] \quad (2.32)$$

$$D_m(l_m) = - \frac{\exp \left[\frac{-\sigma_m^*(l_m) \Delta t}{\mu} \right] - 1}{\sigma_m^*(l_m)} \quad (2.33)$$

The field components inside the PML region undergo strong attenuation in all directions due to the presence of electric and magnetic losses, σ_m , σ_m^* , respectively. In the PML region, the condition $\sigma_m / \epsilon = \sigma_m^* / \mu$ is observed. Thus, the phase velocity of a plane wave in the PML region is the same as the velocity in the computational volume truncated by the PML region. Here ϵ and μ are the permittivity and permeability of the loss free computational volume. This ensures that there is no reflection at the interface of the computational and the PML regions. The decay is so rapid that the conventional time

integration of the FDTD method is not useful; therefore, in the PML region the time integration is exponential [8].

In theory, a single absorbing layer would be sufficient. However, in practical application of the FDTD technique, the discretization of the PML region requires several layers. In antenna analysis, the absorbing square box that consists of matched layers at the walls encloses the mesh that defines the antenna.

2.3.2 First Order Absorbing Boundary

Applications for which the outside boundary need not accurately represent free space, can utilize the first order absorbing boundary condition. In the first order ABC [11], the absorption is accurate only for waves that are incident perpendicular to the surface. Unlike the PML ABC, the first order ABC directly applies to the field components as shown below.

For the first yz surface

$$E_y^n(1, j, k) = E_y^{n-1}(2, j, k) + \frac{c\Delta t - \Delta x(1)}{c\Delta t + \Delta x(1)} \left[E_y^n(2, j, k) - E_y^{n-1}(1, j, k) \right] \quad (2.34)$$

$$E_z^n(1, j, k) = E_z^{n-1}(2, j, k) + \frac{c\Delta t - \Delta x(1)}{c\Delta t + \Delta x(1)} \left[E_z^n(2, j, k) - E_z^{n-1}(1, j, k) \right] \quad (2.35)$$

where c is the speed of light in free space and the other variables are as defined earlier.

For the second yz surface, with the total number of cells in the x -direction being nx ,

$$E_y^n(nx, j, k) = E_y^{n-1}(nx-1, j, k) + \frac{c\Delta t - \Delta x(nx)}{c\Delta t + \Delta x(nx)} \left[E_y^n(nx-1, j, k) - E_y^{n-1}(nx, j, k) \right] \quad (2.36)$$

$$E_z^n(nx, j, k) = E_z^{n-1}(nx-1, j, k) + \frac{c\Delta t - \Delta x(nx)}{c\Delta t + \Delta x(nx)} \left[E_z^n(nx-1, j, k) - E_z^{n-1}(nx, j, k) \right] \quad (2.37)$$

For the other four surfaces, the equations are as follows:

First xz surface

$$E_x^n(i, 1, k) = E_x^{n-1}(i, 2, k) + \frac{c\Delta t - \Delta y(1)}{c\Delta t + \Delta y(1)} \left[E_x^n(i, 2, k) - E_x^{n-1}(i, 1, k) \right] \quad (2.38)$$

$$E_z^n(i, 1, k) = E_z^{n-1}(i, 2, k) + \frac{c\Delta t - \Delta y(1)}{c\Delta t + \Delta y(1)} \left[E_z^n(i, 2, k) - E_z^{n-1}(i, 1, k) \right] \quad (2.39)$$

Second xz surface, with the total number of cells in the y-direction being ny ,

$$E_z^n(i, ny, k) = E_z^{n-1}(i, ny - 1, k) + \frac{c\Delta t - \Delta y(ny)}{c\Delta t + \Delta y(ny)} \left[E_z^n(i, ny - 1, k) - E_z^{n-1}(i, ny, k) \right] \quad (2.40)$$

$$E_x^n(i, ny, k) = E_x^{n-1}(i, ny - 1, k) + \frac{c\Delta t - \Delta y(ny)}{c\Delta t + \Delta y(ny)} \left[E_x^n(i, ny - 1, k) - E_x^{n-1}(i, ny, k) \right] \quad (2.41)$$

First xy surface

$$E_x^n(i, j, 1) = E_x^{n-1}(i, j, 2) + \frac{c\Delta t - \Delta z(1)}{c\Delta t + \Delta z(1)} \left[E_x^n(i, j, 2) - E_x^{n-1}(i, j, 1) \right] \quad (2.42)$$

$$E_y^n(i, j, 1) = E_y^{n-1}(i, j, 2) + \frac{c\Delta t - \Delta z(1)}{c\Delta t + \Delta z(1)} \left[E_y^n(i, j, 2) - E_y^{n-1}(i, j, 1) \right] \quad (2.43)$$

Second xy surface, with the total number of cells in the z-direction being nz ,

$$E_y^n(i, j, nz) = E_y^{n-1}(i, j, nz - 1) + \frac{c\Delta t - \Delta z(nz)}{c\Delta t + \Delta z(nz)} \left[E_y^n(i, j, nz - 1) - E_y^{n-1}(i, j, nz) \right] \quad (2.44)$$

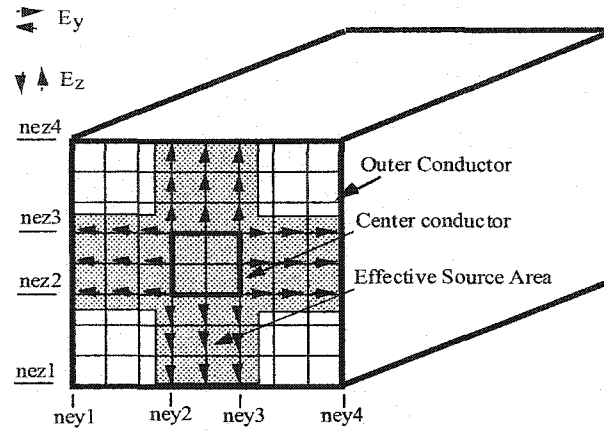
$$E_x^n(i, j, nz) = E_x^{n-1}(i, j, nz - 1) + \frac{c\Delta t - \Delta z(nz)}{c\Delta t + \Delta z(nz)} \left[E_x^n(i, j, nz - 1) - E_x^{n-1}(i, j, nz) \right] \quad (2.45)$$

It can be easily seen from the formalism of the first order absorbing boundary condition that the absorption is valid for electromagnetic waves with wave fronts parallel to each surface. If the absorbing boundaries are placed far from the structure by a distance of several wavelengths, then the wave front is somewhat spherical in nature and the error due to imperfect absorption is minimal.

2.4 Excitation Source

In FDTD simulations, applying a known excitation source and observing the response in the desired domain gives the time or frequency response of the structures under investigation. The excitation source can be applied at any part of the structure with different forms of feed structures such as coaxial, microstrip or stripline transmission lines, and the source can be of different types such as sinusoidal, Gaussian or step functions. In the cases of antennas and integrated circuits, when using a rectangular grid, the feed is typically coaxial or microstrip. The excitation source can be either Gaussian pulse or sinusoidal. The choice of excitation source depends on the specific application. It was found that the Gaussian pulse is the best excitation source for obtaining a wide band frequency response, whereas sinusoidal excitation is suitable for certain specific applications such as obtaining the radiation pattern of an antenna or for the analysis of waveguide structures. The correct choice of excitation and the implementation of the source in the structure are both important for accurate simulation. The best method of implementing an excitation source is to use a square coaxial structure. The TEM mode in a coaxial line is expressed more accurately than in microstrip or strip-line structures due to the simpler field distribution in the transverse plane. In addition, uniform cells can be used within the coaxial feed to minimise error, and the excitation source is applied in a cross-sectional plane in the coax, thus giving a quasi-TEM mode in the coax. The field component of the excitation source is assumed uniform from the centre conductor to the outer conductor. Figure 2.4 shows the typical excitation source field-points. The field components E_y and E_z in the y and z directions are constant and

are equal to the excitation source. They are implemented in the shaded region as shown in Figure 2.4.



Cross Sectional View of the Coaxial Feed Line

Figure 2.4: Excitation source field configuration.

Among the various types of excitation source, the most useful one is the Gaussian pulse (as stated above). In addition to providing a wide frequency response, the Gaussian pulse can be used to derive all the essential device parameters needed for device analysis, such as return loss, insertion loss, antenna gain or pattern, antenna efficiency, surface current, etc. Due to its wide range of applications, the Gaussian pulse has been adopted as the primary excitation source for all our analyses using the FDTD technique. Details of its implementation are addressed in Section 2.4.1.

2.4.1 Gaussian Pulse Excitation Source Implementation

A Gaussian pulse is defined in time domain using parameters such as the pulse width (T), time offset (t_0), amplitude (A) and pulse duration (t_{dur}). These parameters are shown in

Figure 2.5. The Gaussian pulse as a function of time is [12].

$$g_1(t) = A \exp \left[\frac{-(t - t_0)^2}{2T^2} \right] \quad (2.46)$$

The Gaussian pulse in discrete time steps Δt is

$$E_{exc}(n) = A \exp \left[\frac{-(n \Delta t - t_0)^2}{2T^2} \right] \quad (2.47)$$

The choice of values and the effects of the parameters such as the amplitude (A) and time-offset (t_0) are straightforward. However, the choice and effects of the pulse width (T) and the truncation (duration) of the Gaussian pulse are not straightforward and need detailed analysis.

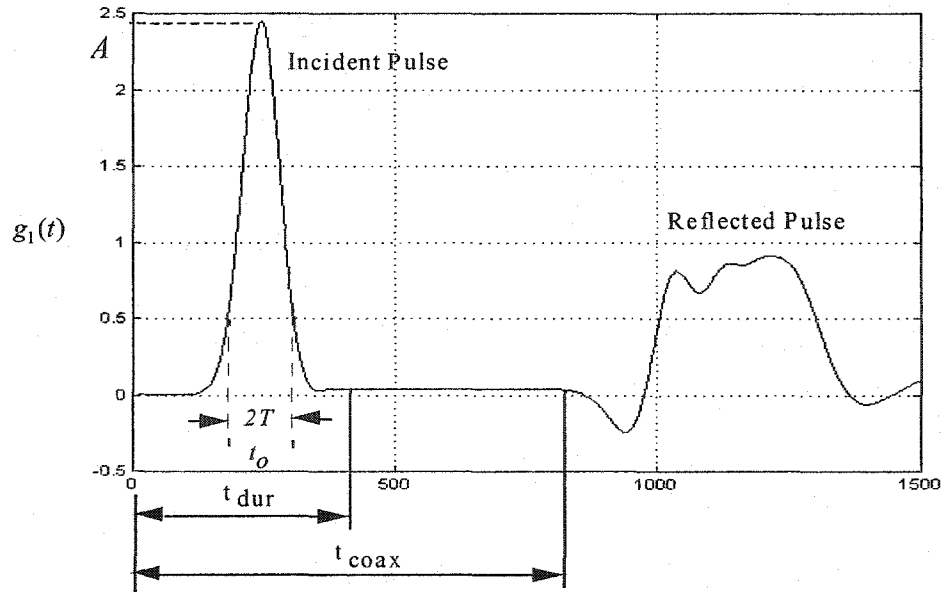


Figure 2.5 A typical excitation waveform.

In most practical problems, we are interested in obtaining the frequency response of circuits or devices. Thus, we begin the investigation with the frequency domain representation of the Gaussian pulse. Using Fourier transform, the frequency domain function of equation (2.46) is [12]:

$$G_1(f) = AT\sqrt{\pi} \exp\left[\frac{-(2\pi fT)^2}{4}\right] \exp(-j2\pi ft_0) \quad (2.48)$$

It is observed in (2.48) that the frequency response of the Gaussian function has the same shape as in the time domain. The peak of the Gaussian pulse is at zero on the frequency axis. If we are interested in obtaining a return loss of a circuit or a device, then the spectral (frequency) content in the Gaussian pulse should have sufficient power (spectral content) for a given value of return loss. If we were to examine the spectral content as a function of frequency then we can write the following:

$$D = -20 \log_{10} \left(\exp\left[\frac{-(2\pi fT)^2}{4}\right] \right) \quad (2.49)$$

Here, D is the return loss that is normalized to DC (i.e. maximum value occurs at DC and it is $AT\pi$). Now we could define the frequency limit in terms of pulse width (T) and return loss (D) as

$$f_H = \frac{1}{\pi T} \sqrt{\frac{2.303 D}{20}} \quad (2.50)$$

From equation (2.50), one may infer that for good accuracy over a wide frequency range, the pulse width has to be small and there is no limitation for the pulse width. However, in practical situations there are lower and upper limits for the pulse width. The

length of the simulation time sets the upper limit and the discrete time step sets the lower limit of the pulse width.

In addition to the pulse width limit, there are limits on the minimum duration of the pulse. In the FDTD algorithm, if the Gaussian pulse is terminated prematurely at t_x from the initiation of the pulse as shown in Figure 2.6, then the error in the simulation is significant.

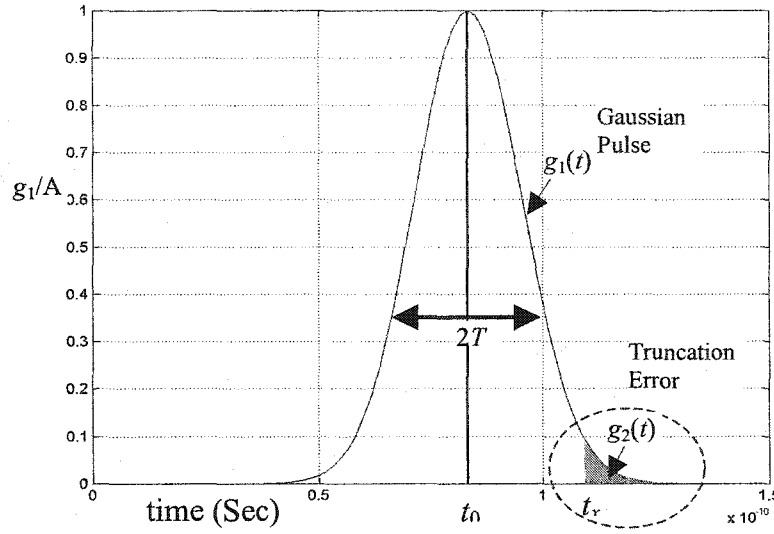


Figure 2.6: Gaussian pulse and truncated error function.

The truncation error shown in Figure 2.6 is defined as

$$g_2(t) = \begin{cases} A \exp\left[\frac{-(t-t_0)^2}{2T^2}\right] & t > t_x \\ 0 & t \leq t_x \end{cases} \quad (2.51)$$

We define ξ in the frequency domain as the ratio of the magnitudes of the truncation error to that of the Gaussian pulse as

$$\xi = 20 \cdot \log_{10} \frac{|G_2(f)|}{|G_1(f)|} \quad (2.52)$$

where $G_1(f)$ and $G_2(f)$ are the Fourier transforms of the functions $g_1(f)$ and $g_2(f)$,

respectively. We evaluate this function numerically using Fast Fourier Transform (FFT). The graphical representation of equation (2.52) for an example with different t_x with a fixed pulse width (T) of 10 ps is shown in Figure 2.7. The figure contains the return loss error ξ for values of the pulse truncation from the centre of the pulse ($t_x - t_0$) of 10 ps, 20 ps, and 30 ps.

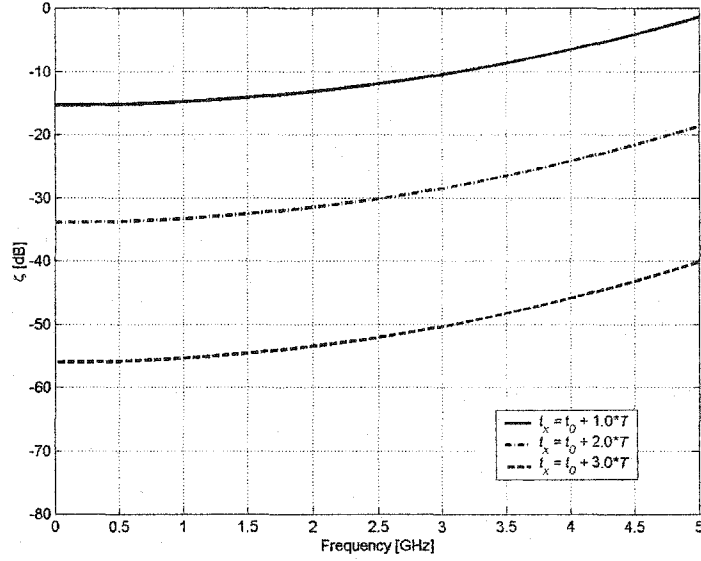


Figure 2.7: Return Loss for premature termination of pulse.

It is evident from Figure 2.7 that the truncation error plays a major role in the overall simulation. It is extremely difficult to derive a relationship between the three parameters: the pulse width, the return loss and the pulse duration. Therefore, for each simulation problem one needs to pay attention to all three parameters. For example, if we are interested in a practical problem for which the return loss needs to be less than -40 dB over a frequency range of up to 5GHz, then the minimum pulse duration has to be

$$t_{dur} \geq 3t_0 + \frac{d_{sp} \sqrt{\epsilon_r}}{c} \quad (2.53)$$

where d_{sp} is the distance of the S_{11} sampling point from the beginning of the coaxial feed line

and ϵ_r is the dielectric constant within the coaxial feed.

The length of the coaxial feed for a Gaussian pulse is calculated with the assumption of TEM mode in the feed:

$$\text{Coax length}_{\min} = \frac{c}{\sqrt{\epsilon_r}} \frac{t_{dur}}{2} \quad (2.54)$$

In the FDTD algorithm, initially the pulse is reflected at the excitation point within the coaxial feed, and at time t_{dur} an absorbing boundary is turned on while the source and the reflecting plane are turned off. Figure 2.8 shows the side view of the coaxial feed.

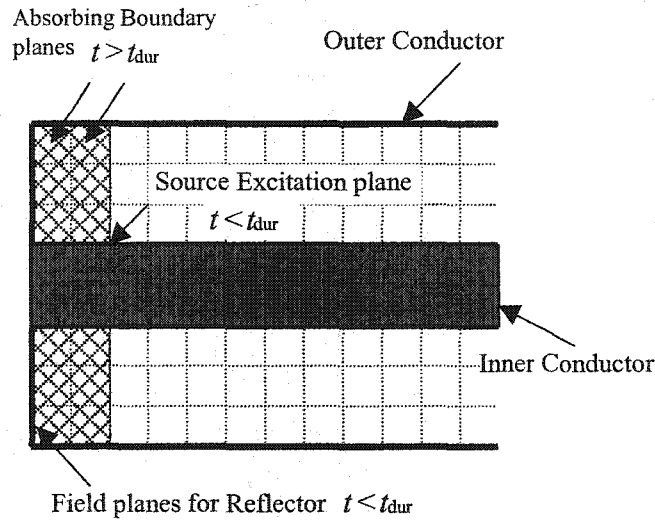


Figure 2.8: The cross sectional view of the coaxial feed.

2.4.2 Sinusoidal Excitation Source Implementation

In sinusoidal excitation source, the parameters that define the source do not affect the simulation results significantly. However, there is a limit on the high frequency; this is due to the maximum cell size. In a sinusoidal source, only two parameters need to be set and

they are the amplitude and the frequency. The selection of these parameters is straightforward.

$$E_{exc}(n) = A \sin(2\pi f_0 n \Delta t) \quad (2.55)$$

where f_0 is the frequency, Δt is the time step in the FDTD algorithm and A is the amplitude of the source. In the simulation algorithm, for sinusoidal excitation, the reflector plane is continuously on.

2.6 Summary

In this chapter the formalism needed for the implementation of non-uniform FDTD applications is developed. The formulas given are utilised in computer simulations, which demonstrate applications to antennas and integrated circuits. In addition, this chapter contains descriptions of the absorbing boundary conditions and excitation source. The discussions on the excitation source demonstrate that some parameters are crucial to the accuracy of the FDTD simulation; they are the pulse width, the duration, and the coaxial line length. The detailed error analysis of these parameters was presented in this chapter.

2.7 References

- [1] K.S. Yee, "Numerical solution of initial boundary value problems involving Maxwell's equation in isotropic media," *IEEE Trans. Antennas Propagation*, vol.14, pp. 302-307, 1966.
- [2] R. Holland, "Finite-difference solution of Maxwell's equation in generalized non-orthogonal coordinates," *IEEE Trans. Nucl. Sci.*, vol. NS-30, No.6, 1983.

- [3] M. Fusco, "FDTD algorithm in curvilinear coordinates," *IEEE Trans. Antennas Propagation*, vol. AP-38, pp. 76-88, 1990.
- [4] J.F. Lee, R. Palandech, and R. Mittra, "Modelling three dimensional discontinuities in waveguide using non-orthogonal FDTD algorithm," *IEEE Trans. Microwave Theory and Tech.*, vol. MTT-40, pp. 346-352, 1992.
- [5] A. Taflove and K. R. Umashankar, "Review of FD-TD numerical modelling of electromagnetic wave scattering and radar cross section," *Proc. IEEE*, Vol. 47, pp. 421-435, 1986.
- [6] R. Holland, "Finite-difference time-domain (FDTD) analysis of magnetic diffusion," *IEEE Trans. Electromagn. Comput.*, vol. EMC-36, pp. 32-39, 1994.
- [7] J. Berenger, "A perfectly matched layer for the absorption of electromagnetic waves," *J. Computational Physics*, vol.114, pp. 185-200, 1994.
- [8] N. Sangary, E. Navarro, C. Wu and J. Litva, "Application of Non-uniform FDTD Method to PCS Antennas," *IEEE Antennas and Propagation Symposium*, pp. 1148-1151, 1995.
- [9] G. Dubost and A. Rabbaa, "Analysis of a slot microstrip antenna," *IEEE Trans. Antennas and Propagation*, vol. AP-34, pp.155-163, February 1986.
- [10] Paul C. Cherry and Magdy F. Iskander, "FDTD analysis of high frequency electronic interconnection effects," *IEEE Trans. Microwave Theory and Tech.*, vol.43, pp. 2445-2451, Oct. 1995.
- [11] G. Mur, "Absorbing boundary conditions for the finite-difference approximation of the time domain electromagnetic field equations," *IEEE Trans. Electromagnetic Compat.*, vol. EMC-23, pp. 377-382, 1981.
- [12] F. G. Stremler, *Introduction to Communication Systems*, 2nd ed., Assison-Wesley, pp. 91-92, 1982.

Chapter 3

Radiation Pattern with New Equivalence

3.1 Introduction

The equivalence principle has been widely used in the analysis of the radiation patterns of antennas. It states that an original problem with radiating sources can be transformed into an equivalent problem with equivalent sources on an arbitrary closed surface [1]-[3]. The region of interest in radiation/scattering problems extends to the far zone. It is impossible to accommodate such a region in the computational space of a finite volume numerical technique. With these techniques, the equivalence principle is practically the only means of pattern computations. However, it requires large computational time. In this thesis, we introduce an approximation to the standard equivalence principle, namely the line-of-sight (LoS) equivalence approach to far-field computations. It significantly increases the efficiency of the radiation pattern computations when used in numerical techniques such as the finite-difference time domain (FDTD) method.

The LoS approximation to the equivalence principle considers the source contributions from surface currents that are on the LoS surface only; as well as the currents along the LoS contour. The conditions necessary for the validity of the LoS approximation are: (i) the radiating equivalent sources are in free space and the field is bounded at infinity, and (ii) the observation point is in the far-field region. For every observation point, the virtual closed surface consists of the LoS surface and the 'shadow' surface (see Figure 3.1).

The ‘shadow’ surface can be transformed into an infinite surface supported by the LoS contour. Every straight line, which passes through the observation point and a point on the LoS contour, belongs to this infinite surface (see Figure 3.1). In our approach, the integration of the equivalent currents on the infinite surface is approximated by a contour integration over the edge currents along the LoS contour.

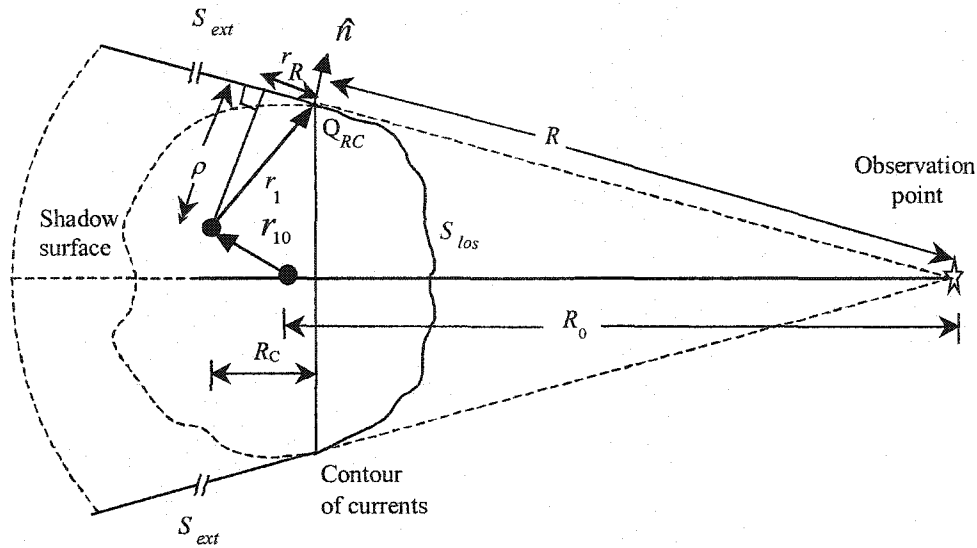


Figure 3.1. Equivalent surfaces and LoS approximation notations.

Over the last half a century, significant attention has been paid to the solutions of diffraction and scattering problems; for example, see [4]-[7]. Most of these references treat the problem of reducing the surface integrals to contour integrals and they are focused mainly on the application to scattering problems. The fundamental difference between a scattering problem and an equivalence problem is that in the former the position vectors of the field on the surface of the scatterer, of the radiating source and of the observer, are known; while in the latter, only two of these position vectors are known: the position vectors of the surface field and of the observer. Therefore, the approximate expressions obtained for the scattering problem cannot be applied directly to the equivalence problem. In [6], the Modified Edge Representation (MER) was proposed and the authors derived a general mathematical

expression for the surface-to-contour transformation using Stroke's theorem. In [6], using field equivalence, an approximate solution is obtained for the surface integral. The derivations in [6] are based on the use of two deformed surfaces (reflection and shadow boundaries), which are needed to obtain near zone accuracies for the diffracted field. Our LoS approximation is developed for far field computations. This allows the shape of the extended surface to be transformed from an infinite conical frustum to an infinite tubular frustum. Unlike in [6], we use an approximation to the open-space potential integral solution rather than diffraction equations such as the Stratton-Chu representation (see [7]). With this approximation, the derivation and implementation of the LoS approach to the radiation problem becomes simple and straightforward. In the literature one could find more metaphorical and less theoretical arguments to the LoS approach, e.g., [12][13][14].

3.2 Theoretical Discussion

In order to highlight the need for a LoS approximation to the equivalence principle, one needs to examine the standard equivalence principle. In the equivalence principle, when obtaining the radiation pattern, the surface currents on the surface enclosing the antenna are used. They are derived from the tangential surface field components. The standard equivalence principle is very useful when used in an isotropic medium for which the free space Green's function can be used in obtaining the radiation pattern [1], [2] and [3]. In general, the calculation of the radiation pattern from the surface currents requires both electric and magnetic currents. However, if the equivalent surface is sufficiently smooth, i.e. the observation point is in the positive normal of the LoS surface, then either one of the surface currents can be used. This concept is exploited in the LoS approach. The LoS approximation to the equivalence principle reduces the computational time and storage memory in the FDTD simulation, thus resulting in an improved efficiency in its application. The theoretical proof for the LoS approximation to the equivalence principle and its

verification with simulations and measurements are presented below.

The first section contains the definition of the LoS equivalence approach and its necessary conditions. The next section contains a brief review of the commonly used equivalence theorem and the expression of the field in terms of the vector potentials. The proceeding section contains the introduction and the derivation of the point-of-symmetry fields. Section 3.2.5 contains detailed discussion on the calculation of the LoS edge currents and supporting examples.

3.2.1 Line of Sight Equivalence Principle

The LoS equivalence principle approximates the commonly used equivalence principle, valid under some special conditions. We give its definition below.

The source contributions from an enclosed surface to an observation point are only from one type of surface currents (electric or magnetic) that are on the line-of-sight surface and the equivalent edge current on the LoS contour.

The conditions necessary for the validity of the LoS principle are:

1. The radiating sources are in free space and the fields are finite at infinity.
2. The observation points satisfy the point-of-symmetry condition (see Section 3.2.4).
3. The size of the enclosing box dictates the accuracy of the LoS approximation.

It follows from the definition of the LoS equivalence approach that the surface current contributions to the far-field are from two distinct sources; one is the sources on the LoS surface and the other is the sources on the LoS contour. The discussion on this is given in Sections 3.2.4 and 3.2.5, respectively.

3.2.2 Standard Equivalence Principle

The equivalence principle is widely used to simplify the original problem with an equivalent one in solving for the radiated field. The derivation of equivalence to a problem

begins with the uniqueness theorem; this and its extension to the equivalence principle are given in [1],[2],[3].

In order to examine the equivalence principle, let us choose a surface that encloses all sources in homogeneity as shown in Figure 3.2. Suppose we are interested only in the field in space outside the enclosed surface, then an equivalent problem can be constructed as shown in Figure 3.3.

The electric and magnetic surface current densities on this surface are:

$$\vec{J}_o^S = \hat{n} \times (\vec{H}_1 - \vec{H}_2) \quad (3.1)$$

and

$$\vec{M}_o^S = -\hat{n} \times (\vec{E}_1 - \vec{E}_2) \quad (3.2)$$

where (\vec{E}_1, \vec{H}_1) and (\vec{E}_2, \vec{H}_2) are electric and magnetic fields outside (region 1) and inside (region 2) the enclosed surface respectively, and \hat{n} is the outward normal vector to the surface.

If we are interested in the field in region 1, then the fields in region 2 could be set to zero without disturbing the field in region 1. With this assumption, the electric and magnetic surface current densities

$$\vec{J}^S = \hat{n} \times \vec{H}_1 \Big|_S = \hat{n} \times \vec{H}^S \quad (3.3)$$

and

$$\vec{M}^S = -\hat{n} \times \vec{E}_1 \Big|_S = -\hat{n} \times \vec{E}^S \quad (3.4)$$

where \vec{E}^S and \vec{H}^S are the electric and magnetic field components on the surface in region 1. In addition, one important point to note is that in the above derivation, the original problem is reduced to an isotropic problem, to which the free-space conditions can be applied.

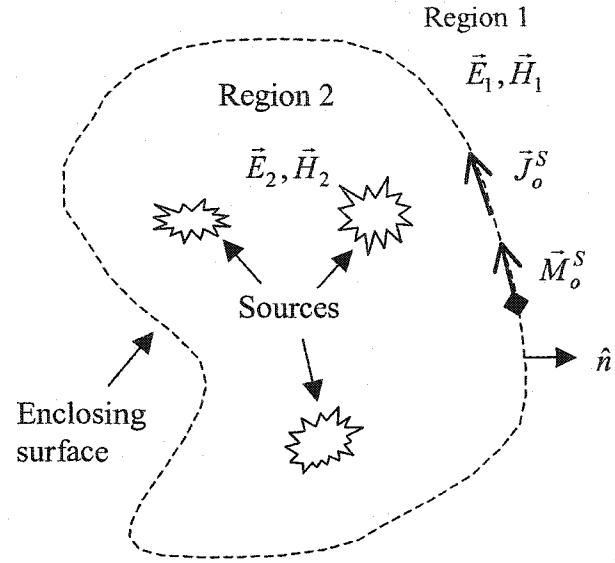


Figure 3.2: Equivalent source in an isotropic medium

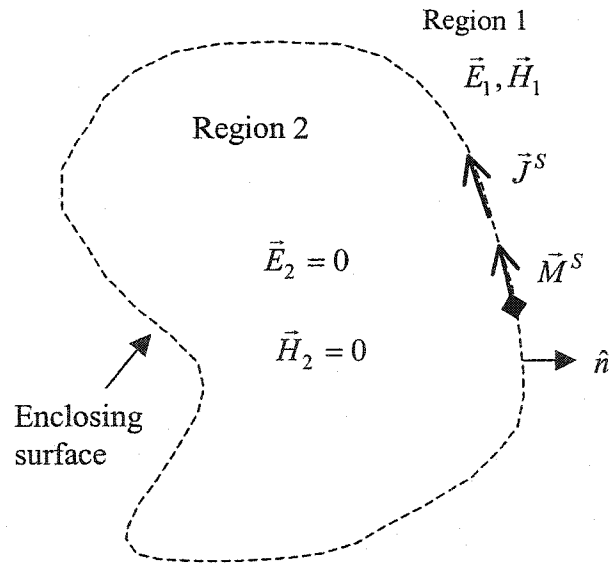


Figure 3.3: Equivalent source in an isotropic medium

3.2.3 Surface Current Densities and Vector Potentials

A commonly used method for calculating the field from radiating sources on a surface is the vector potential approach [1],[2],[11]. Let us assume that sources with current densities \vec{J}^e and \vec{M}^e , which in the limit as area tends to zero are an infinitesimal point sources, are placed at the origin of the coordinate system. For this, the wave equations are

$$\nabla^2 \vec{A}^e + k^2 \vec{A}^e = -\mu \vec{J}^e \quad (3.5)$$

$$\nabla^2 \vec{F}^e + k^2 \vec{F}^e = \varepsilon \vec{M}^e \quad (3.6)$$

where k is the wave number. The solution for the elemental vector potentials of (3.5) and (3.6) is the free space Green's function:

$$\vec{A}^e = \frac{\mu \vec{J}^e}{4\pi} \frac{e^{-jkr}}{r}, \quad (3.7)$$

and

$$\vec{F}^e = \frac{\varepsilon \vec{M}^e}{4\pi} \frac{e^{-jkr}}{r}. \quad (3.8)$$

The principle of superposition holds, thus the total vector potentials are

$$\vec{A} = \iiint_v \vec{A}^e \cdot dv' = \frac{\mu}{4\pi} \iiint_v \frac{e^{-jkr}}{r} \vec{J}^e \cdot dv', \quad (3.9)$$

$$\vec{F} = \iiint_v \vec{F}^e \cdot dv' = \frac{\varepsilon}{4\pi} \iiint_v \frac{e^{-jkr}}{r} \vec{M}^e \cdot dv'. \quad (3.10)$$

If the linear densities of current \vec{J}^e and \vec{M}^e on the surface are \vec{J}^{Se} and \vec{M}^{Se} , then

$$\vec{A} = \frac{\mu}{4\pi} \iint \frac{e^{-jkr}}{r} \vec{J}^{Se} \cdot d\vec{s}' = \iint \vec{A}^{Se} \cdot d\vec{s}' , \quad (3.11)$$

$$\vec{F} = \frac{\varepsilon}{4\pi} \iint \frac{e^{-jkr}}{r} \vec{M}^{Se} \cdot d\vec{s} = \iint \vec{F}^{Se} \cdot d\vec{s} , \quad (3.12)$$

and the general expression for the fields in terms of vector potentials is [3]

$$\vec{E} = -\nabla \times \vec{F} + \frac{1}{j\omega\varepsilon_0} (\nabla \times \nabla \times \vec{A}) \quad (3.13)$$

$$\vec{H} = \nabla \times \vec{A} + \frac{1}{j\omega\mu_0} (\nabla \times \nabla \times \vec{F}) \quad (3.14)$$

We use a rectangular coordinate system, in which the vector wave equation of each vector potential reduces to three decoupled scalar wave equations. The electric and magnetic vector potentials in the rectangular coordinate system are

$$\vec{A}^e = A_x^e \hat{x} + A_y^e \hat{y} + A_z^e \hat{z} \quad (3.15)$$

$$\vec{F}^e = F_x^e \hat{x} + F_y^e \hat{y} + F_z^e \hat{z} \quad (3.16)$$

In order to simplify the further development, we use one component for each of the surface currents, namely J_x^e and M_y^e as elemental current in free space. For these, from (3.7) and (3.8) it can be seen that only A_x^e and F_y^e exist. Without loss of generality, the following derivations can be extended to the other four components J_y^{Se} , J_z^{Se} , M_x^{Se} and M_z^{Se} .

The curls of the electric F_y^e and magnetic A_x^e vector potentials in spherical coordinates are

$$\nabla \times A_x^e \hat{x} = \cos(\theta) \frac{\partial A_x^e}{\partial r} \hat{y} - \sin(\theta) \sin(\phi) \frac{\partial A_x^e}{\partial r} \hat{z} \quad (3.17)$$

$$\nabla \times F_y^e \hat{y} = -\cos(\theta) \frac{\partial F_y^e}{\partial r} \hat{x} + \sin(\theta) \cos(\phi) \frac{\partial F_y^e}{\partial r} \hat{z} \quad (3.18)$$

The curl of the curl of the magnetic vector potential is

$$\begin{aligned} \nabla \times \nabla \times A_x^e \hat{x} = & \left[\frac{-2(\sin(\theta) \cos(\phi))^2}{r} \frac{\partial A_x^e}{\partial r} + \frac{(\cos(\theta) \cos(\phi))^2}{r} \frac{\partial}{\partial r} \left(\frac{r \partial A_x^e}{\partial r} \right) - \frac{\sin^2(\theta)}{r} \frac{\partial}{\partial r} \left(\frac{r \partial A_x^e}{\partial r} \right) \right] \hat{x} \\ & + \left[\frac{-2(\sin(\theta) \cos(\phi))^2}{r} \frac{\partial A_x^e}{\partial r} + \frac{(\cos(\theta) \cos(\phi))^2}{r} \frac{\partial}{\partial r} \left(\frac{r \partial A_x^e}{\partial r} \right) - \frac{\cos(\phi) \sin(\phi)}{r} \frac{\partial}{\partial r} \left(\frac{r \partial A_x^e}{\partial r} \right) \right] \hat{y} \\ & + \left[\frac{-2 \sin(\theta) \cos(\theta) \cos(\phi)}{r} \frac{\partial A_x^e}{\partial r} + \frac{\sin(\theta) \cos(\theta) \cos(\phi)}{r} \frac{\partial}{\partial r} \left(\frac{r \partial A_x^e}{\partial r} \right) \right] \hat{z} \end{aligned} \quad (3.19)$$

and the curl of the curl of the electric vector potential is

$$\begin{aligned} \nabla \times \nabla \times F_y^e \hat{y} = & \left[\frac{2 \sin^2(\theta) \cos(\phi) \sin(\phi)}{r} \frac{\partial F_y^e}{\partial r} - \frac{\cos^2(\theta) \cos(\phi) \sin(\phi)}{r} \frac{\partial}{\partial r} \left(\frac{r \partial F_y^e}{\partial r} \right) \right. \\ & \left. + \frac{\sin(\phi) \cos(\phi)}{r} \frac{\partial}{\partial r} \left(\frac{r \partial F_y^e}{\partial r} \right) \right] \hat{x} + \left[\frac{2(\sin(\theta) \sin(\phi))^2}{r} \frac{\partial F_y^e}{\partial r} \right. \\ & \left. - \frac{(\cos(\theta) \sin(\phi))^2}{r} \frac{\partial}{\partial r} \left(\frac{r \partial F_y^e}{\partial r} \right) - \frac{\cos^2(\phi)}{r} \frac{\partial}{\partial r} \left(\frac{r \partial F_y^e}{\partial r} \right) \right] \hat{y} \\ & + \left[\frac{-2 \sin(\theta) \cos(\theta) \cos(\phi)}{r} \frac{\partial F_y^e}{\partial r} + \frac{\sin(\theta) \cos(\theta) \cos(\phi)}{r} \frac{\partial}{\partial r} \left(\frac{r \partial F_y^e}{\partial r} \right) \right] \hat{z} \end{aligned} \quad (3.20)$$

3.2.4 Field at Point-of-Symmetry

Since the surface current contribution to the far-field calculation from the shadow surface is zero, the shadow surface can be deformed or extended to infinity as shown in Figure 3.1. The field components in this extended volume can be set to zero and this region is referred to as *null-field* region. With this, one can guarantee that for regular convex LoS surface, for every observation point, there exists a point-of-symmetry in the null-field region. This is shown in Figure 3.4.

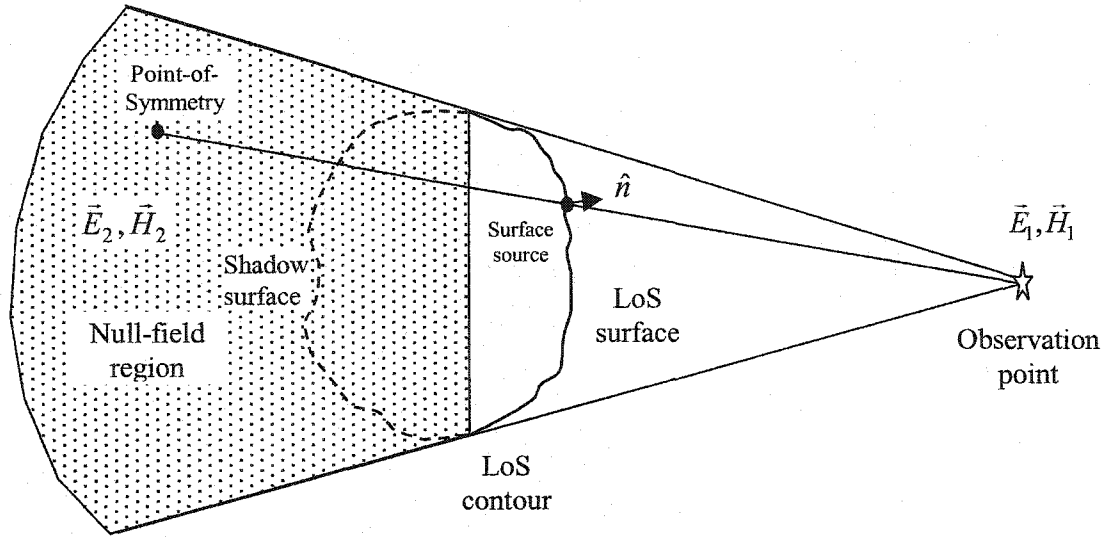


Figure 3.4: The illustration of null-field region, point-of-symmetry and observation point.

The point-of-symmetry is a point that is radially opposite to the observation point with the source point at the centre. At this point-of-symmetry, the field of an elemental surface source has a unique relation to its counterpart at the observation point. To proceed further with the derivation of the fields at the point-of-symmetry, we consider a simple problem in which an elemental current is located at the origin of the coordinate system, and assume that the entire region is in free space. We denote the field at the observation point as

$(\vec{E}_1^e, \vec{H}_1^e)$ and the field at the point-of-symmetry as $(\vec{E}_2^e, \vec{H}_2^e)$. If the location of the observation point in a spherical coordinate system defined as

$$r_1, \phi_1, \theta_1 \quad (3.21)$$

then, the point-of-symmetry is at the location given by

$$r_2 = r_1, \quad \phi_2 = \phi_1 + \pi, \quad \theta_2 = \pi - \theta_1 \quad (3.22)$$

Using (3.13) and (3.14), the field at the observation point (r_1, ϕ_1, θ_1) is

$$\vec{E}_1^e = -\nabla \times \vec{F}_{y1}^e + \frac{1}{j\omega\epsilon_0}(\nabla \times \nabla \times \vec{A}_{x1}^e) \quad (3.23)$$

$$\vec{H}_1^e = \nabla \times \vec{A}_{x1}^e + \frac{1}{j\omega\mu_0}(\nabla \times \nabla \times \vec{F}_{y1}^e) \quad (3.24)$$

Using equations (3.17)-(3.20), the field in the null-field region at point-of-symmetry (r_2, ϕ_2, θ_2) can be written in terms of the vector potential at the observation point A_{x1} and F_{y1} as

$$\vec{E}_2^e = \nabla \times \vec{F}_{y1}^e + \frac{1}{j\omega\epsilon_0}(\nabla \times \nabla \times \vec{A}_{x1}^e) \quad (3.25)$$

$$\vec{H}_2^e = -\nabla \times \vec{A}_{x1}^e + \frac{1}{j\omega\mu_0}(\nabla \times \nabla \times \vec{F}_{y1}^e) \quad (3.26)$$

Equations (3.23)-(3.26) hold for any other component of the surface currents and these equations can be generalised to omit the subscripts x and y .

Now, if we consider the practical situation in which we are interested in the field in

region 1 only, then the field in region 2 \vec{E}_2^e and \vec{H}_2^e can be set to zero. Thus from the equations (3.25) and (3.26) we obtain the relations

$$\nabla \times \vec{A}_1^e = \frac{1}{j\omega\mu_0} (\nabla \times \nabla \times \vec{F}_1^e) \quad (3.27)$$

$$\nabla \times \vec{F}_1^e = -\frac{1}{j\omega\epsilon_0} (\nabla \times \nabla \times \vec{A}_1^e) \quad (3.28)$$

Substituting (3.27) and (3.28) into (3.23) and (3.24), we obtain

$$\vec{E}_1^e = -2\nabla \times \vec{F}_1^e \quad (3.29)$$

$$\vec{H}_1^e = \frac{2}{j\omega\mu_0} \nabla \times \nabla \times \vec{F}_1^e \quad (3.30)$$

From equations (3.29) and (3.30) it is evident that only one of the surface currents, which appear in the equations for the vector potentials, is needed to obtain the field outside the closed surface. Thus, the general form of (3.29) and (3.30) is

$$\vec{E}_1 = -\frac{2\epsilon}{4\pi} \iint_{LoS} \nabla \times \vec{M}^{se} ds \quad (3.31)$$

$$\vec{H}_1 = \frac{2\epsilon}{4\pi j\omega\mu_0} \iint_{LoS} \nabla \times \nabla \times \vec{M}^{se} ds \quad (3.32)$$

One easily observes that if the surface is regular and convex, then the point-of-symmetry always falls in the null-field region. For most simulation problems, the enclosing

box is of regular shape such as a rectangular box. In the above derivation, the effects of edge currents are neglected. However, they are addressed in the next section.

3.2.5 The LoS Edge Currents

In accordance with the equivalence principle, the time harmonic E -field in the far zone can be expressed in terms of the electric and magnetic fields \vec{E}^s and \vec{H}^s on the surface enclosing the radiating sources [3]:

$$\vec{E} = -\frac{j\omega\mu}{4\pi} \iint_S (\hat{n} \times \vec{H}^s) \frac{e^{-j\beta R_{QP}}}{R_{QP}} ds - \frac{j\omega\eta\epsilon}{4\pi} \iint_S [\hat{R} \times (\hat{n} \times \vec{E}^s)] \frac{e^{-j\beta R_{QP}}}{R_{QP}} ds \quad (3.33)$$

Here, as shown in Figure 3.5, R_{QP} is the distance from the surface field point Q to the observation point P , \hat{n} is the unit normal to the surface, \hat{R} is the unit vector from the surface source to the observation point, β is the free-space wave number, ω is the frequency, and η is the free space intrinsic impedance.

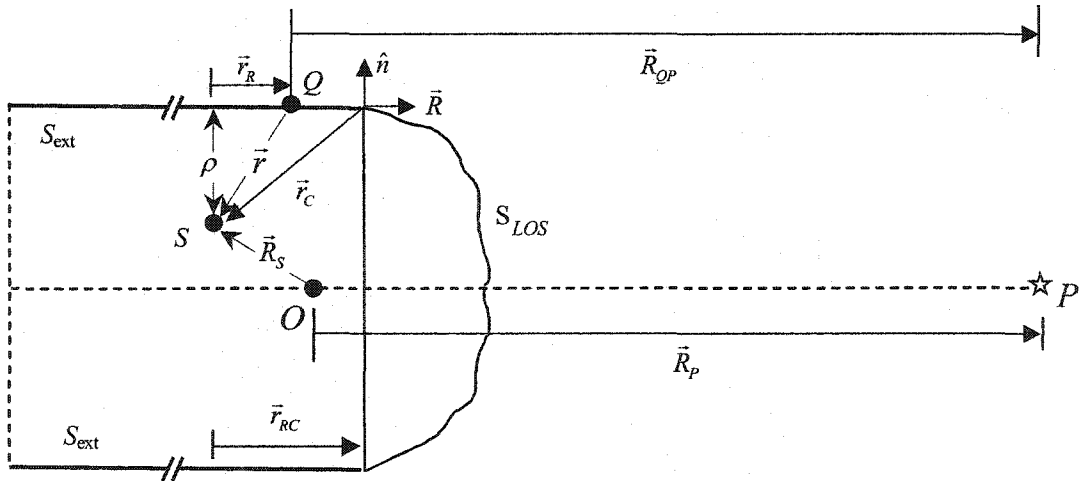


Figure 3.5: LoS approximations and notations

The LoS approximation is obtained by transforming the ‘shadow’ surface into an infinite (extended) surface supported by the LoS contour, as shown in Figure 3.1. When the observation point is in the far zone, the extended surface becomes a semi-infinite tubular frustum whose profile is defined by the LoS contour (see Figure 3.5). In general, the far field is calculated from the equivalent electric and magnetic surface current densities on the LoS surface S_{LOS} and on the extended surface S_{ext} . Our objective is to obtain accurate far-field information by integrating the surface current densities over S_{LOS} only, and to reduce the contribution of the S_{ext} current densities to an integral over the LoS contour C_{LOS} .

We use a local rectangular coordinate system with unit vectors \hat{R} , \hat{n} and $\hat{\tau}$ as shown in Figure 3.5, where $\hat{\tau} = \hat{n} \times \hat{R}$. Using the relation $\hat{n} \cdot \hat{R} = 0$ and neglecting the far-zone E_R component, the second term of (3.33) can be written as

$$\vec{E}_{MS_{ext}} = -\frac{j\omega\eta\epsilon}{4\pi} \iint_{S_{ext}} \hat{R} \times (\hat{n} \times \vec{E}^s) \frac{e^{-j\beta R_{QP}}}{R_{QP}} ds = -\frac{j\omega\eta\epsilon}{4\pi} \iint_{S_{ext}} \hat{n} E_R^s \frac{e^{-j\beta R_{QP}}}{R_{QP}} ds \quad (3.34)$$

where E_R^s is the R -component of the electric field on the extended surface. The surface integral of (3.34) can be expanded as

$$\vec{E}_{MS_{ext}} = -\frac{j\omega\eta\epsilon}{4\pi} \oint_{C_{LOS}} \hat{n} \left[\int_{R_{CP}}^{\infty} E_R^s \frac{e^{-j\beta R_{QP}}}{R_{QP}} dR_{QP} \right] dl_C \quad (3.35)$$

where the lower limit R_{CP} is the distance from the respective point on the LoS contour C_{LOS} to the observation point P (see Figure 3.5). Introducing a variable

$$r_R = \hat{R} \cdot (\vec{R}_P - \vec{R}_{QP} - \vec{R}_S) = R_P - R_{QP} - (\hat{R} \cdot \vec{R}_S) \quad (3.36)$$

(3.35) can be written as

$$\vec{E}_{MS_{ext}} = -\frac{j\omega\eta\epsilon}{4\pi} \oint_{C_{LOS}} \hat{n} \mathcal{J}_E dl_C \quad (3.37)$$

where

$$\mathcal{J}_E = \int_{r_{RC}}^{-\infty} E_R^S \frac{e^{-j\beta R_{QP}}}{R_{QP}} dr_R \quad (3.38)$$

and $r_R = r_{RC}$ when the surface source point Q lies on C_{LOS} (see Figure 3.5).

Similarly, with the far-field assumption that the radial field components are negligible, the first term of (3.33) becomes

$$\vec{E}_{JS_{ext}} = -\frac{j\omega\mu}{4\pi} \iint_{S_{ext}} (\hat{n} \times \vec{H}^S) \frac{e^{-j\beta R_{QP}}}{R_{QP}} ds = \frac{j\omega\mu}{4\pi} \iint_{S_{ext}} (\hat{R} \times \hat{n}) H_R^S \frac{e^{-j\beta R_{QP}}}{R_{QP}} ds \quad (3.39)$$

where H_R^S is the surface magnetic field component along \hat{R} . The electric field in (3.39) is now written in terms of a contour and a line integral as

$$\vec{E}_{JS_{ext}} = \frac{j\omega\mu}{4\pi} \oint_{C_{LOS}} (\hat{R} \times \hat{n}) \mathcal{J}_H dl_C \quad (3.40)$$

where

$$\mathcal{J}_H = \int_{r_{RC}}^{-\infty} H_R^S \frac{e^{-j\beta R_{QP}}}{R_{QP}} dr_R \quad (3.41)$$

The surface field components H_R^S and E_R^S in (3.38) and (3.41) are due to the enclosed electric and magnetic sources inside the equivalent surface. In order to simplify the derivations, we consider only an infinitesimal electric dipole whose surface field R -components are denoted as H_R^{Se} and E_R^{Se} . The derivation is similar for a magnetic dipole. In a linear medium, the surface magnetic field R -component of a complex radiator can be

represented as a superposition of the elemental contributions, $H_R^S = \sum_e H_R^{Se}$. Then, (3.40) can be written as

$$\vec{E}_{JS_{ext}} = \frac{j\omega\mu}{4\pi} \sum_e \oint_C (\hat{R} \times \hat{n}) \left[\int_{r_{RC}}^{\infty} H_R^{Se} \frac{e^{-j\beta R_{QP}}}{R_{QP}} dr_R \right] dl_C \quad (3.42)$$

a similar expression can be written for $\vec{E}_{MS_{ext}}$ of (3.37).

Consider the electric current element $Id\vec{l} = I_R \hat{R} + I_n \hat{n} + I_\tau \hat{\tau}$ at a point S inside the enclosed surface whose position vector with respect to the surface point Q is $\vec{r} = r_R \hat{R} + r_n \hat{n} + r_\tau \hat{\tau}$. Its surface field components, H_R^{Se} and E_R^{Se} , are obtained as [3]

$$H_R^{Se} = \frac{(1 + j\beta r) e^{-j\beta r}}{4\pi r^3} (r_n I_\tau - r_\tau I_n) \quad (3.43)$$

$$E_R^{Se} = \frac{j\eta e^{-j\beta r}}{4\pi\beta r^3} \left\{ \left[(3 + 3j\beta r - \beta^2 r^2) \frac{\rho^2}{r^2} - 2(1 + j\beta r) \right] I_R \right. \\ \left. + \left[(-3 - 3j\beta r + \beta^2 r^2) \frac{r_R}{r^2} \right] (r_n I_n + r_\tau I_\tau) \right\} \quad (3.44)$$

where $r = |\vec{r}|$. The orthogonal distance from the source to the surface of the tube is

$$\rho = \sqrt{r^2 - r_R^2} \quad (3.45)$$

where r_R is defined in (3.36) see also Figure 3.2. The integral over H_R^{Se} in the far zone (3.41) becomes

$$\mathcal{J}_H^e = (r_n I_\tau - r_\tau I_n) \frac{e^{-j\beta(R_P + \vec{R}_S \cdot \hat{R})}}{R_P} \int_{r_{RC}}^{\infty} \frac{(1 + j\beta r)}{4\pi r^3} e^{-j\beta(r - r_R)} dr_R \quad (3.46)$$

where R_P and \bar{R}_S are shown in Figure 3.2. Our goal is to find an approximation of (3.46) such that \mathcal{J}_H^e is expressed in terms of the field at the LoS contour point that corresponds to $r_R = r_{RC}$. We change variable as

$$u = (r - r_R) - u_l = \left(\sqrt{r_R^2 + \rho^2} - r_R \right) - u_l \quad (3.47)$$

where $u_l = r_C - r_{RC}$. Here, $r = r_C$ and $r_R = r_{RC}$ when the surface point Q lies on C_{LOS} (see Figure 3.2). Using the relationships

$$r = \frac{(u + u_l)^2 + \rho^2}{2(u + u_l)}, \quad r_R = \frac{(u + u_l)^2 - \rho^2}{2(u + u_l)}, \quad \frac{dr_R}{du} = \frac{-r}{(u + u_l)} \quad (3.48)$$

\mathcal{J}_H^e is written in terms of u as

$$\mathcal{J}_H^e = -(r_n I_\tau - r_\tau I_n) \frac{e^{-j\beta(R_P + \bar{R}_S \cdot \hat{R} + u_l)}}{4\pi R_P} \int_0^\infty \left[\frac{2j\beta}{((u + u_l)^2 + \rho^2)} + \frac{4(u + u_l)}{((u + u_l)^2 + \rho^2)^2} \right] e^{-j\beta u} du \quad (3.49)$$

We integrate by parts the first integral term of (3.49) as

$$\int_0^\infty \left[\frac{2j\beta}{((u + u_l)^2 + \rho^2)} \right] e^{-j\beta u} du = \frac{-2}{((u + u_l)^2 + \rho^2)} e^{-j\beta u} \Big|_0^\infty - \int_0^\infty \left[\frac{4(u + u_l)}{((u + u_l)^2 + \rho^2)^2} \right] e^{-j\beta u} du \quad (3.50)$$

which results in

$$\mathcal{J}_H^e = -(r_n I_\tau - r_\tau I_n) \frac{e^{-j\beta(R_P + \bar{R}_S \cdot \hat{R} + u_l)}}{4\pi R_P} \left[\frac{-2}{(u_l^2 + \rho^2)} \right] \quad (3.51)$$

The function \mathcal{J}_H^e has to be expressed in terms of the field component H_R^{Se} on the contour.

To achieve that, we multiply (3.51) by the factor

$$1 + \frac{2u_l}{j\beta(u_l^2 + \rho^2)} \quad (3.52)$$

The second term of (3.52) is in fact equal to $1/j\beta r_C$ and it has a negligible effect on \mathcal{J}_H^e for $r_C \gg \lambda$, λ being the wavelength. With this approximation, (3.51) becomes

$$\mathcal{J}_{Ha}^e = \frac{e^{-j\beta(R_P + \vec{R}_S \cdot \hat{R})}}{R_P} \left[\frac{(u_l^2 + \rho^2)}{j2\beta u_l^2} \right] e^{-j\beta u_l} H_R^{Se}(u = u_l) \quad (3.53)$$

The position of the original sources inside the virtual surface determines u_l . However, in a practical computational problem, the locations of the original sources inside the enclosed surface are not known. On the other hand, a computational algorithm provides full information about the field at the contour. If H_R^{Se} is available, then the term

$$C_H^e = \frac{(u_l^2 + \rho^2)}{j2\beta u_l^2} \quad (3.54)$$

can be extracted from its phase for a point on C_{LOS} . From (3.43), the phase of H_R^{Se} is the argument of the term $(j\beta r + 1)e^{-j\beta r}$:

$$\Theta_H^e = -\beta r + \arctan(\beta r). \quad (3.55)$$

Its derivative with respect to r_R is

$$\frac{d\Theta_H^e}{dr_R} = -\beta \left[1 - \frac{1}{1 + (\beta r)^2} \right] \left(\frac{r_R}{r} \right). \quad (3.56)$$

For large βr , C_H^e can be obtained from the approximated phase derivative as

$$\left[-j \left(\frac{d\Theta_H^e(u = u_l)}{dr_R} + \beta \right) \right]^{-1} \approx \left[-\frac{j\beta(r - r_R)}{r} \right]^{-1} = \frac{u_l^2 + \rho^2}{j2\beta u_l^2} = C_H^e \quad (3.57)$$

In the case of a complex source distribution, a constant C_H can be obtained from the phase Θ_H of the total field H_R^S as is done for the elemental field H_R^{Se} :

$$C_H = \left[-j \left(\frac{d\Theta_H(u = u_l)}{dr_R} + \beta \right) \right]^{-1} \quad (3.58)$$

Thus, the approximation to \mathcal{J}_H from (3.41) can be written as

$$\mathcal{J}_{Ha} = C_H H_R^S \frac{e^{-j\beta R_{CP}}}{R_{CP}} \Big|_{r=r_C} \quad (3.59)$$

The derivation thus far addressed the contribution of the electric surface currents ($\hat{n} \times \vec{H}^S$) at S_{ext} to the far-zone electric field $\vec{E}_{JS_{ext}}$ in (3.40). A similar derivation is carried out for the contribution of the magnetic surface currents to the far-zone electric field $\vec{E}_{MS_{ext}}$ in (3.37). An elemental contribution to (3.38) is obtained as

$$\mathcal{J}_E^e = \mathcal{J}_{ER}^e + \mathcal{J}_{En}^e + \mathcal{J}_{Er}^e \quad (3.60)$$

where

$$\mathcal{J}_{ER}^e = \frac{e^{-j\beta(R_p + \vec{R}_S \cdot \hat{R})}}{R_p} \int_{r_{RC}}^{-\infty} \left[\chi(r) \left(\frac{\rho}{r} \right)^2 - 2 \frac{(1 + j\beta r)}{r^3} \right] I_R e^{-j\beta(r-r_R)} dr_R;$$

$$\mathcal{J}_{En}^e = -\frac{e^{-j\beta(R_p + \vec{R}_S \cdot \hat{R})}}{R_p} \int_{r_{RC}}^{-\infty} \chi(r) \frac{r_R}{r^2} r_n I_n e^{-j\beta(r-r_R)} dr_R;$$

$$\mathcal{J}_{E\tau}^e = -\frac{e^{-j\beta(R_p + \vec{R}_S \cdot \hat{R})}}{R_p} \int_{r_{RC}}^{-\infty} \chi(r) \frac{r_R}{r^2} r_\tau I_\tau e^{-j\beta(r-r_R)} dr_R;$$

$$\chi(r) = \frac{3 + 3j\beta r - \beta^2 r^2}{r^3}.$$

In (3.60), the most significant component for far-field computations is \mathcal{J}_{ER}^e , which is due to the elemental source I_R . For elemental currents polarized along \hat{n} or $\hat{\tau}$, the far-field contribution through \mathcal{J}_H^e is far more significant than that from \mathcal{J}_{En}^e and/or $\mathcal{J}_{E\tau}^e$ (with a factor of approximately η). Under the condition $\beta^2 r^2 \gg 3$, \mathcal{J}_{ER}^e can be expressed in terms of u as

$$\begin{aligned} \mathcal{J}_{ER}^e \approx \mathcal{J}_{ERa}^e = & \frac{e^{-j\beta(R_p + \vec{R}_S \cdot \hat{R})}}{R_0} \left\{ 4j\beta\rho^2 \int_0^{+\infty} \left[\frac{j\beta(u+u_l)}{[(u+u_l)^2 + \rho^2]^2} + \frac{6(u+u_l)^2}{[(u+u_l)^2 + \rho^2]^3} \right] e^{-j\beta u} du \right. \\ & \left. + \int_0^{+\infty} \left[\frac{2j\beta}{(u+u_l)^2 + \rho^2} + \frac{4(u+u_l)}{[(u+u_l)^2 + \rho^2]^2} \right] e^{-j\beta u} du \right\}. \end{aligned} \quad (3.61)$$

Using integration by parts and the result of the integral

$$\int_0^{+\infty} \left[\frac{3(u+u_l)^2 + \rho^2}{((u+u_l)^2 + \rho^2)^3} \right] e^{-j\beta u} du = \left[\frac{\pi(3+3\rho\beta - (\rho\beta)^2)}{4\rho^3} e^{-\rho\beta} \right] e^{-j\beta u_l}, \quad (3.62)$$

(3.61) is reduced to

$$\mathcal{J}_{ERa}^e = \frac{e^{-j\beta(R_p + \bar{R}_S \cdot \hat{R})}}{R_p} \left\{ 4j\beta\rho^2 \left[\frac{-u_l}{(u_l^2 + \rho^2)^2} + \frac{\pi(3+3\rho\beta - (\rho\beta)^2)e^{-\rho\beta}}{4\rho^3} \right] e^{-j\beta u_l} - \frac{4e^{-j\beta u_l}}{(u_l^2 + \rho^2)} \right\} \quad (3.63)$$

When $\rho\beta \gg 1$, the term

$$\frac{\pi(3+3\rho\beta - (\rho\beta)^2)e^{-\rho\beta}}{4\rho^3} \quad (3.64)$$

is negligible, and (3.63) reduces to

$$\mathcal{J}_{ERa}^e = \frac{4e^{-j\beta(R_p + \bar{R}_S \cdot \hat{R} + u_l)}}{R_p} \left\{ j\beta \left[\frac{-u_l\rho^2}{(u_l^2 + \rho^2)^2} \right] - \frac{1}{(u_l^2 + \rho^2)} \right\}. \quad (3.65)$$

Equation (3.65) can be re-written in terms of E_R^{Se} using the same approach as in the case of

\mathcal{J}_H^e :

$$\mathcal{J}_{ERa}^e = \frac{e^{-j\beta(R_p + \bar{R}_S \cdot \hat{R})}}{R_p} \left[\frac{(u_l^2 + \rho^2)}{j2\beta u_l^2} \right] e^{j\beta u_l} E_R^{Se}(I_R, u = u_l). \quad (3.66)$$

Here, $E_R^{Se}(I_R, u = u_l)$ is the electric field R -component on the surface due to the elemental

current I_R . The coefficient C_E , analogous to C_H , is derived from the derivative of the phase of the total electric field:

$$C_E = \left[-j \left(\frac{d\Theta_E(u=u_l)}{dr_R} + \beta \right) \right]^{-1}. \quad (3.67)$$

In the above derivation, we addressed the contribution of the dominant term due to the \hat{R} -oriented sources. A similar approximation can be applied for I_n and I_τ components of the current element. In a practical problem, however, their contribution is negligible. The approximate solution to \mathcal{J}_E of (3.38) is thus

$$\mathcal{J}_{Ea} = C_E E_R^S \frac{e^{-j\beta R_{CP}}}{R_{CP}} \Big|_{r=r_C}. \quad (3.68)$$

3.2.5.1 The Edge Currents Contribution to the Far-field

In the LoS approach, three critical approximations are made: (i) the approximation transforming (3.51) into (3.53); (ii) the simplification of the derivative of the phase term of the field at the contour, see (3.57); and (iii) neglecting the term (3.64) in the expression for \mathcal{J}_{Ea}^e . The first two require that $\beta r_C \gg 1$; the third one assumes that $\beta \rho \gg 1$. These conditions limit the minimum size of the virtual surface. The accuracy of these approximations is investigated below. We show the error due to the approximations in the evaluation of the line integrals \mathcal{J}_H^e and \mathcal{J}_E^e . \mathcal{J}_H^e shows the contribution of the surface field component H_R^e to the far-zone field of an elemental source; while \mathcal{J}_E^e is associated with the contribution of the E_R^e field component. Electric current densities, which are transversal to the LoS contribute to the radiated field predominantly through H_R^e ; while if the current

density is longitudinal to the LoS it contributes to the far field mostly through E_R^e . We, therefore, investigate the approximation error of the \mathcal{J}_H^e integral in the case of transversely oriented dipole element, and that of the \mathcal{J}_E^e integral in the case of longitudinally oriented dipole element.

A. Error due to the approximation of the line integral \mathcal{J}_H^e

The error due to the approximation of the line integral \mathcal{J}_H^e in (3.49) with \mathcal{J}_{Ha}^e in (3.53) is calculated numerically using MATLAB®. The exact solution to (3.49) is obtained with Fast Fourier Transform (FFT) whose discrete form is

$$\tilde{\mathcal{J}}_H^e(k\beta) = (r_\tau I_n - r_n I_\tau) \frac{e^{-j\beta(R_p + \vec{R}_S \cdot \hat{R} + u_l)}}{4\pi R_0} F(k\Delta\beta) \quad (3.69)$$

where

$$F(k\Delta\beta) = \Delta u \sum_{n=0}^N f(n\Delta u) e^{-j(k\Delta\beta)(n\Delta u)} . \quad (3.70)$$

Here, k denotes a discrete point in the β -domain. The discretization step in the u -domain is $\Delta u = 10^{-4}$ m, and the number of points is $N = 2^{18}$. The discrete step in the β -domain is calculated as $\Delta\beta = 2\pi/(N\Delta u)$. The function $f(n\Delta u)$ is the discretized square-bracket term in the integral in (3.49).

The error function ξ due to the approximation of \mathcal{J}_H^e is defined as:

$$\xi = \frac{|\mathcal{J}_{Ha}(\beta) - \mathcal{J}_H(\beta)|}{|\mathcal{J}_H(\beta)|} \times 100\% . \quad (3.71)$$

The coefficient C_H^e used in the approximation \mathcal{J}_{Ha}^e contains two constants, ρ and u_l , where u_l is dependent on the distance between the source and the LoS contour r_{RC} . Therefore, the error function ξ is examined in the following cases: (i) constant ρ and varying r_{RC} , and (ii) constant r_{RC} and varying ρ (for the meaning of r_{RC} and ρ refer to Figure 3.5). The current element must be either \hat{n} -polarized or $\hat{\tau}$ -polarized (see Figure 3.5) in order to obtain a nonzero H_R^{Se} component at the LOS contour, see (3.43). The results for both polarizations are identical.

The approximation errors are shown in Figure 3.6 and Figure 3.7. It is evident that the distance between the source and the LoS contour r_{RC} does not influence strongly the error due to the approximation of the \mathcal{J}_H^e integral when $r_{RC} \geq \lambda$ and $\rho \geq \lambda$. In fact, under these conditions, the approximation error ξ is well below 0.5% (see the curves for $r_{RC} = \pm\lambda_0$ and $r_{RC} = \pm 2\lambda_0$ in Figure 3.6 and the curves for $\rho = 1.0\lambda_0, 2.0\lambda_0$ in Figure 3.7). In both figures, the results for $\beta < \beta_0 \approx 21$ rad/m show that when the virtual surface size in any direction becomes smaller than the wavelength, the approximation accuracy quickly deteriorates. This effect is even more pronounced in the approximation of the \mathcal{J}_E^e integral.

B. Error due to the approximation of the line integral \mathcal{J}_E^e

We consider the contribution to \mathcal{J}_E^e from an \hat{R} -polarized elemental current source I_R denoted as \mathcal{J}_{ER}^e , see (3.60). Such a source generates a significant E_R^{Se} field component at the LOS contour. This is the worst case scenario for the approximation due to the substitution of \mathcal{J}_E with \mathcal{J}_{Ea} of (3.68). As in the case of \mathcal{J}_{Ha} , the error due to the approximation of \mathcal{J}_{ER}^e with \mathcal{J}_{ERa}^e is examined for: (i) constant ρ and varying r_{RC} , and (ii) constant r_{RC} and varying ρ . These errors are plotted in Figures 3.8 and 3.9. It becomes obvious from Figure 3.8 that not only the distance to the extended surface ρ must be kept larger than a wavelength but

also r_{RC} should not be much larger than ρ . The latter restriction, however, is not of practical concern. It is also important to note that if the condition $\rho > \lambda$ is violated, the error due to the approximation increases drastically (see Figure 3.9). This is due to the term (3.64) which is being neglected in the more general expression for \mathcal{J}_{ERa}^e given by (3.63).

In summary, the following guidelines can be suggested for the choice of the LoS surface size:

1. The minimum distance from S_{LOS} to the enclosed sources should be more than a wavelength, i.e. $\rho_{\min} \geq \lambda$.
2. The orthogonal distance between the enclosed sources and the LoS contour should be less than twice the minimum distance between the sources and the virtual surface. At the same time, it should be larger than the wavelength, i.e. $\lambda \leq r_{RC} < 2\rho_{\min}$.

If these two conditions are observed, an approximation error of about 2% or less is achieved.

In the next section, we examine a practical problem with $\rho_{\min} = 1.25\lambda$.

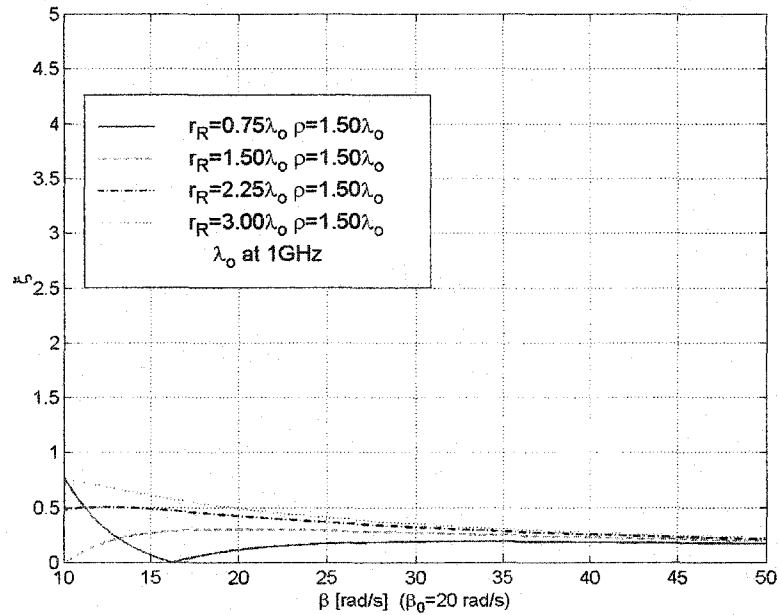


Figure 3.6. Error function of the H_R component for $I_{n/\tau}$ with constant ρ for positive r_R .

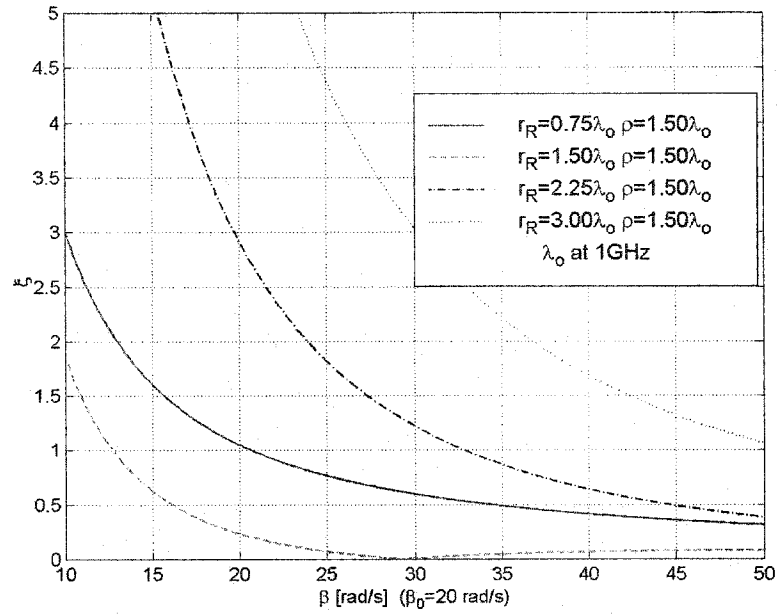


Figure 3.7: Error function of the E_R component for $I_{n/\tau}$ with constant ρ for positive r_R .

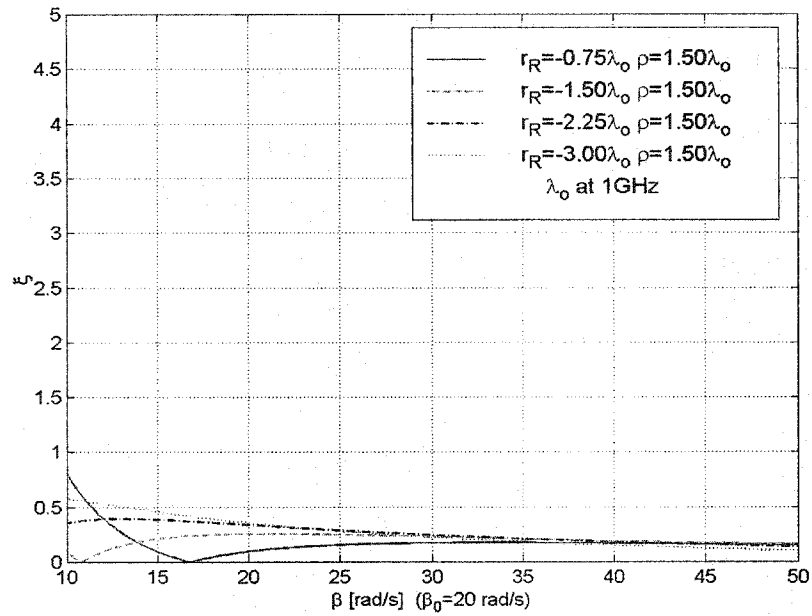


Figure 3.8: Error function of the E_R component for I_R with constant ρ for positive r_R .

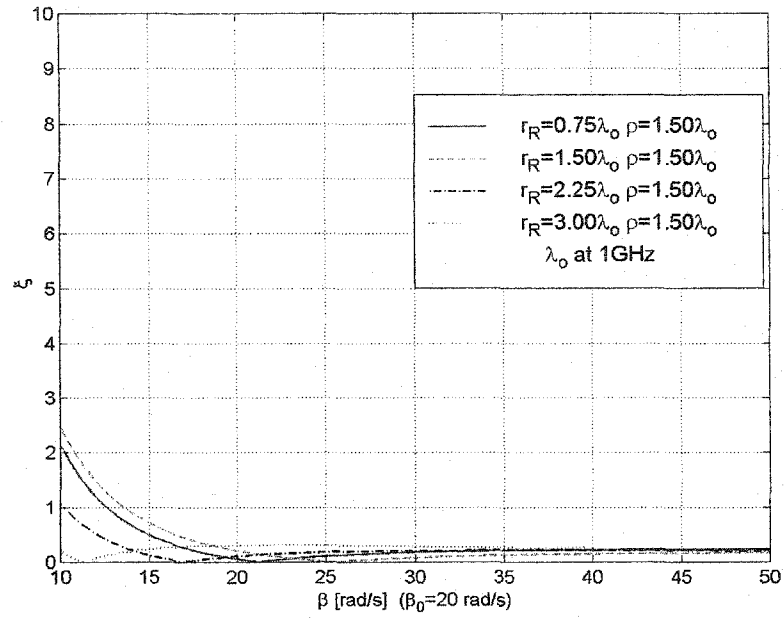


Figure 3.9: Error function of the H_R component for $I_{n/\tau}$ with constant ρ for negative r_R .

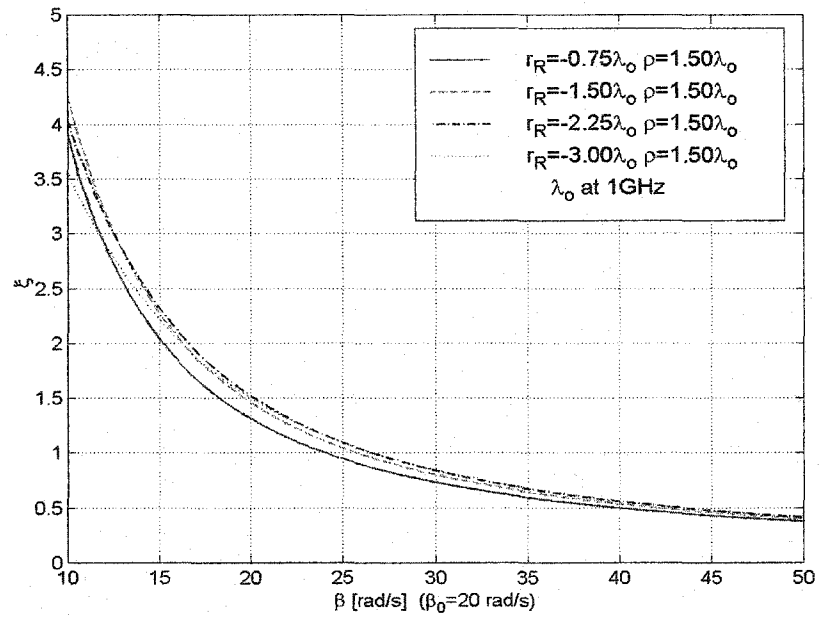
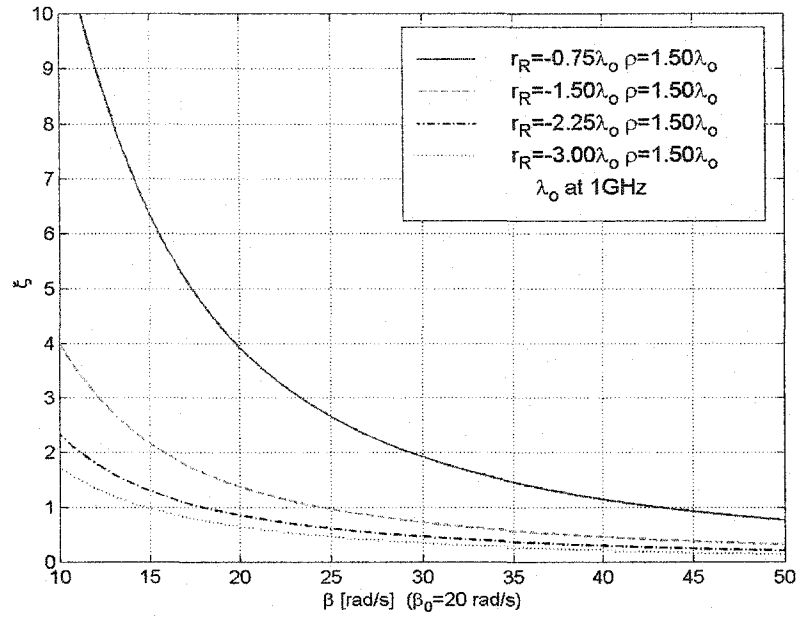
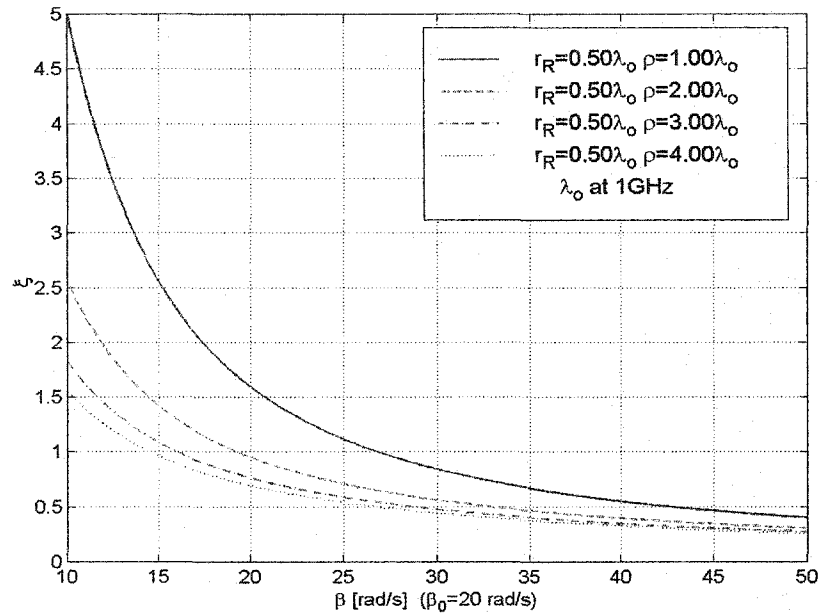


Figure 3.10: Error function of the E_R component for I_R with constant ρ for negative r_R .


 Figure 3.11: Error function of the E_R component for $I_{n/\tau}$ with constant ρ for negative r_R .

 Figure 3.12: Error function of the H_R component for $I_{n/\tau}$ with constant r_R for different ρ .

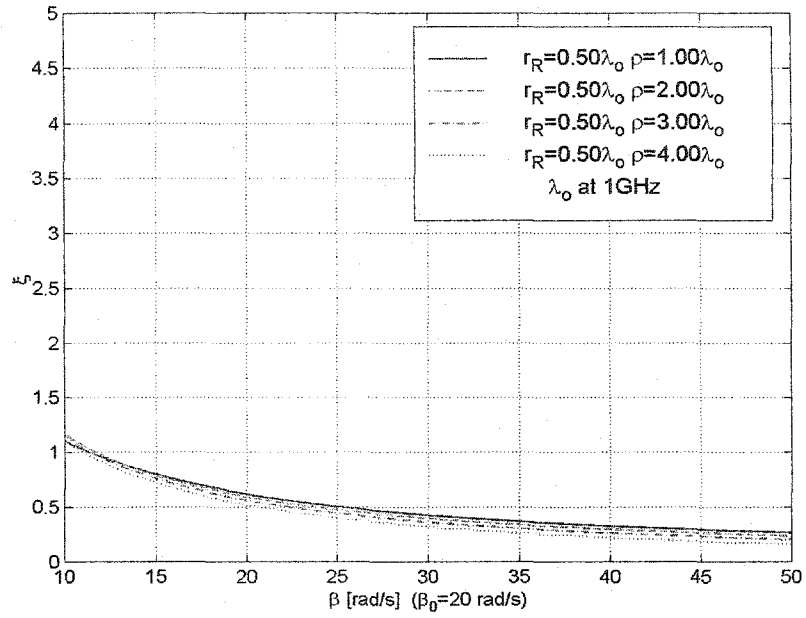


Figure 3.13: Error function of the E_R component for I_R with constant r_R for different ρ .

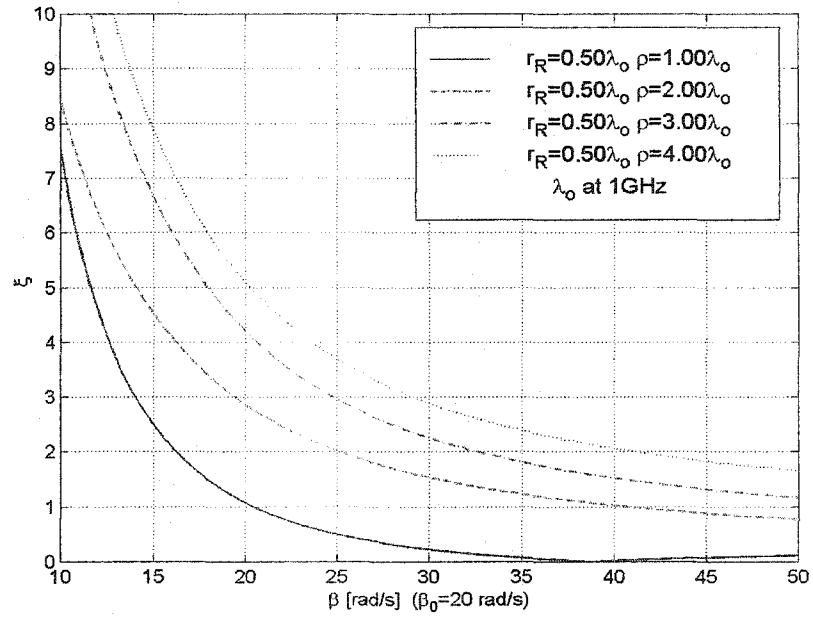


Figure 3.14: Error function of the E_R component for $I_{n/\tau}$ with constant r_R for different ρ .

3.3 Application of the LoS Approach to a Practical Problem

A general approximate expression for the far field is obtained using (3.33), (3.37) and (3.40) :

$$\begin{aligned} \vec{E} \approx & -\frac{j\omega\mu}{4\pi} \left[\iint_{S_{LoS}} (\hat{n} \times \vec{H}^S) \frac{e^{-j\beta R_{QP}}}{R_{QP}} ds + \oint_c (\hat{R} \times \hat{n}) H_R^S \frac{e^{-j\beta R_{QP}}}{R_{QP}} C_H dl \right] \\ & + \frac{j\omega\eta\varepsilon}{4\pi} \left[\iint_{S_{LoS}} (\hat{R} \times (\hat{n} \times \vec{E}^S)) \frac{e^{-j\beta R_{QP}}}{R_{QP}} ds + \oint_c \hat{n} E_R^S \frac{e^{-j\beta R_{QP}}}{R_{QP}} C_E dl \right] \end{aligned} \quad (3.72)$$

We note that the LoS approach can be further simplified under the condition that the LoS surface is smooth and that the observation point falls in the positive side of the unit normal for every surface point. Typically, computational algorithms use rectangular boxes as virtual surfaces. These satisfy the stipulated LoS conditions. In this case, in (3.72), one can resolve either the surface integral over the equivalent electric currents ($2\hat{n} \times \vec{H}^S$), or the surface integral over the equivalent magnetic currents ($2\hat{n} \times \vec{E}^S$). This improves additionally the efficiency of the far-field calculations. Notice that in either case both contour integrals in (3.72) have to be computed.

To illustrate the reduction of the surface integration by the LoS approach, consider the example in Figure 3.15. The source contribution to the field at the observation point P_1 is from the top xz -plane only. The source contribution at P_2 is from the top xz -plane and the right yz -plane. In this method, up to three surfaces and up to six edges could contribute to the calculation of the radiation pattern.

The contribution from the edge current to the far field radiation results in the calculation of the coefficients C_E and C_H according to (3.58) and (3.67). It is observed in (3.58) and (3.67), that the derivative with respect to R can be projected to any desired direction (x , y or z) without changing the overall effect. That is, the derivative with respect to R can be written as

$$\frac{d\Theta(E_R)}{dR} = \frac{d\Theta(E_x)}{dx} = \frac{d\Theta(E_y)}{dy} = \frac{d\Theta(E_z)}{dz} \quad (3.73)$$

In many numerical techniques such as in the FDTD technique, the information of the field components on the edges that are parallel to the other edges of the rectangular box are available. From this the coefficients C_E and C_H can be easily calculated.

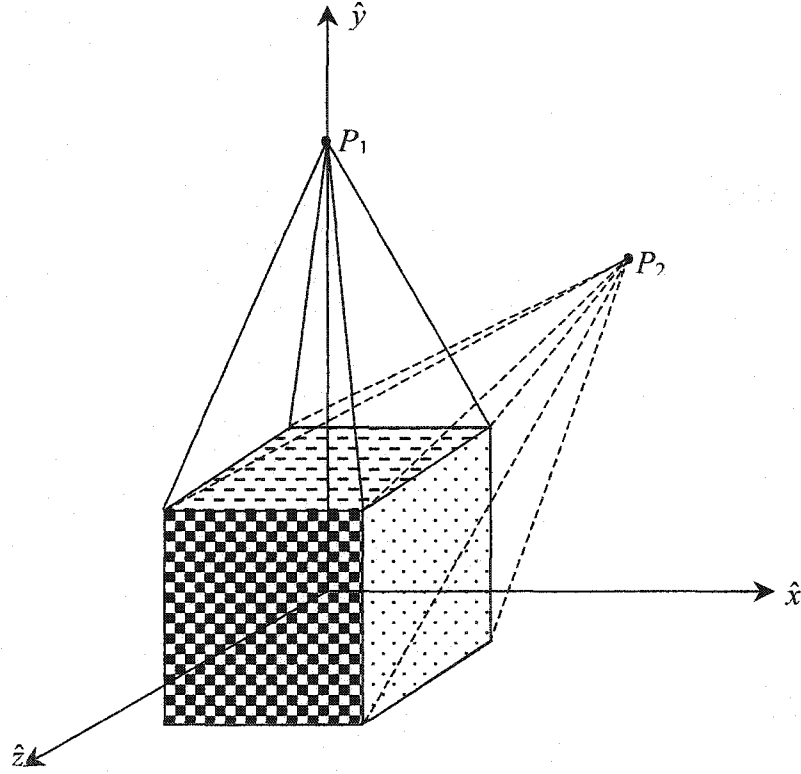


Figure 3.15: Enclosing surface in the simulation of radiation pattern.

In some practical applications, surface currents on only one face of the box are required, and, in this case, edge current effects are negligible. The two practical examples in section 3.3 show the effect of the edge currents.

3.3.1 A Numerical Example of the Application of LoS Approximation

The accuracy of the LoS approach as compared to the standard equivalence principle is demonstrated using the simulation of a half-wavelength dipole. In the simulation, the dipole is enclosed in a rectangular box of size $2.5\lambda \times 2.5\lambda \times 3.5\lambda$. The box is discretized into $60 \times 60 \times 120$ cells, which gives a maximum cell size of $\lambda/24$. Such a cell size is within the standard range in numerical simulations.

The tangential surface field components are calculated over the LoS surface using (3.43) and (3.44), and the far-field surface integral over S_{LOS} is computed according to (3.72). The far field E -plane radiation pattern for the E_θ component is computed and the results are shown in Figures 3.17, 3.18 and 3.19. Each figure contains three plots and they are for (i) the radiation pattern using the standard equivalence principle, (ii) the radiation pattern using the LoS approach, and (iii) the radiation pattern using the LoS approach excluding the contour integrals.

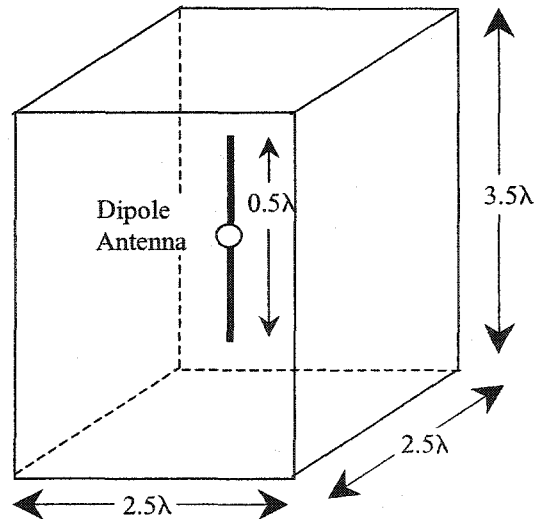


Figure 3.16: Dipole antenna for the LoS numerical example

When principal plane patterns are calculated, the LoS approach uses at most two of the six surface faces; whereas for the standard equivalence principle, the currents on all six faces are integrated. The physical size of the virtual box for the simulation is such that the shortest distance from the dipole edge to the surface of the box is 1.25λ . For this example, $\rho_{\min} \approx 1.27\lambda$, and the corresponding expected maximum approximation error is below 2%.

Figure 3.17 shows the normalized radiation pattern plots. The plots in Figure 3.17 somewhat mask the approximation error. However, when the plots are normalized to a common value such as the maximum value of the standard equivalence radiated field, the errors are more visible. These are observed better in Figure 3.18, which contains the patterns normalized to the maximum of the radiated field according to the standard equivalence. We notice that the exclusion of the contour integrals leads to significant error, which can be as high as 20%. The maximum error of the LoS approach, which takes into account the contribution of the edge currents, is lower than 2%, as expected. This error is within an acceptable range for most practical applications.

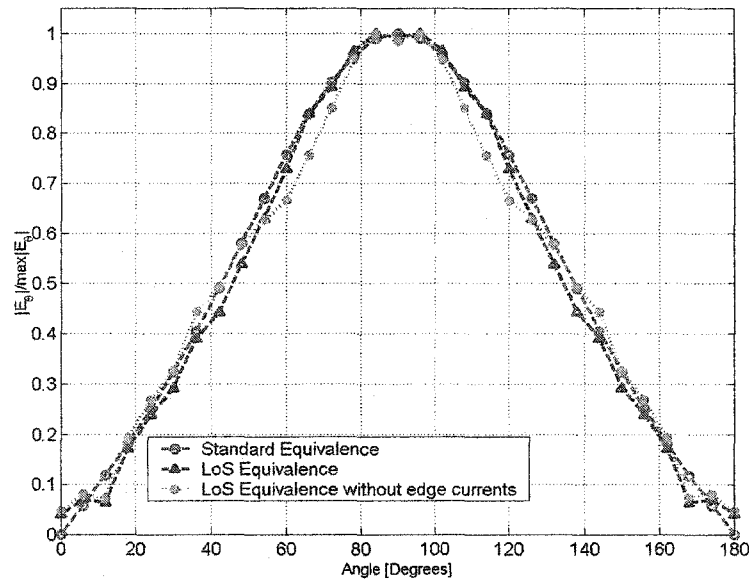


Figure 3.17: Self normalized E_0 radiation pattern of a dipole antenna in linear scale

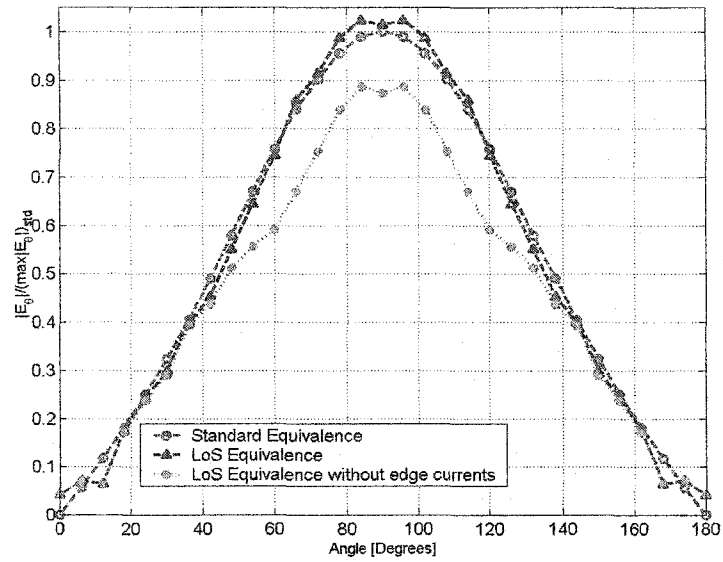


Figure 3.18: Normalized to SE , E_0 radiation pattern of a dipole antenna in linear scale

In the plots of Figure 19, the results are in logarithmic scale. The error below the relative gain of -15 dB is attributed to the numerical errors and not to the approximation used in the LoS approach.

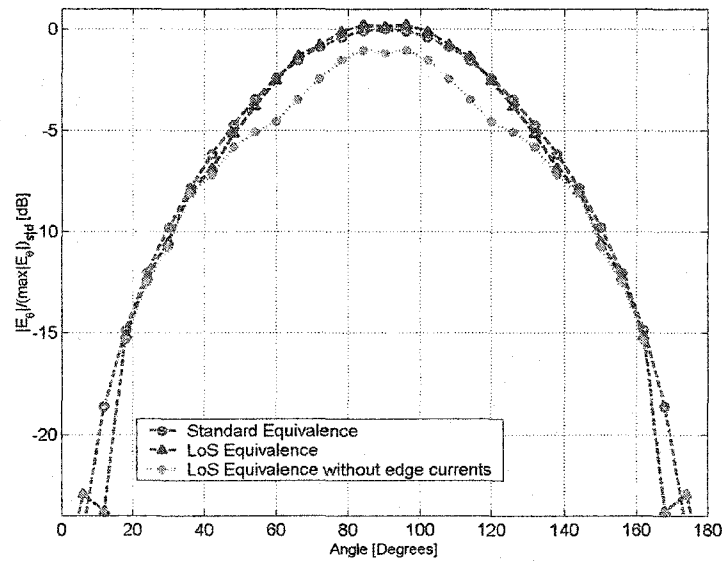


Figure 3.19: Normalized to SE , E_0 radiation pattern of a dipole antenna in log scale

3.4 Practical Examples with the LoS Approximation Using the FDTD Method

This section demonstrates the effectiveness of the LoS approximation. We consider two examples: (i) the dielectric covered dipole antenna and (ii) the rectangular patch antenna. In some antenna simulations, the edge current effect in the LoS approximation is negligible. One such example is a rectangular patch antenna. The edge current effect can be made negligible by placing the top face of the enclosing box very close to the patch. This is demonstrated in section 3.4.2. However, in a dipole antenna, the edge currents play a significant role in the pattern calculation. This is demonstrated in section 3.4.1.

3.4.1 The Dielectric-covered Dipole Antenna

In this example, the Perfectly Matched Layer (PML), which was presented in Chapter 2, is used as an absorbing boundary condition. This allows the absorbing boundary surface to be very close (less than 100 mm) to the antenna. The antenna and the feed structure are embedded into a box of size 120 mm by 200 mm by 100 mm.

We use a non-uniform FDTD technique. The number of cells in the computational domain in the x , y , and z directions is 60, 80 and 50, respectively. The feed structure of the antenna is a square coaxial transmission line of length 100 mm. The inner conductor is of height 1.75 mm, and the outer conductor is of height 5.1 mm. The characteristic impedance is 50Ω . The initial run of the simulation gives the resonant frequency of the antenna, and then with this frequency, the simulation is repeated to obtain the radiation pattern of the antenna. The excitation source used is a Gaussian pulse of width 30 ps, and the total number of iterations is 2000.

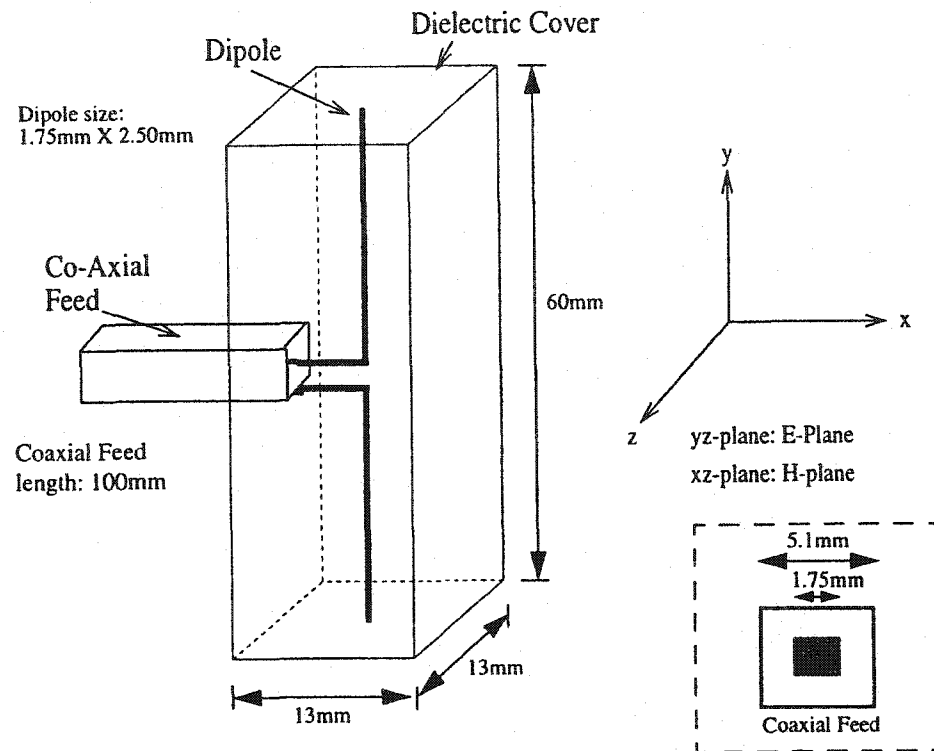


Figure 3.20: The dielectric covered dipole antenna.

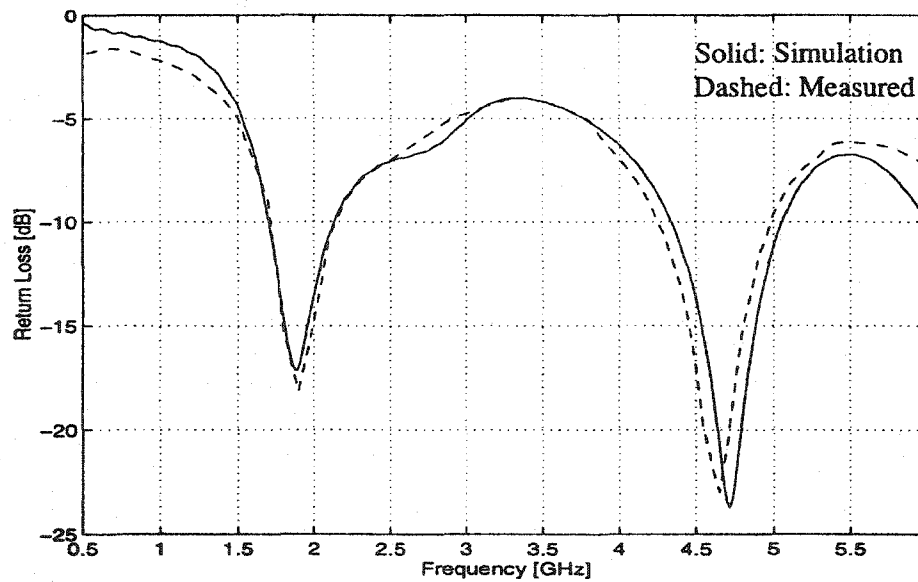


Figure 3.21: Return Loss of the antenna

The simulation and the measurement of the return loss of the antenna are given in Figure 3.21. The resonant frequency of the antenna is determined to be 1.86 GHz. By carrying out Discrete Fourier Transform (DFT) on the surface currents with the known resonance frequency, the time step, and with application of line of sight condition, the radiation pattern is obtained. The measurement and simulation results for the radiation pattern for the E-plane with co-polarization are shown in Figure 3.22.

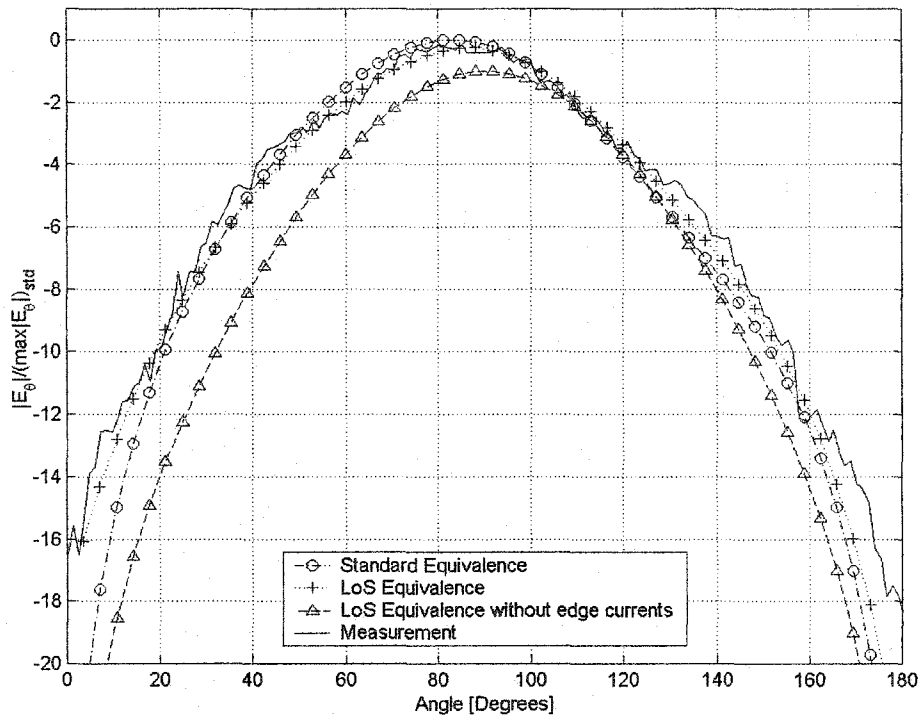


Figure 3.22: The *E*-(half) plane co-polarization radiation pattern of dipole antenna.

From Figure 3.22, one can observe the accuracy of the LoS approximation, which shows very good agreement with the measurements and with the standard equivalence. In addition, Figure 3.22 shows the effect of omitting the edge currents for a dipole antenna. The effectiveness of the LoS approach is in the use fewer surface faces when calculating the radiation pattern. In the above calculation in the half E-plane, only two faces of the

rectangular box are used. In the case of the standard equivalence, one needs to use all six faces of the box. The LoS approximation becomes highly effective when used in radiation pattern optimisation.

3.4.2 The Patch Antenna

The second example is a patch antenna on a finite ground plane. Figures 3.23 shows the antenna configuration used in the simulation, the antenna is of size $80 \times 30 \text{ mm}^2$. The substrate is of relative dielectric constant 2.2 and its height is 1.8 mm. The mesh size used for the simulation is $80 \times 50 \times 80$, and the absorbing condition is the first-order absorbing boundary. The resonant frequency of this antenna is 3.75 GHz and it is obtained from the simulation results as shown in Figure 3.24.

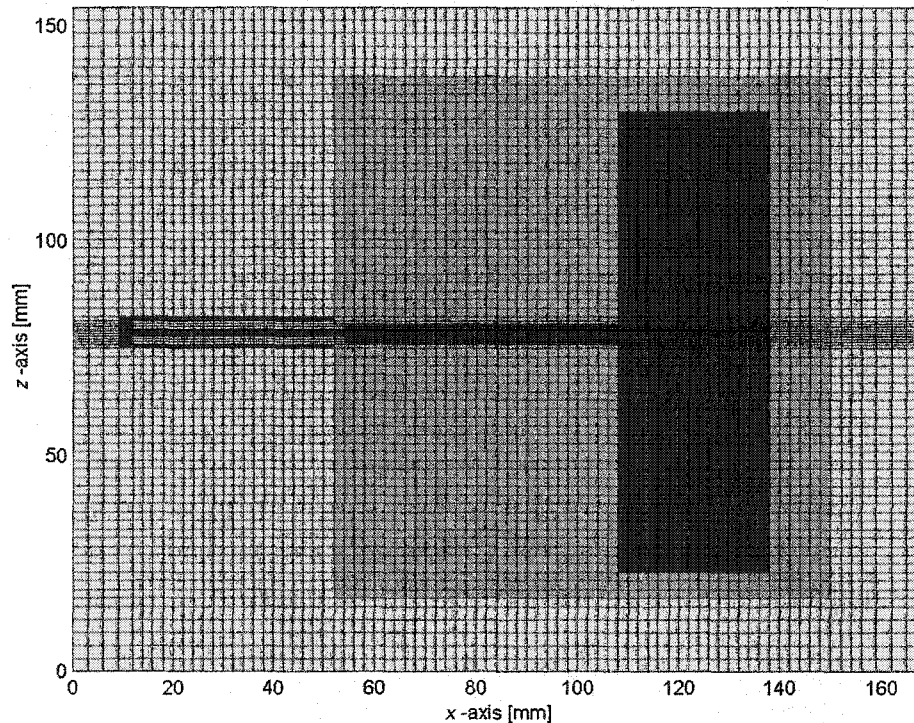


Figure 3.23: The planer view of microstrip rectangular patch antenna.

In the simulation, the top face of the enclosing box was placed at a distance of less than 10 mm from the patch, thus annulling the requirement of the inclusion of edge currents on the overall pattern calculation. Figures 3.25 through 3.26 show the simulation results for the radiation patterns in the main two planes.

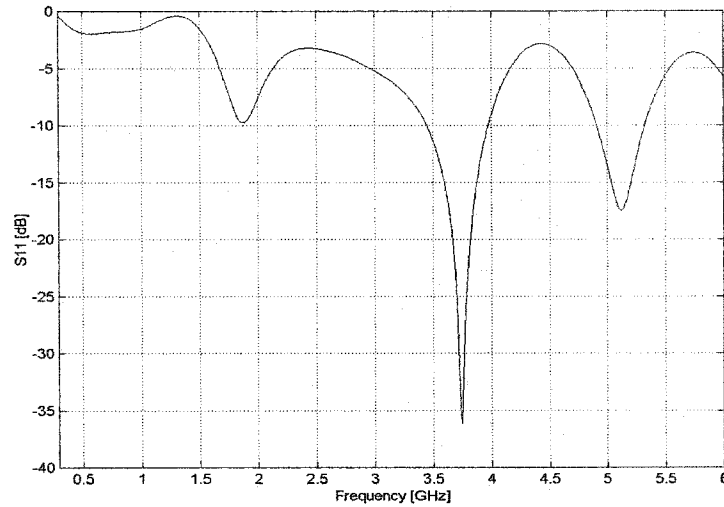


Figure 3.24: The Return Loss of the patch antenna.

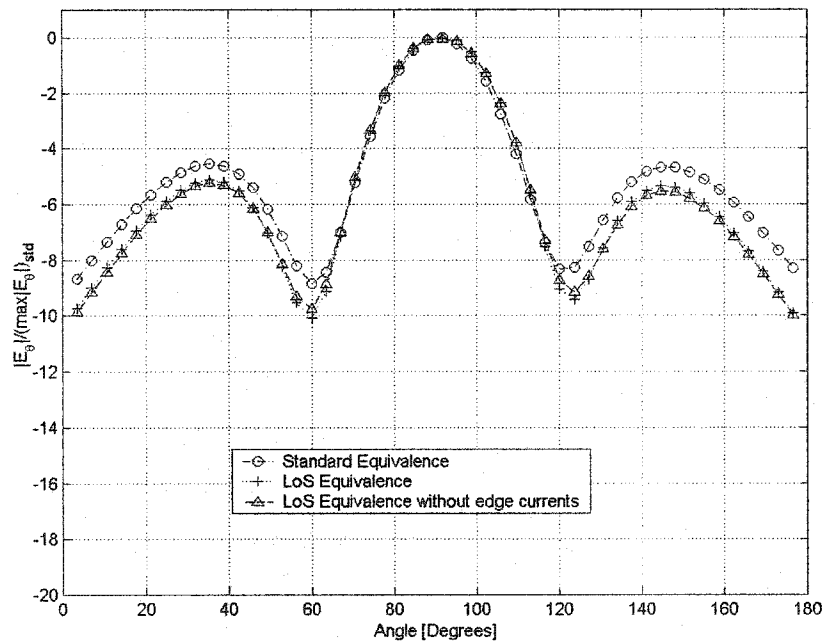


Figure 3.25: The H -plan co-polarization radiation pattern of patch antenna.

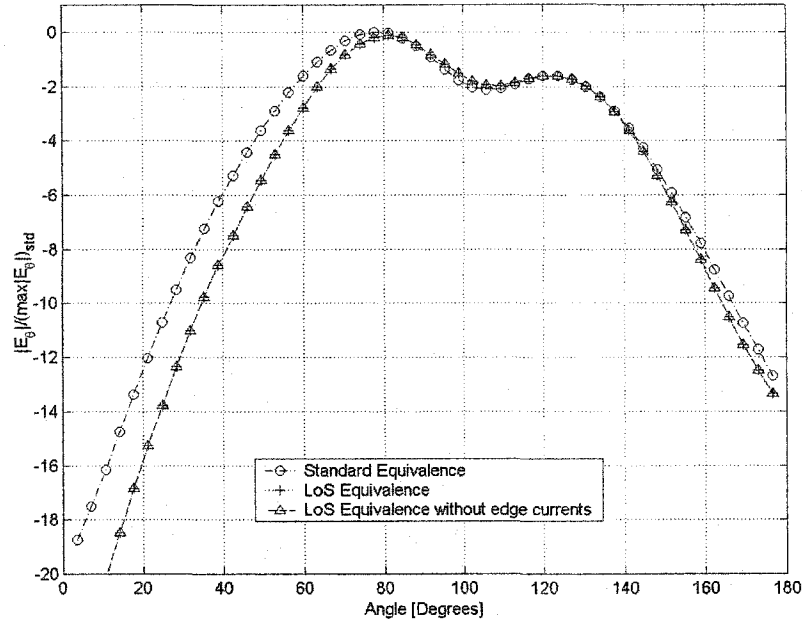


Figure 3.26: The E -plan co-polarization radiation pattern of patch antenna.

In this example of the rectangular patch antenna there was good agreement between the radiation patterns obtained through the three different methods. From the simulation results, we can conclude that for planar antennas, the edge current has negligible effect on the radiation pattern.

3.5 Summary

In this chapter, a new approach to the computation of far-field radiation pattern using the equivalence principle is presented. The validity of the LoS approach is shown with an application to a practical problem of calculating the radiation pattern of a dipole antenna. The simulation results show remarkable agreement between the LoS approach and the standard equivalence method, the approximation error is within the acceptable levels and it matches

the theoretical prediction. The efficiency of the LoS approach as compared to the standard equivalence principle in the calculation of radiation patterns is due to the reduced size of the integration surface, which requires less computational time. Furthermore, it was demonstrated that the use of one type of surface current in the LoS is sufficient to obtain radiation pattern for antennas, and this further reduces the computational time.

The efficiency of the LoS approximation is demonstrated through antenna analysis with the FDTD method. This technique reduces the computational time and the memory requirement in the FDTD simulations. The computational time for the LoS approach is approximately one-sixth of that required by the standard equivalence. Thus, the LoS approach is an efficient alternative to existing standard algorithms for the computation of far-field patterns in high-frequency structure simulators. The work presented in this chapter has been accepted by the peers in the electromagnetic community as a significant contribution and it can be found in the literature [15].

3.8 References

- [1] J.A. Stratton, *Electromagnetic Theory*, New York: McGraw Hill, pp. 482-488 and 196-197, 1941.
- [2] R. F. Harrington, *Time-Harmonic Electromagnetic Fields*, New York: McGraw Hill, pp. 101-103, 120-123, 106-109, 77-79 and 129-134, 1961.
- [3] C.A. Balanis, *Advanced Engineering Electromagnetic*, New York: John Wiley & Sons, pp. 329-342 and 279-291, 1989.
- [4] A. Rubinowicz, "The Miyamoto-Wolf diffraction wave," *Progress in Optics*, vol.4, pp. 201-240, 1965.
- [5] F. Kottler, "Diffraction at a black screen, part 2: Electromagnetic theory," *Progress in Optics*, vol.6, pp. 335-377, 1967.

- [6] Ken-ichi Sakina, Suomin Cui and Makoto Ando, "Mathematical investigation of modified edge representation," *IEEE Antenna and Propagation Symposium*, vol.1, pp. 386-389, 2000.
- [7] John Asvestas, "The physical optics fields of an aperture on a perfectly conducting screen in terms of line integrals," *IEEE Trans. Antenna and Propagation*, vol. AP-34, pp. 1155-1159, 1986.
- [8] P. Beckmann, *The Depolarisation of Electromagnetic Waves*, The Golem Press, Boulder, Co, pp. 76-92, 1968.
- [9] R. F. Harrington, "On scattering by large conducting bodies," *IRE Trans. Antennas Propagation*, vol. AP-7 number 2, pp. 150-153, April 1959.
- [10] J. Berenger, "A Perfectly Matched Layer for the Absorption of Electromagnetic Waves," *Journal of Computer Physics*, pp. 185-200, 1994.
- [11] N. T. Sangary, *Theoretical and Experimental Investigations on the Equiangular Spiral Antenna*, M.Eng thesis, McMaster University, 1994.
- [12] V. H. Rumsey, "Reaction Concept in Electromagnetic Theory," *Physical Review*, volume 94, number 6, pp. 1483-1491, June 1954.
- [13] S. A. Schelkunoff, "Some Equivalence Theorems of Electromagnetic and Their Application to Radiation Problems," *The Bell System Technical Journal*, pp. 92-112, 1931.
- [14] D. A. B. Miller, "Huygens's wave propagation principle corrected," *Optical Letters*, volume 16, number 18, pp. 1370-1372, September 1991.
- [15] N. T. Sangary, and Natalia Georgieva, "Line-of-Sight Approximation to the Equivalence Principle for Far-field Computations," *URSI International XXVII General Assembly*, Symposium Digest, pp. 34-36, August 2002.
- [16] N. T. Sangary, and Natalia Georgieva, "Line-of-Sight Approximation to the Equivalence Principle," *IEEE Trans. Antennas Propagation*, submitted 15 Sep. 2002, Manuscript No. AP0209-0445.

Chapter 4

Antenna Analysis with the FDTD Method

4.1 Introduction

In this chapter, new antennas are introduced and simulations of these antennas are carried out with the non-uniform FDTD technique. In addition to the use of non-uniform mesh and the PML absorbing boundary condition, the concept of an integrated feed structure is introduced to the antenna simulation. The use of the PML allows the absorbing boundary to be placed closer to the antenna structure thus reducing the grid size and improving the accuracy. When applying the Absorbing Boundary Condition (ABC) to antenna simulations, the proximity of the boundary needs special consideration. This is because for some antennas such as the dipole, the placement of the ABC close to the antenna has undesirable effects, whereas for a patch antenna the proximity of the ABC has little effect in the simulation results. This is because for the dipole antenna, the field intensity in the space surrounding the antenna sets the resonance of the antenna, and any obstruction of these fields with an ABC has a significant effect in the simulation results. In contrast, for patch antennas, since the fields in the space between the patch and the ground plane form the resonance, the effect of the ABC proximity is less.

In almost every antenna, the feed point and the structure in its proximity have significant effect in determining the input impedance of the antenna. Due to this, in our

scheme the feed structure (coaxial line) is part of the antenna, thus no interpolation schemes are necessary between the interfaces formed by the juxtaposition of different meshes. Through numerous simulations and experimental verifications it is found that a square coaxial feed at the input of the antenna could be modelled with same level of accuracy in the simulation results, as for a circular coaxial feed. The return loss at the antenna input is obtained from the time domain field at a point in the coax feed and this was addressed in detail in Chapter 2.

In order to show the effectiveness of the FDTD technique, the antennas presented are from different categories with different shapes and sizes. The main features of the proposed antennas are the small size for mobile units and high gain for the base station antennas. With these choices of antennas we can address some of the main challenges facing the FDTD technique. They include: the detailed structures in small antennas and larger cell size in modelling large antennas. The FDTD technique has been widely used in antenna analysis [1], [2] and [3]. A similar form is adopted in the antenna simulations in this thesis.

4.2 The Coaxial Transmission Line

In many antenna analyses the modelling of the feed point has been ignored to a large extent. However, the feed point of the antenna is an important factor in its analysis. In some antenna analyses in the literature, in which the feed point of the antenna was considered, a coaxial feed was modelled with unnecessary accuracy and this resulted in larger computer memory usage and longer computational time. In our analysis, we have chosen a square coaxial line as the feed line and this structure can be easily incorporated into the modelling of the antenna. One should avoid the use of microstrip or strip-line feed, because it is not possible to excite a single mode (pure TEM) in these feed lines and the extraction of the reflected wave from a multimode wave is very difficult.

Through experimental investigation, it is found that if the ratio of the inner to the outer width of the conductor is 2.89 and with dielectric filling of unity, the characteristic impedance of the line is 50 Ohm. Since one may use different characteristic impedance other

than 50 Ohms, different conditions were examined. Figure 4.1 gives the ratio of inner (a) to outer (b) width (or radius) of the coax conductors at the frequency point of 1GHz and the size of coaxial line can be scaled to the desired frequency. In addition, this figure contains plots with different dielectric constants. One could see that the impedance is inversely proportional to the square root of the dielectric constant $z \propto 1/\sqrt{\epsilon_r}$, as expected.

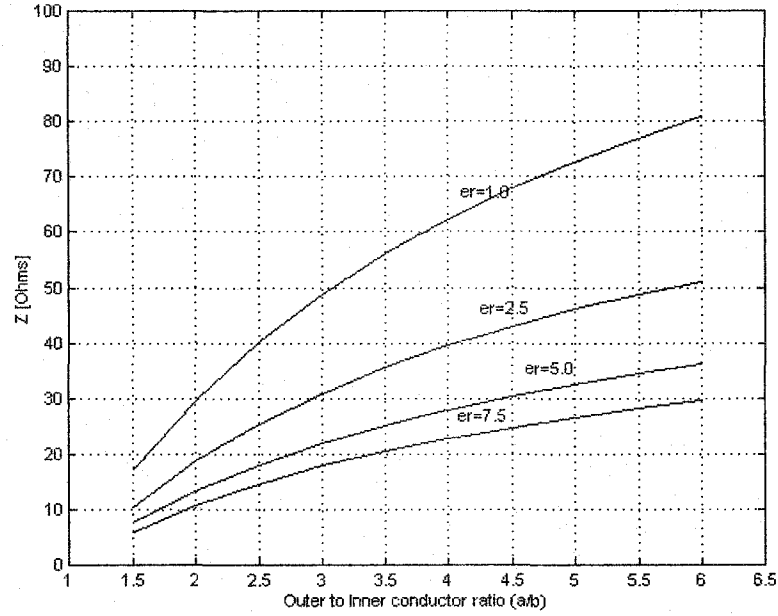


Figure 4.1: Characteristic impedance of the square coaxial line.

With three variables a , b and ϵ_r , while maintaining the desired characteristic impedance, the non-uniform mesh can be made to fit any feed point of the antenna. The accuracy and the limitations of the square coaxial feed line are discussed in chapter two.

We have chosen three different categories of antennas and they are mobile unit antennas, window antennas and base station antennas. Antennas were put in different categories for their different size and shapes; in each category, we selected more than one antenna to demonstrate the capability of the FDTD simulations. The simulation results presented in this chapter are only for the return loss and the radiation patterns are obtained from measurement data. Chapter 3 contains the detailed discussion on the radiation pattern simulation.

4.3 Mobile Unit Antennas

In this category of antennas, the size and the shape of the antenna are the important features, and in many instances the antennas have to be designed for specific applications. In modelling small antennas with unique shapes, the challenge one faces is the detail of the structure. Once again, the non-uniform FDTD technique proves to be advantageous. In this category, we present three different antennas, namely, the Coupled Patch Antenna, the Printed Sleeve Antenna and the Sandwich Antenna.

4.3.1 Coupled Patch Antennas

Figure 4.2 shows the coupled patch antenna (CPA). This antenna is different from the traditional monopole, i.e., the reflecting plane is not large, and the strip length is much less than a quarter wavelength. Both, the size of the reflecting plane and the length of the strip set the resonant condition of the antenna. The antenna is for the operating frequency of 0.9 GHz and it is for the application in PCMCIA, and the shape of the antenna confines to the PCMCIA card. The size of the reflecting plane is $B=1.2 \lambda$, $A=0.17 \lambda$, length of the strip $L=0.15 \lambda$, the dielectric constant of the substrate is 4.00, and the thickness of the substrate is 0.06λ . The gain of the antenna is 2.6 dBi and maintains a constant level of performance despite the change in the environment. The bandwidth is 12%. The measured radiation patterns in two principal planes are shown in Figures 4.4 and 4.5. The comparison between the simulation and the measurement results of the return loss is given in Figure 4.3. The size of the non-uniform FDTD mesh used for this analysis was $90 \times 72 \times 70$. The operation of this antenna is somewhat similar to a dipole antenna, where one arm is a plane and the other arm is a stub. The wider bandwidth is achievable, because one section of the antenna is large. The operating frequency of the antenna is set by the both plane and the stub. The variation of the operating frequency as a function of the plane size and stub length is given in [3].

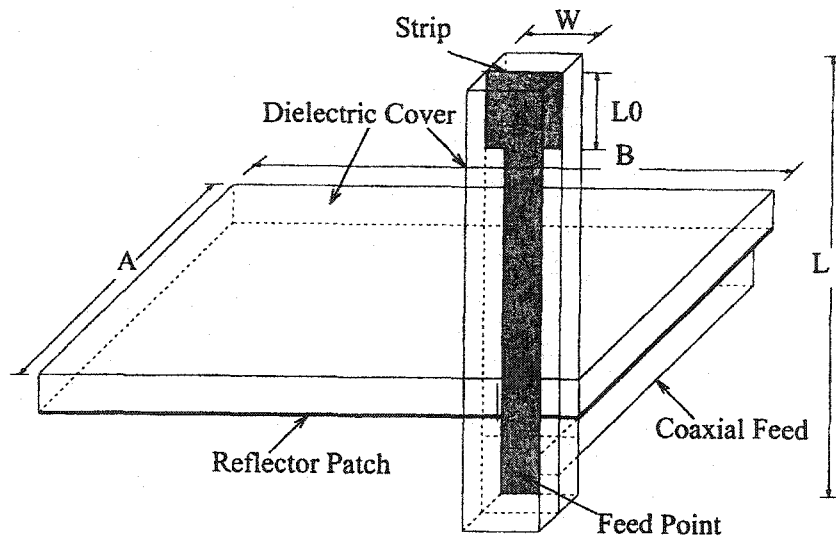


Figure 4.2: Coupled Patch Antenna (CPA).

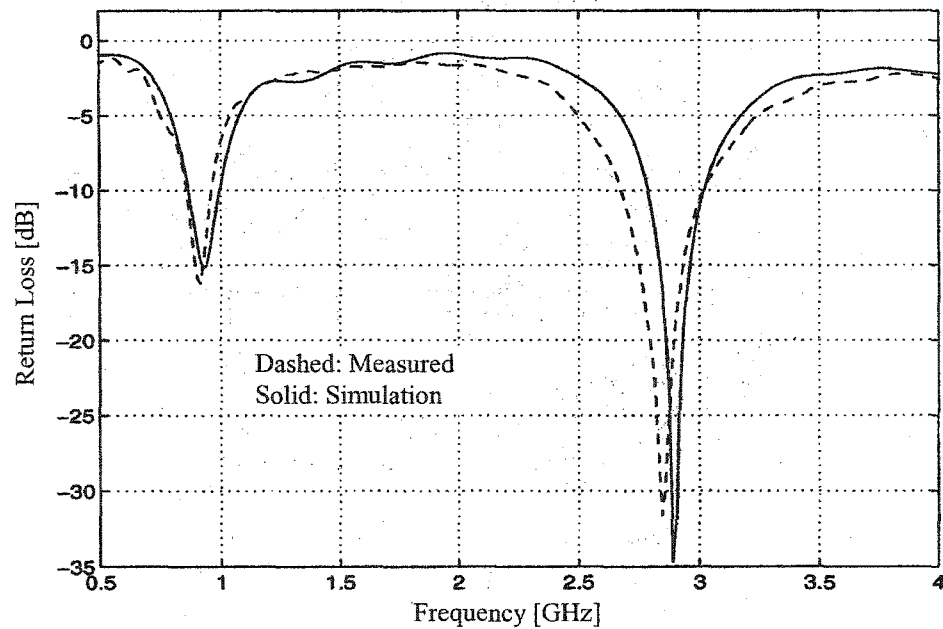


Figure 4.3: Return Loss of CPA.

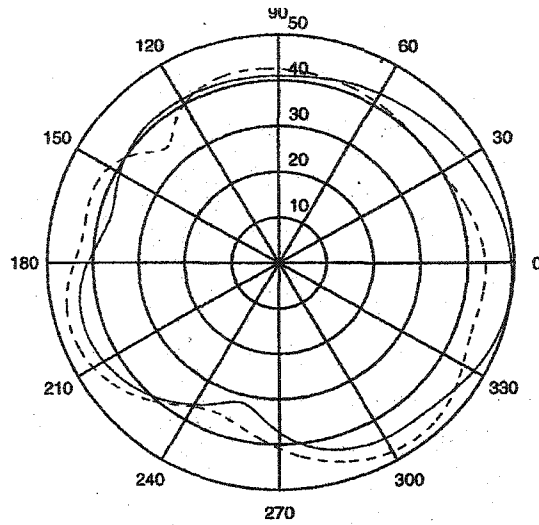


Figure 4.4: Radiation Pattern, H-plane (CPA), solid co-pol, dashed: x-pol.

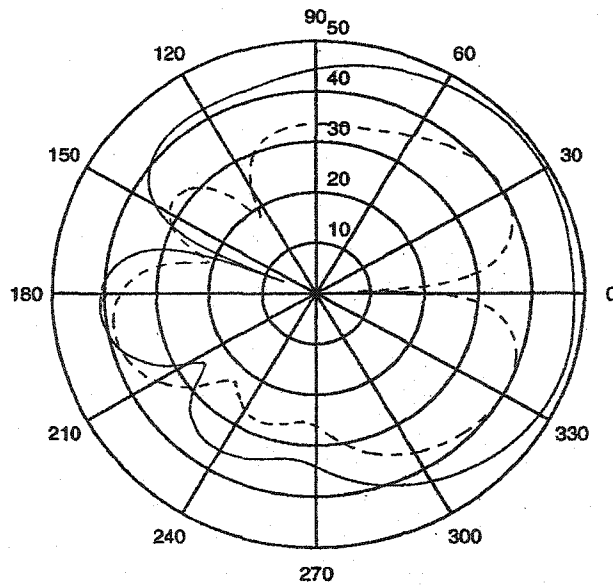


Figure 4.5: Radiation Pattern, E-plane (CPA), solid co-pol, dashed: x-pol.

4.3.2 Printed Sleeve Antenna

We have extended the concept of an ordinary sleeve antenna to a printed structure and the antenna is shown in Figure 4.6. In this antenna, the length is similar to a dipole antenna but with the matching at the end rather than at the centre. The substrate used has $\epsilon_r = 3.0$, width $W = 0.08 \lambda$, length $L = 0.4 \lambda$ and the substrate thickness $H = 0.01 \lambda$. The antenna was designed to work at 0.9 GHz (a specific requirement for the MPT product developed by Research In Motion). The gain of the antenna is 5.2 dBi with an input impedance bandwidth of 25%. The radiation pattern is maximum in the elevation angle of 30 to 70 degrees. The comparison between the simulation and the measurements of return loss is given in Figure 4.7. The size of the non-uniform FDTD mesh used was $55 \times 45 \times 90$. The radiation pattern of the antenna in E-plane and H-plane are shown in Figures. 4.8 and 4.9.

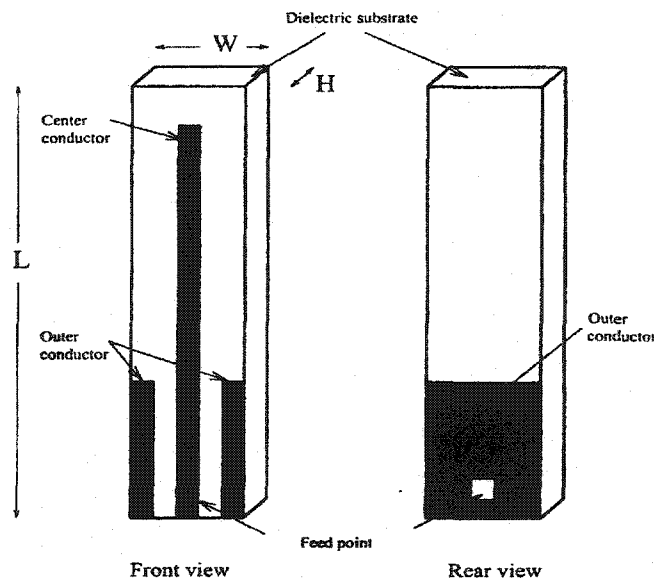


Figure 4.6: Printed Sleeve Antenna (PSA).

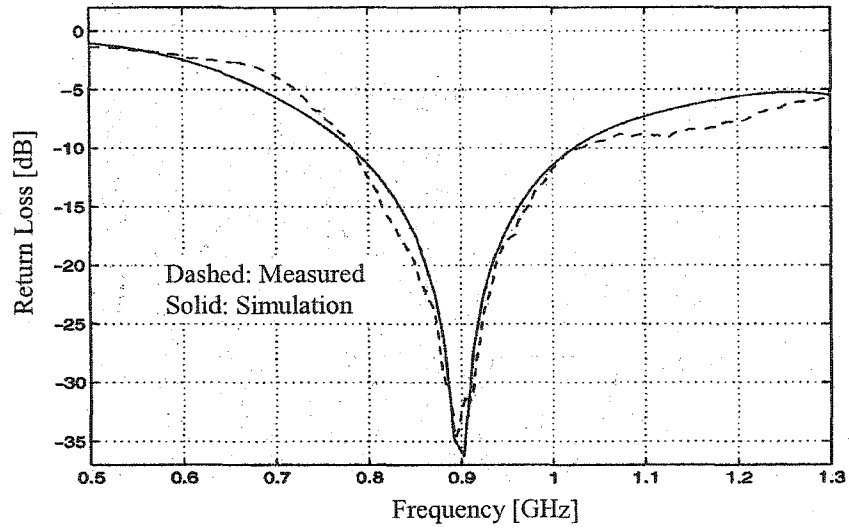


Figure 4.7: Return Loss of PSA.

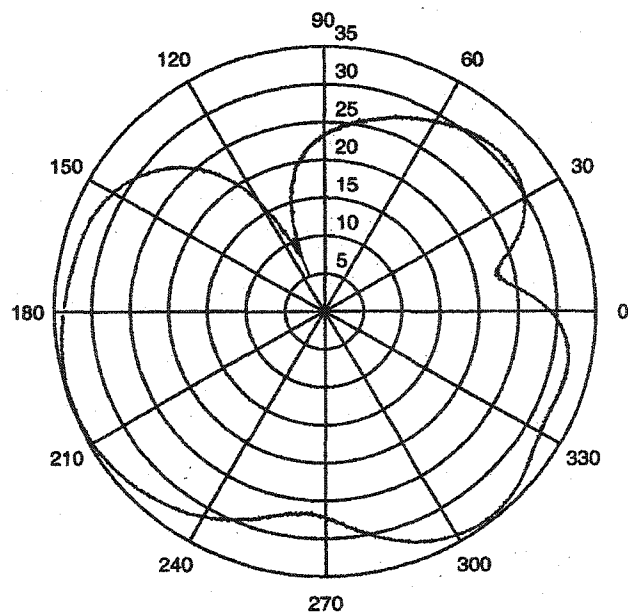


Figure 4.8: Radiation Pattern, H-plane (PSA), co-pol.

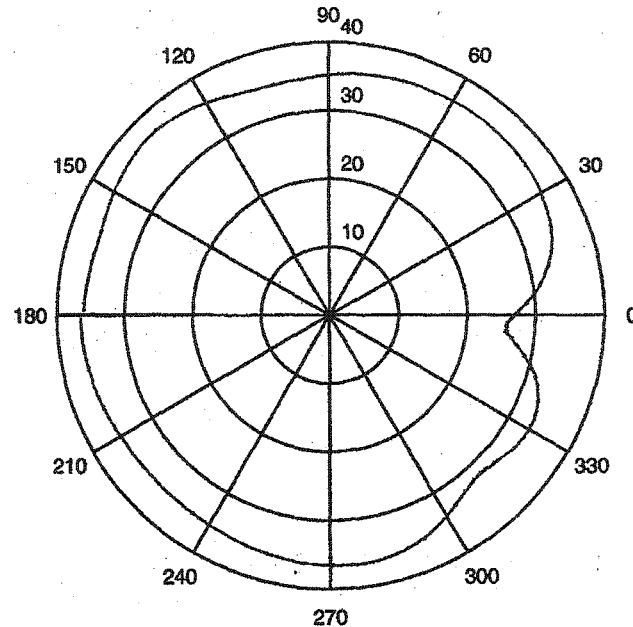


Figure 4.9: Radiation Pattern, E-plane (PSA), co-pol.

4.3.3 Sandwich Antenna

Figure 4.10 shows a sandwich antenna. The operation of the antenna is rather peculiar. This antenna has three planes; namely, the ground plane, the matching plane, and the radiating plane. The radiating plane is not at the same potential as the ground, thus implying that the matching circuit is not of a stripline nature. In this design, we have used a folded line for matching. The antenna is very small in size, the length and width are $L=0.3\lambda$ and $W=0.04\lambda$. The simulation and measurement for S_{11} is given in Figure 4.11. The size of the non-uniform FDTD mesh used for this antenna analysis is $55 \times 100 \times 50$. In terms of antenna performance, the gain was 2.0 dBi, the input impedance bandwidth is 6%, and the polarisation is elliptical. The radiation patterns of this antenna are given in Figures 4.12 and 4.13.

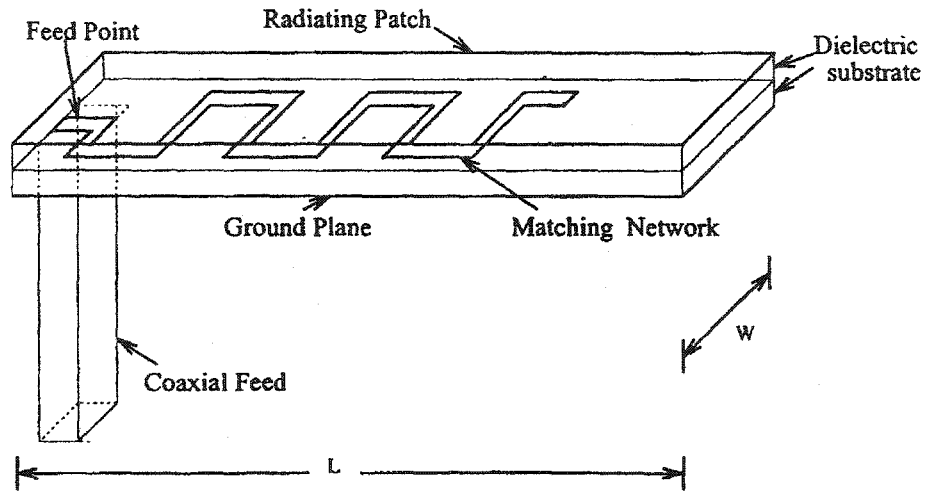


Figure 4.10: Sandwich Antenna (SA).

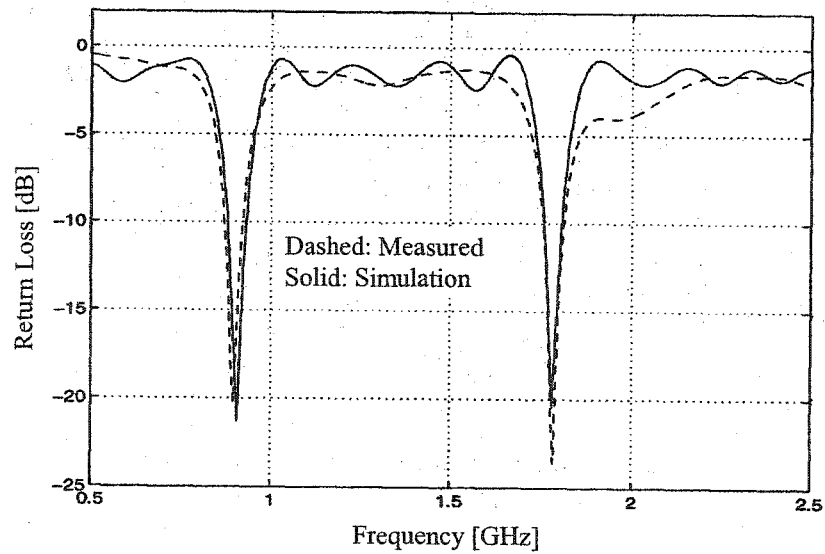


Figure 4.11: Return Loss of SA.

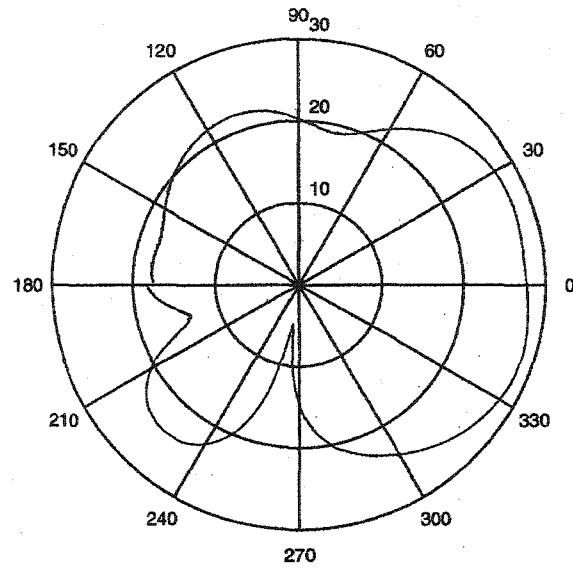


Figure 4.12: Radiation Pattern, H-plane (SA).

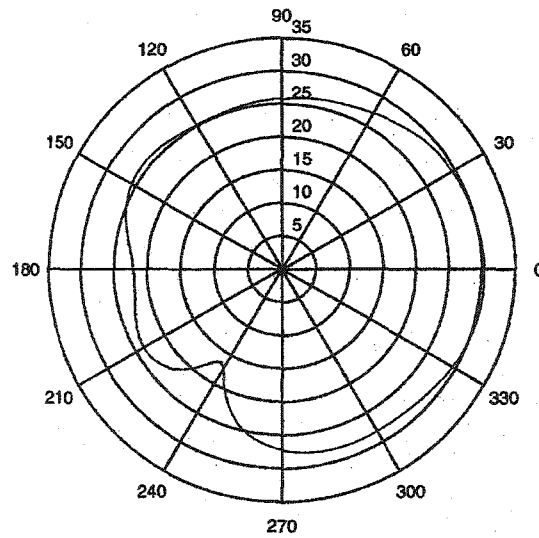


Figure 4.13: Radiation Pattern, E-plane (SA).

4.4 Window Antennas

Window antennas are designed to be thin low-profile structures. They are single layer antennas that can be stuck to a window. In Figure 4.14 a typical window antenna is shown. The length of the ground line and the length of the centre line determine the operating frequency of the antenna. The width and the length of this particular antenna are $W=0.20\lambda$ and $L=0.25\lambda$ respectively. The antenna uses a plexiglass substrate with a relative dielectric constant of $\epsilon_r = 2.90$. Since the coupling of the fields is mostly from outside the substrate, the value of the substrate does not affect the performance of the antenna very much. The gain is 2.6 dBi. The polarisation is elliptical and the input impedance bandwidth is about 20%. The measurement and simulation results at the input terminal of the antenna are given in Figure 4.15. The radiation patterns are given in Figures 4.16 and 4.17. The size of the non-uniform FDTD mesh used for this simulation is $80 \times 80 \times 50$. The design principles for this particular window antenna can be extended to numerous different antenna patterns on a single layer.

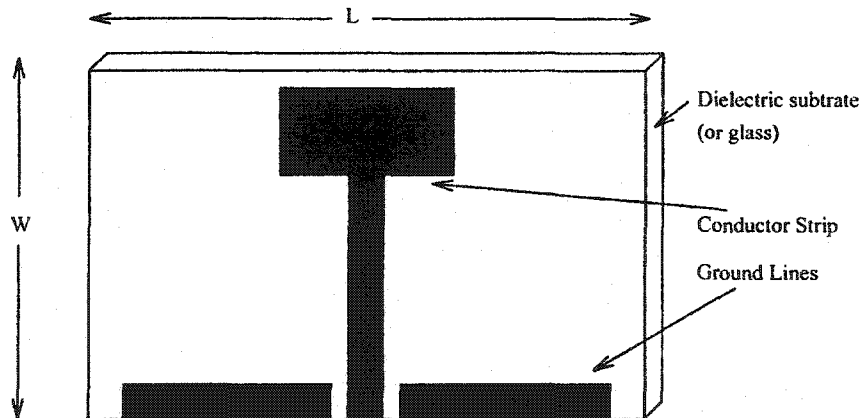


Figure 4.14: Window Antenna (WA).

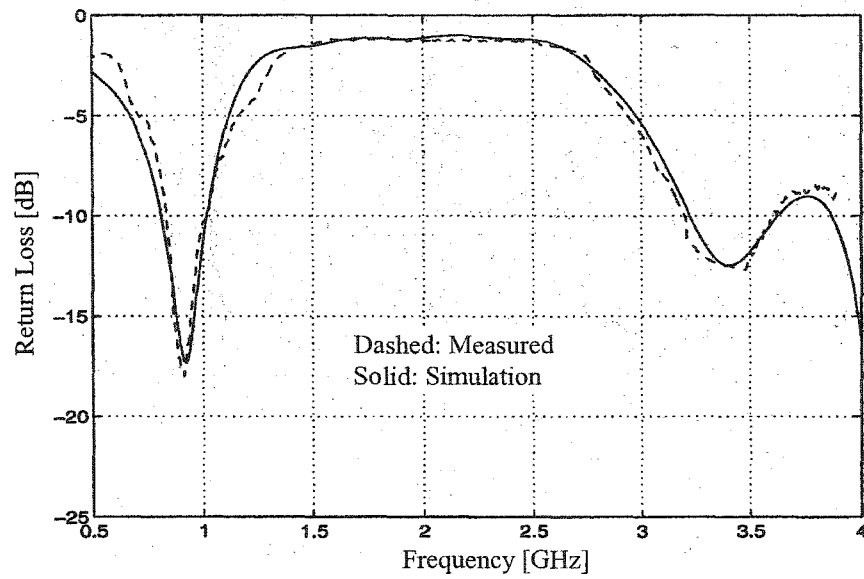


Figure 4.15: Return Loss of WA.

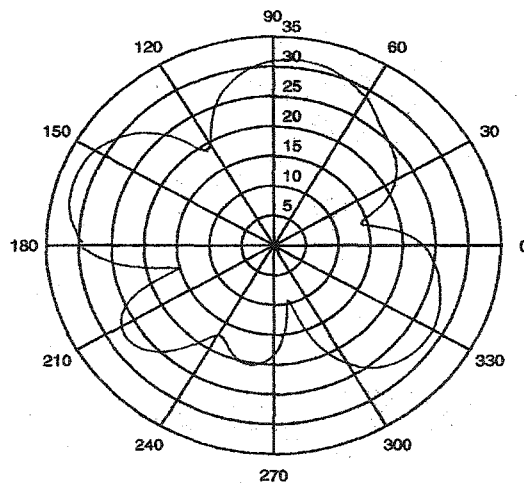


Figure 4.16: Radiation Pattern, H-plane (WA).

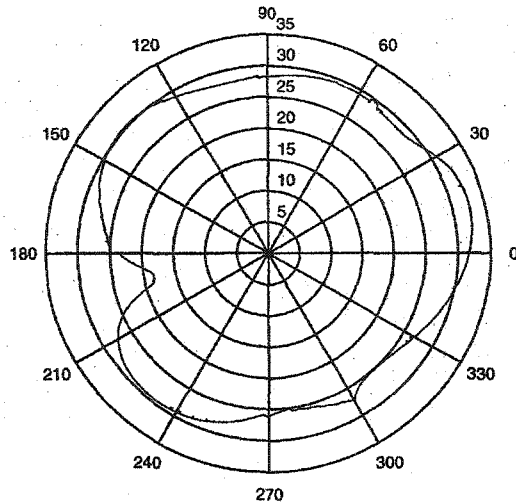


Figure 4.17: Radiation Pattern, E-plane (WA).

4.5 Base Station Antennas

The base station antennas are required to have high gain. The size of the base station antenna is not a stringent requirement. However, extremely large arrays are not preferred. In our analysis we chose an antenna that is large in size and has a gain of more than 6dBi. The biggest challenge in analysing large antennas using the FDTD method is the number of the cells and cell size. In this respect the non-uniform mesh is the best solution. In this category, we analysed the following antennas: the folded dipole antenna backed by a reflector plane and a simple window antenna. As our goal is to demonstrate the effectiveness of FDTD technique, only the simulation of return loss is considered.

4.5.1 Co-Planer Patch Antenna

This antenna has a gain of about 6 dBi; the operating frequency is controlled by the length of the line and the distance of the reflector plane. The antenna is narrow band with a

bandwidth of less than 5%. The different planes of the antenna are shown in Figure 4.18, and more detail on the operation of the antenna can be found in [3]. In the FDTD analysis the number of cells used are $81 \times 50 \times 80$. The simulation and measurement result for the return loss is given in Figure 4.19.

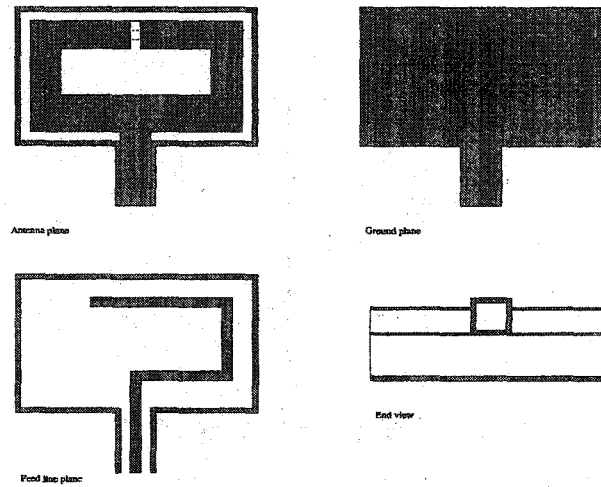


Figure 4.18: Co-Planar Patch Antenna (CPPA).

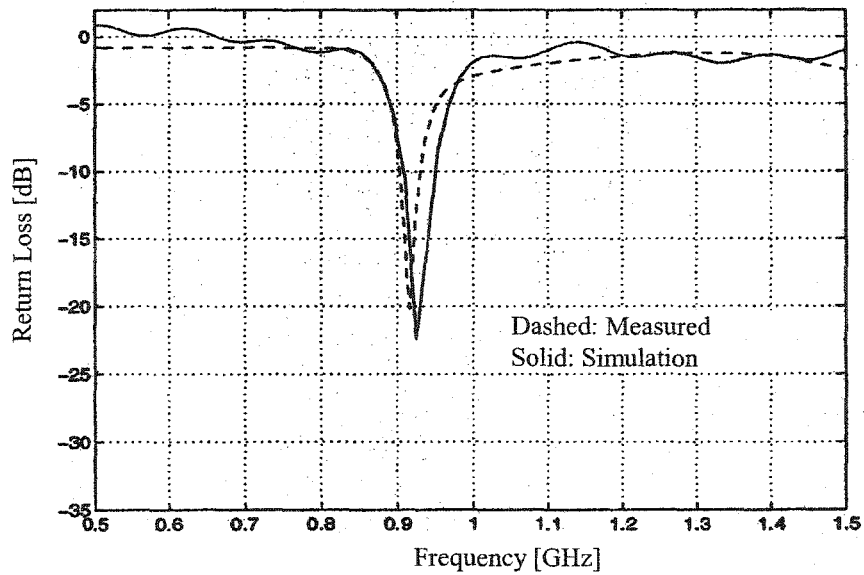


Figure 4.19: Return Loss of CPPA.

4.5.2 Printed Loop Antenna

This antenna is similar to the antenna given in [4], but this antenna functions without a ground plane. Therefore, this antenna (see Figure 4.20) can also be categorised as a window antenna. The gain of the antenna without the ground (reflector) plane is in the order of 6 dBi and has a bandwidth of about 20%. With a non-uniform mesh, the dimension is 70 x 60 x 30. The polarisation of the antenna is linear with the cross polarisation of less than 15dB in the principal planes. The return loss is given in Figure 4.21.

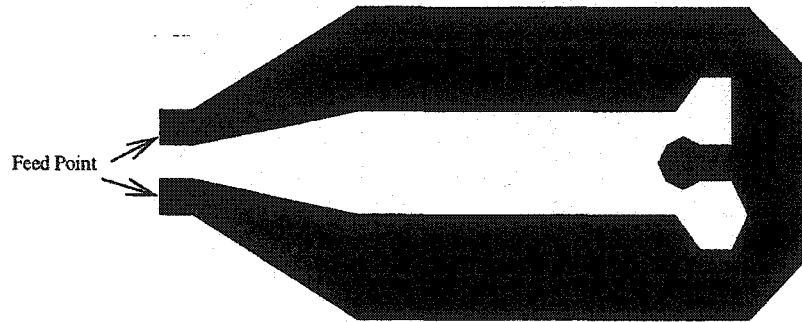


Figure 4.20: Printed Loop Antenna (PLA).

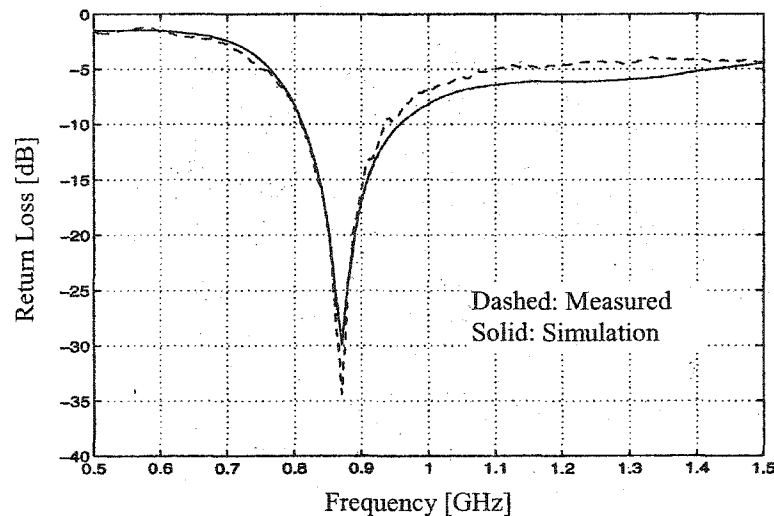


Figure 4.21: Return Loss of PLA.

4.6 Summary

In this chapter, we have given simulation and measurement results for some new antenna configurations. The simulation and measurement results are in good agreement, thus proving the accuracy and the versatility of the FDTD method. Using FDTD techniques one could ascertain the sensitive geometrical parameters of the antennas. As an example, in the case of CPA, the patch size rather than the vertical element determines the resonant frequency and this would not be that obvious with an analytical analysis.

4.7 References

- [1] K. S. Yee, "Numerical solution of initial boundary value problems involving Maxwell's equations in isotropic media," *IEEE Trans. Antennas and Propagation*, vol.14, pp. 302-307, May 1966.
- [2] N. T. Sangary, E. A. Navarro, C. Wu and J. Litva, "Application of non-uniform FDTD method to PCS antennas," *IEEE AP-S Int. Symposium Digest Antennas and Propagation*, pp. 1148-1151, June 1995.
- [3] E. A. Navarro, N. T. Sangary, C. Wu and J. Litva, "Analysis of a coupled patch antenna with application in personal communications," *IEE Pro.-Micro. Antennas and Propagation*, Vol. 142, pp. 495-499, 1996.
- [4] M. Cai and M. Ito, "New type of printed polygonal loop antenna," *IEE Proceedings H*, vol. 138, No. 5, October 1991.

Chapter 5

Error Analysis of the Non-Uniform FDTD Method

5.1 Introduction

A non-uniform mesh has a number of advantages over a uniform mesh and this was evident in the antenna analysis using the FDTD technique considered in Chapter 4. In the FDTD technique, the central finite difference approximation is applied to the first order derivative. Although this approximation undoubtedly creates errors in the solution, these errors may be insignificant depending on the method of implementation. Specifically, by expressing the central finite differences by Taylor series, one can show that the error is of second order for the case of a uniform mesh. The same does not hold for a non-uniform mesh.

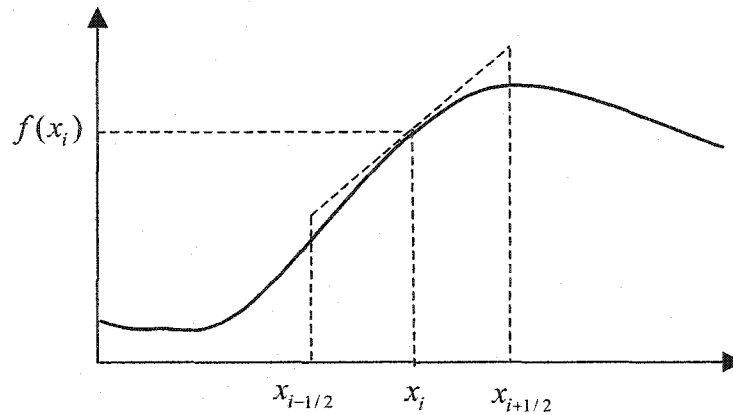


Figure 5.1: Finite-difference approximation of first-order derivative.

Using the Taylor series approximation for the first derivative in terms of x we can write

$$f'(x_i) = \frac{f(x_{i+1/2}) - f(x_{i-1/2})}{\Delta x_{i-1/2} + \Delta x_{i+1/2}} - \frac{(\Delta x_{i-1/2}^2 - \Delta x_{i+1/2}^2)f''(x_i)}{2(\Delta x_{i-1/2} + \Delta x_{i+1/2})} - \frac{[\Delta x_{i+1/2}^3 f'''(x_{i-1/4}) + \Delta x_{i-1/2}^3 f'''(x_{i+1/4})]}{6(\Delta x_{i-1/2} + \Delta x_{i+1/2})} + \dots \quad (5.1)$$

where

$$\Delta x_{i-1/2} = \frac{x_i - x_{i-1}}{2}, \quad \Delta x_{i+1/2} = \frac{x_{i+1} - x_i}{2}.$$

In the above expression, the terms $\Delta x_{i+1/2}$ and $\Delta x_{i-1/2}$ are the lengths of the corresponding cells. If these terms are equal, which is the case for a uniform mesh, then the second term in (5.1) is zero. Therefore, if we approximate the first order derivative as

$$f'(x_i) \approx \frac{f(x_{i+1/2}) - f(x_{i-1/2})}{\Delta x_{i-1/2} + \Delta x_{i+1/2}}, \quad (5.2)$$

then this approximation has second order accuracy.

In the case of a non-uniform mesh, the lengths of the cells $\Delta x_{i-1/2}$ and $\Delta x_{i+1/2}$ are unequal. The second order term in (5.1) is not zero, thus, equation (5.2) has only first order accuracy.

The implementation of the FDTD technique in EM theory is carried out via Yee's method, which uses the leapfrog scheme. In this scheme, the electric field components are on the edges of the cells, and the magnetic field components are on the centroid of the cells' surfaces. In any given direction, the latter corresponds to the midpoint of the cell length. Therefore, the magnetic field components, which are obtained by finite difference approximation of electric field components, have second order accuracy. This does not apply to the electric field component. This is because the magnetic field component points are not equidistant from the electric field component points, resulting in a non-uniform scheme.

Although locally the non-uniform orthogonal mesh has only a first-order accuracy, globally this scheme can have a second-order accuracy in space, a phenomenon known as supraconvergence [5] [6] [7]. In addition to this global second-order convergence, non-uniform meshes give rise to a number of consistency and stability phenomena, which have no counterpart on uniform grids. In our research we intend to show this supraconvergence phenomenon for Maxwell's equations, and explore some of its aspects in non-uniform meshes.

5.2 Second Order Error Analysis

In evaluating any technique, the variable to be tested should be isolated from the other variables. It is very difficult to remove the effects of all the other variables from the variable under test, and so the best solution is to choose a simple case with minimum effects from the untested variables. Furthermore, it is best if the problem has an analytical solution, so that an accurate comparison is possible. One of the simplest problems is a resonant cavity box. However, since this high Q structure does not involve any wave propagation, the error analysis on it may not mimic a typical problem that involves the FDTD method. A waveguide structure is the most suitable for error analysis relevant to our problems.

The error analysis using the rectangular waveguide is carried out with a number of varying conditions such as variations of the absorbing boundary conditions, and variations in the uniformity of the mesh. We carry out a numerical investigation of the accuracy of the non-uniform FDTD method. The computer simulations show that the use of non-uniform grids with the FDTD method yields numerical field values that have second order accuracy with respect to cell dimensions. This accuracy is possible if the boundary condition is perfectly or highly absorptive. With imperfect boundary conditions, the accuracy degrades to first order. We demonstrate this with a homogeneous Dirichlet boundary condition, the perfect dispersive boundary condition for waveguides [2], and the perfectly matched layer [3,4].

5.2.1 Error Analysis with Homogeneous Dirichlet Boundary Conditions

The FDTD method is used to obtain the TM_{11} mode in a rectangular waveguide following the procedure given by Navarro et al. [7]. The TM_{11} field distribution is analytically known; thus, the difference between the field obtained numerically and that obtained analytically gives us an estimation of the numerical error when the FDTD method is applied with a non-uniform mesh. The electromagnetic field is introduced into the x - y transversal section of the waveguide by using a time domain pulse, consisting solely of the E_z component. The time domain pulse resonates within a two-dimensional slice of the waveguide and the first resonant field corresponds to the TM_{11} mode [8]. The field corresponding to the TM_{11} mode is extracted from the FDTD time domain field by applying the discrete Fourier transform at each node of the mesh. The TM_{11} mode is compared with analytical values to evaluate the errors generated at the nodes of (a) a non-uniform mesh with abrupt changes in the cell dimension, and (b) gradually changing non-uniform meshes. In every case the dimensions of the mesh in the y -direction are kept constant, in order to keep the error due to discretization in the y -direction constant and second order. The cross section of the waveguide used in this analysis has dimensions 2.286 cm by 1.16 cm.

We first show the numerical second-order error generated using a uniform mesh. The lines of constant E_z , obtained with a 50 by 40 grid, are shown in Figure 5.2.

Figure 5.3 shows log/log plots of both the maximum error versus cell size, and the average error versus cell size. Using the least squares method for curve fitting a straight line the slope of the line is determined, a built-in function in Matlab® was used for the calculation. In both cases, the result confirms the theoretical prediction of second order accuracy. The maximum error has a slope of 2.359 and the average error has a slope of 2.344.

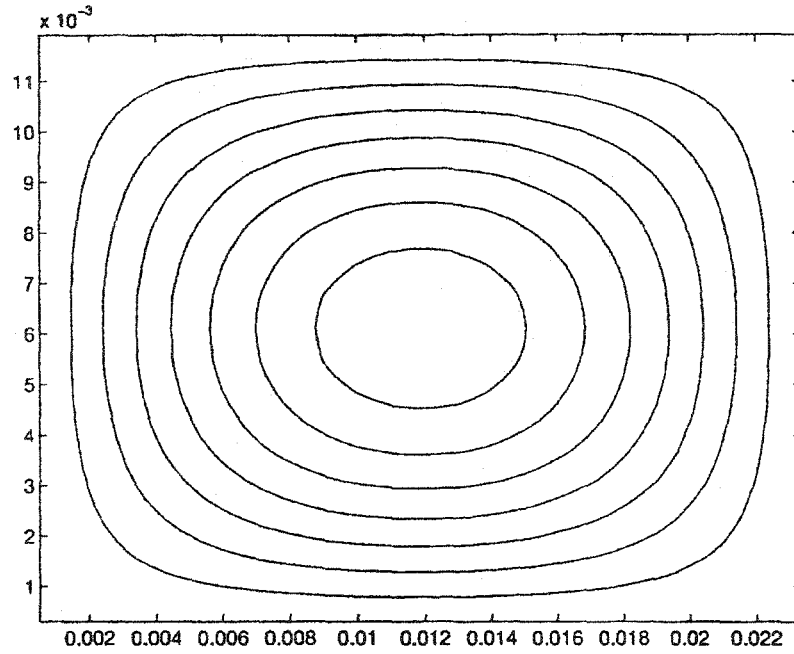


Figure 5.2: Contour lines of constant E_z field for TM_{11} mode, with waveguide cross section $2.286 \times 1.16 \text{ cm}^2$, and regular mesh of 50 cells in the x direction and 40 cells in y direction.

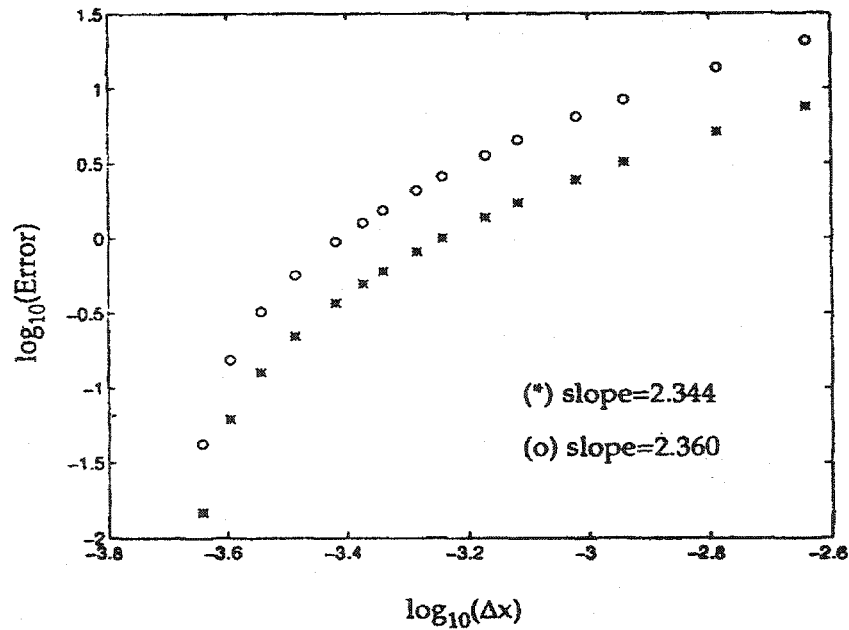


Figure 5.3 Logarithmic plot of error of TM_{11} mode using uniform mesh against the cell dimension. (o) maximum error, $\Delta x = \Delta x_{\max}$, (*) average error, $\Delta x = \Delta x_{\text{ave}}$.

Figure 5.4 gives an example of the non-uniform meshes that are used for the analysis of the waveguide problem. Uniform meshes are used on the left and right sides of the structure and a coarse mesh is used in the middle. The reason for a symmetrical mesh is to avoid the influence of excitation in the final field distribution. The cell ratio between contiguous regions is as small as 1.0526 and as large as 20. The maximum error versus maximum cell dimension, and average error versus average cell dimension, is plotted in Figure 5.5. For the maximum error case, the slope of the line was 2.221, and for the average error the slope was 16.079.

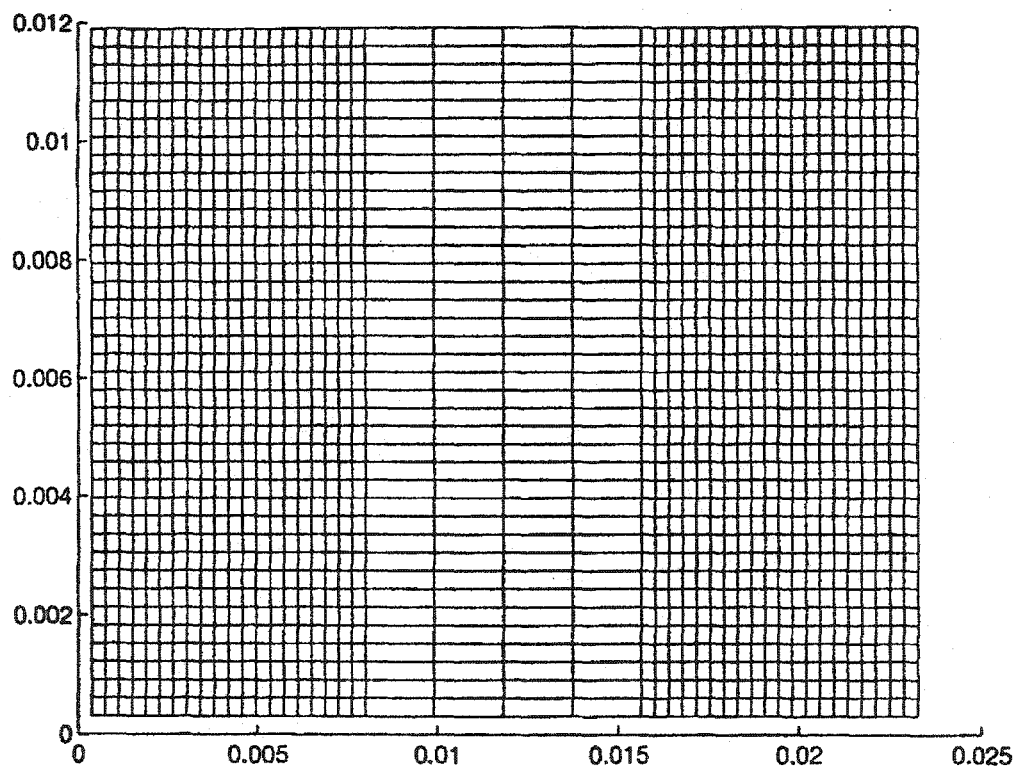


Figure 5.4: The cross section of the abrupt non-uniform mesh.

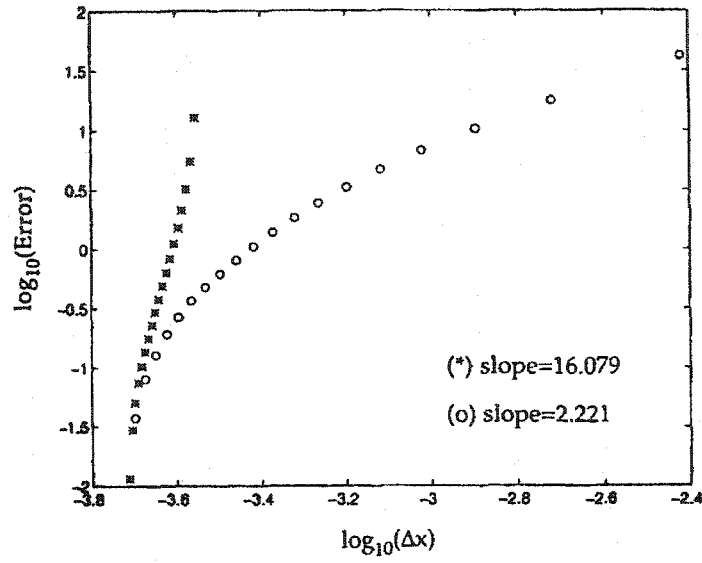


Figure 5.5: Logarithmic plot of error of TM_{11} mode using non-uniform with abrupt mesh against the cell dimension. (o) Maximum error, $\Delta x = \Delta x_{\max}$, (*) average error, $\Delta x = \Delta x_{ave}$.

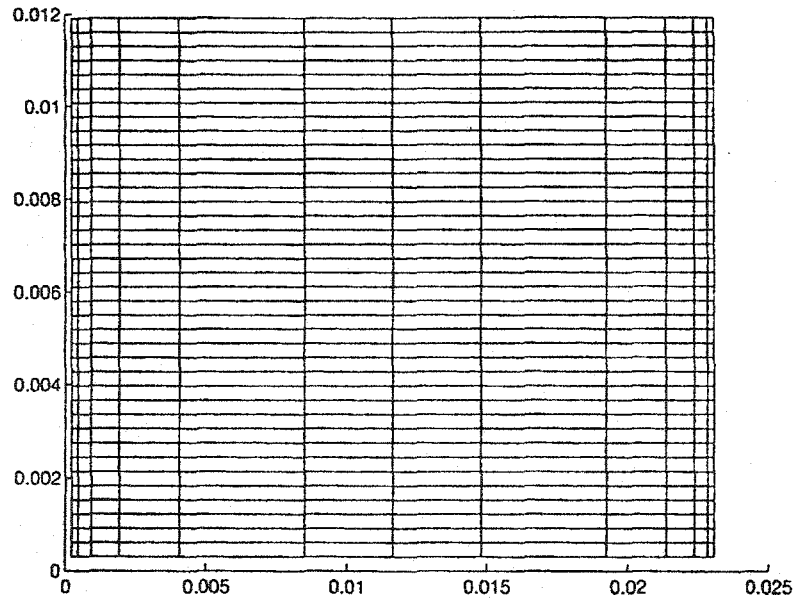


Figure 5.6: The cross section of gradual non-uniform mesh.

Figure 5.6 shows the effect of gradually changing non-uniform mesh, where symmetry is again imposed in order to avoid the influence of excitation. The ratio of change between adjacent cells varies from 1.1 to 2.5. Figure 5.7 is a log/log plot of error for a gradual non-uniform mesh against cell dimensions. Here the slope for the maximum error is 1.917, and that for the average error is 2.376.

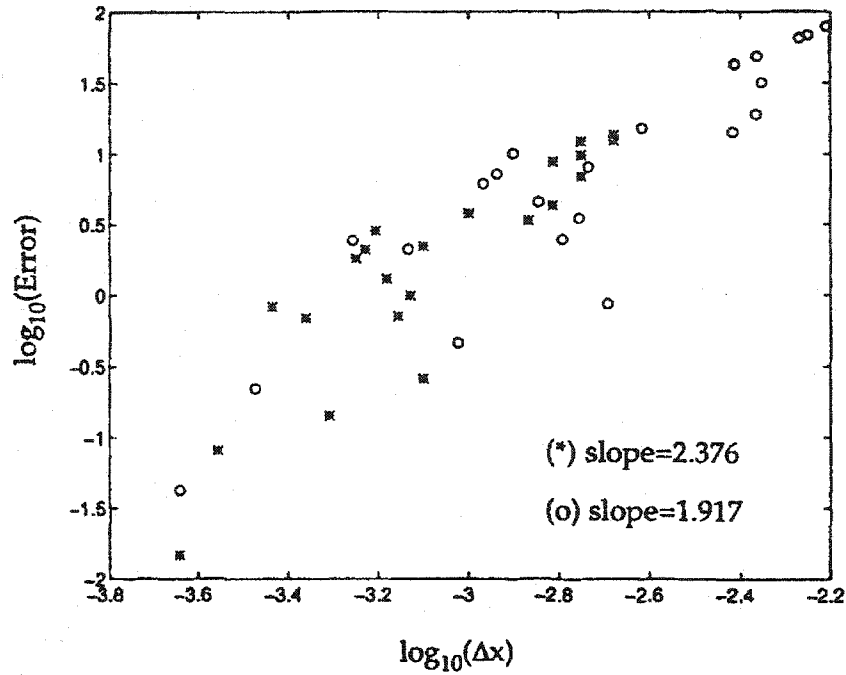


Figure 5.7: Logarithmic plot of error of TM₁₁ mode using gradual uniform mesh against the cell dimension. (o) Maximum error, $\Delta x = \Delta x_{\max}$, (*) average error, $\Delta x = \Delta x_{\text{ave}}$

5.2.2 Error Analysis with the Perfect Dispersive Boundary Conditions

The perfect Dispersive Boundary Condition (DBC) is an extension of the first order boundary condition. In a rectangular waveguide the dominant mode is the TE_{10} mode, and this can be explained as a combination of two plane waves travelling at angle γ with respect to the conducting walls. This angle is related to the frequency and the dimensions of the

waveguide, and so a first order perfect dispersive boundary condition can be developed to absorb the propagating monochromatic wave [2, 5]. The combination of the first order perfectly dispersive boundary conditions gives a second order one that exactly absorbs two monochromatic waves [2]. This absorbing boundary condition is similar to Litva's boundary condition that is used in the FDTD analysis of microstrip structures [6]. The first order perfectly dispersive boundary condition in a waveguide is applied to the tangential field components and can be written as

$$\left(\sqrt{1 - \left(\frac{1}{2af} \right)^2} \right) \frac{\partial U}{\partial t} - c \frac{\partial U}{\partial x} = 0 \quad (5.1)$$

where U is either E_y , or E_z , when it is applied in the x - y plane; a is the width of the rectangular waveguide; f is the frequency and c is the speed of light.

The perfectly dispersive boundary condition (DBC) in the waveguide can be made reasonably accurate, because the wave velocity is known for the dimensions of the waveguide at given frequency. In other words, since the angles of incidence of the plane waves with the boundaries are known [5], one can develop highly accurate boundary conditions. The simulation for the waveguide, with a monochromatic source of a TE_{10} field and with a perfect DBC located at the end of the waveguide, is discussed. A number of different grids are used, namely (1) uniform grids with different cell dimensions and (2) non-uniform grids along the axis of propagation with (a) two connected uniform regions with a change in dimension of ratio 1:9, and (b) a non-uniform mesh in which the size of the cell increases gradually. In the last case we adopt an exponential increase of the form $h_{i+1} = h_i$ times a constant factor, where the ratio $h_{max} : h_{min}$ is varied from 1 to 9. In both cases (1) and (2), a monochromatic source for a pure TE_{10} field and a perfectly dispersive boundary condition at the end cells were used. The discrete Fourier transform is applied at every electric field node point in the waveguide. Since the excitation source has the exact TE_{10}

field distribution, in an error free situation, one would expect the same field profile to propagate down the waveguide. However, in a non-ideal situation an error can be calculated from the difference between the expected and the simulated field profile. In Figure 5.8 maximum errors versus spatial increment are plotted for the cases (1), (2a) and (2b). In Figure 5.9 is plotted the average error versus average cell dimension. In each case, the least squares fit of the logarithm of the error result versus the logarithm of the cell dimension is calculated and shown in the insets of Figures 5.8 and 5.9. These results are illuminating and give a good insight into the errors that occur when the non-uniform mesh is used with a proper absorbing boundary condition. The results show that in spite of the mesh being non-uniform, second order accuracy is achieved. This conclusion remains true for meshes with many different types of non-uniformity. It is interesting to note that an exponentially varying grid gives a slope for the average error that is twice the slope of the uniform grid.

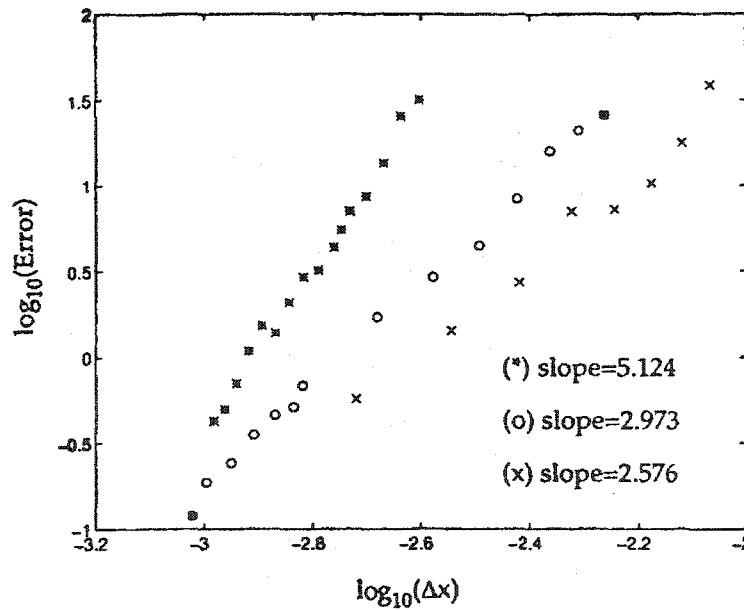


Figure 5.8: Average error versus average cell size using perfect dispersive boundary condition: (x) Uniform mesh, (o) Abrupt non-uniform mesh, (*) Gradual non-uniform mesh.

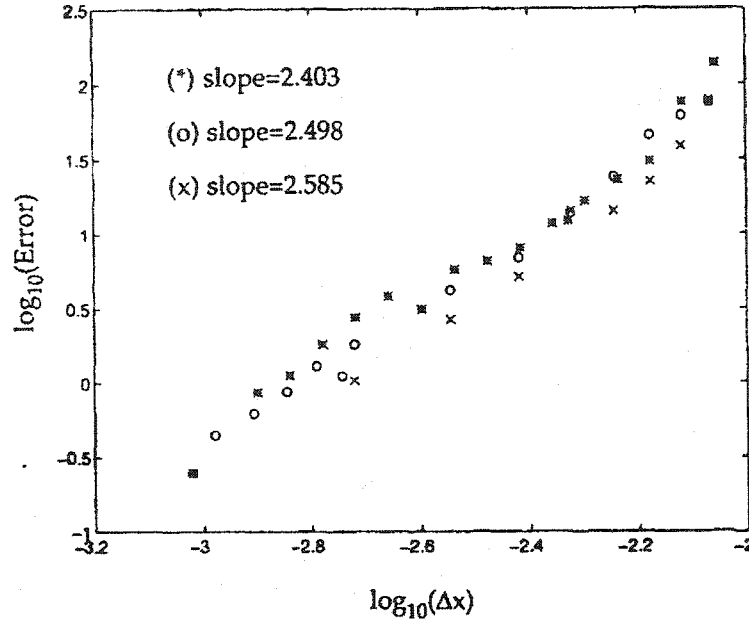


Figure 5.9: Maximum error versus maximum cell size using perfect dispersive boundary condition: (x) uniform mesh, (o) abrupt non-uniform mesh, (*) gradual non-uniform mesh.

5.2.3 Error Analysis with PML Absorbing Boundary Conditions

In this analysis a combination of exponentially increasing cell size with abrupt changes is used. A perfectly matched layer, described in Chapter 2, is used for the absorbing boundary, and a monochromatic source in TE_{10} mode is applied. The discrete Fourier transform is used at each nodal point. When implementing the PML boundary condition, the number of cells used in the absorbing layer along the x -direction was 40. Theoretically, the reflection for this PML is -100 dB, but in practice it turns out to be about -80 dB. In Figure 5.10, the maximum error versus spatial increment is plotted, and average error versus average cell dimension. The least square fit to the data in Figure 5.10 for maximum error versus maximum cell size gives a slope of 2.827, and for average error versus average cell size, the slope is 3.942.

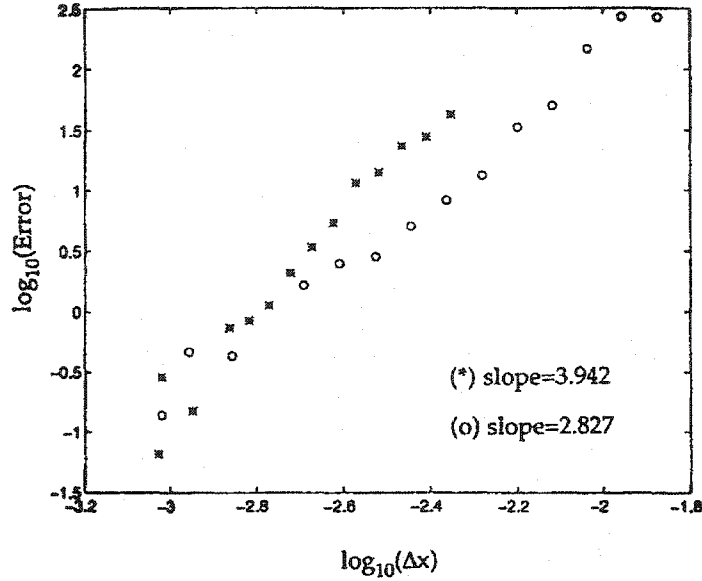


Figure 5.10: Error versus cell size using the PML ABC with abrupt non-uniform mesh: (o) Maximum error, $\Delta x = \Delta x_{\max}$, (*) Average error, $\Delta x = \Delta x_{\text{ave}}$

5.2.4 Error Analysis with Imperfectly Absorbing Boundary Conditions

In this case we apply the dispersive boundary condition to the waveguide problem, assuming that the two plane waves that propagate in the waveguide impinge on the boundary with normal incident (Mur's first order absorbing boundary [7]). This absorbing boundary condition is less than perfect, and the application of such an imperfect absorbing boundary condition gives a truncation error in the field calculation that is combined with the error due to the spatial discretization. The same mesh as in Section 4.2.3 is used for the present analysis along with the same TE_{10} source. The maximum error versus maximum cell dimension, and the average error versus average cell dimension, are shown in Figure 5.11. With such an imperfect absorbing boundary condition, the total error is found to degrade to first order accuracy. Based on the results given in Section 5.2.3, we conclude that this degradation is exclusively due to the truncation error in the imperfectly absorbing boundary conditions.

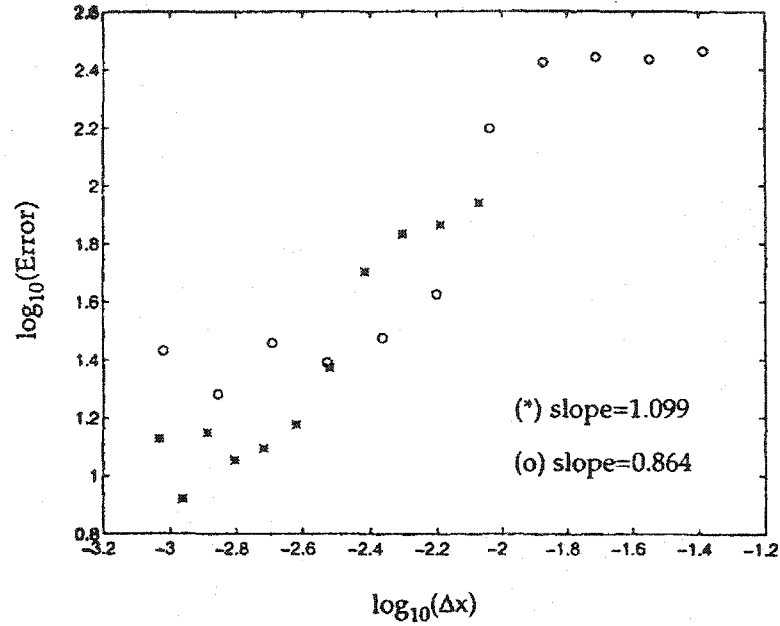


Figure 5.11 Error versus cell size using first order ABC with gradual and abrupt non-uniform mesh: (o) Maximum error, $\Delta x = \Delta x_{\max}$, (*) Average error, $\Delta x = \Delta x_{\text{ave}}$.

5.3 Summary

This chapter presents a detailed investigation of the non-uniform meshes in the FDTD method. In particular, we observed the errors generated by non-uniform meshes and concluded that they are of second-order with respect to the cell size. This numerical analysis was based on the assumption that "exact" boundary conditions were used to terminate the far end of the waveguide. The PML technique was adapted for use with the non-uniform FDTD method and it behaves like an "exact" boundary condition. We showed that the accuracy of the non-uniform FDTD method degrades to first order if less than exact boundary conditions

are used. We have demonstrated the accuracy of the calculations based on non-uniform meshes using wave propagation in waveguides [9].

5.5 References

- [1] A. Taflove and K. R. Umashankar, "Review of FD-TD numerical modelling of electromagnetic wave scattering and radar cross section," *Proc. IEEE*, vol. 47, pp. 421-435, 1986.
- [2] E. A. Navarro, L. Gallart, J. Cruz, B. Gimeno, and V. Such, "Accurate absorbing boundary conditions for FDTD analysis of H -plane waveguide discontinuities," *IEE Proc. Microwave Antennas and Propagation*, vol. 141, pp. 59-61, 1994.
- [3] J. Berenger, "A perfectly matched layer for the absorption of electromagnetic waves," *J. Computational Physics*, vol. 114, pp. 185-200, 1994.
- [4] D. S. katz, E. T. Thiele, and A. Taflove, "Validation and extension to three dimensions of the Berenger PML absorbing boundary condition for FD-TD meshes," *IEEE Trans. Microwave Guided Wave Lett.*, Pp. 268-270, Aug. 1994.
- [5] J. G. Blaschak and G. A. Kriegsmann, "A comparative study of absorbing boundary conditions," *J. Comput. Phy.*, vol. 77, pp. 109-139, 1988.
- [6] Z. Bi, K. L. Wu, C. Wu and J. Litva, "A dispersive boundary condition for microstrip component analysis using FD-TD method," *IEEE Trans. Microwave Theory Tech.*, vol. MTT-40, pp. 774-777, 1992.
- [7] E. A Navarro and V. Such, "Study of TE and TM modes in waveguides of arbitrary cross-section using a FD-TD formulation," *IEE Proc. Microwave Antennas and Propagation*, vol. 139, pp. 491-494, 1992.

- [8] G. Mur, "Absorbing boundary conditions for the finite-difference approximation of the time domain electromagnetic field equations," *IEEE Trans. Electromagnetic Compat.*, vol. EMC-23, pp. 377-382, 1981.
- [9] E.A. Navarro, N.T. Sangary and J. Litva, "Non-uniform FDTD Method and Its Application to Waveguide Analysis When Combined with the Perfectly Matched Layer Technique," *IEEE Transactions on Microwave Theory and Techniques*, vol.44, pp. 1115-1124, July 1996.

Chapter 6

Microwave Device Analysis with FDTD Method

6.0 Introduction

Over the last decade, the analysis of microwave devices using electromagnetic simulators has become very popular [1-3]. The existence of numerous commercial electromagnetic simulators, such as the Agilent Momentum and ADS, Ansoft HFSS, IE3D, and H-Spice, shows that electromagnetic simulation tools are essential for microwave circuit design. Not all these simulators integrate the lumped element and device equations with the EM field directly. In these simulators, each device is a separate entity in the circuit. The individual devices are characterised by their scattering parameters, and then they are combined to form the scattering parameters of the entire circuit using the ABCD matrix approach. In this method of calculating the scattering parameters of the entire circuit, the interactions between individual devices are neglected. In addition, these simulators do not accurately represent the physical structure of the device. Thus, the above-mentioned commercial simulators are not suitable for analysing high frequency integrated circuits where the interactions between the devices and the surrounding physical structures play a vital role. Furthermore, in these simulators, there are theoretical limits in the accuracy when applied to three-dimensional structures, and these limits are specific to the techniques used in EM simulators such as the Method of Moments, and the Finite Element Method.

Even though the existing circuit simulators are going through refinements, the theoretical limitation and the inadequate level of integration in these simulators give the FDTD technique an added advantage. With the increase of CPU speed and the cost reduction of modern day computers, the FDTD technique is becoming increasingly attractive. This chapter contains the necessary basics for the application of the FDTD method to device simulations, and it presents some improvements to the technique.

The circuit models of most microwave devices include only the basic components such as resistors, capacitors, inductors, diodes, voltage dependent sources, and current dependent sources. Therefore, we begin our discussion with the integration into the FDTD algorithm of some of these simple components. In addition, a unique method for implementing the device current is introduced; this handles simulation at higher frequencies with improved accuracy.

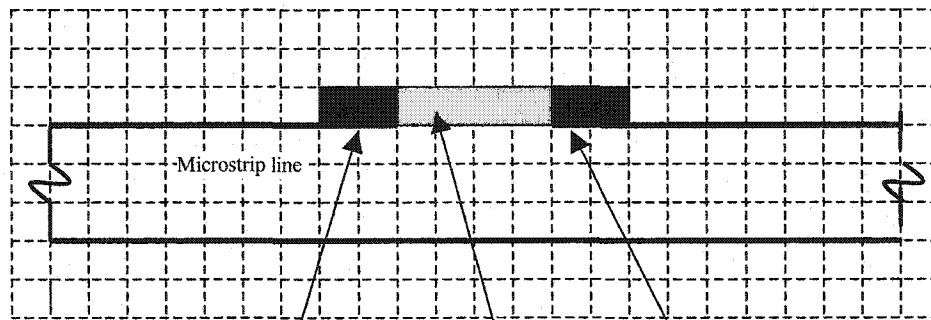
6.1 Implementation of Device Current and Voltage

The implementation of microwave devices in the FDTD algorithm requires accurate representation of the physical structure of the device. The simple application of the device equation at a single point in space as given in [1] is not sufficient. In microwave integrated circuits, some of the packaged devices will be large compared to the FDTD cell size. Therefore, one cannot accurately represent the physical structure of a packaged device with only a single cell. By increasing the cell size one could match the physical size of the device. However, this results in inaccurate EM analysis. The following example elaborates on this statement.

Consider a typical case where we are interested in the simulation in the range of 10 GHz on a substrate of relative dielectric constant 4.0. The wavelength in the substrate is 15 mm. In order to get an accurate simulation, the maximum cell size should be less than one tenth of the wavelength, which is 1.5 mm. However, if we were to use a good tolerance (less than $\pm 5\%$) capacitor of higher values ($>1 \mu\text{F}$) in the circuit, then the size of the capacitor is

3.2 mm by 2.5 mm by 1.5 mm. Under this condition, we need at least four cells to model the capacitor and thus the model proposed in [1] is inadequate. In order to improve the simulation accuracy, the volume occupied by the device should reflect the exact material characteristics used in the device package. This further emphasises the need for more than one cell, and appropriate device equations. A simple model for the device could be a conductive cell for the contact points and a dielectric block for the package. Figure 6.1 shows a typical representation of a device package.

Side view



Contact points

Device package

Contact points

Top view

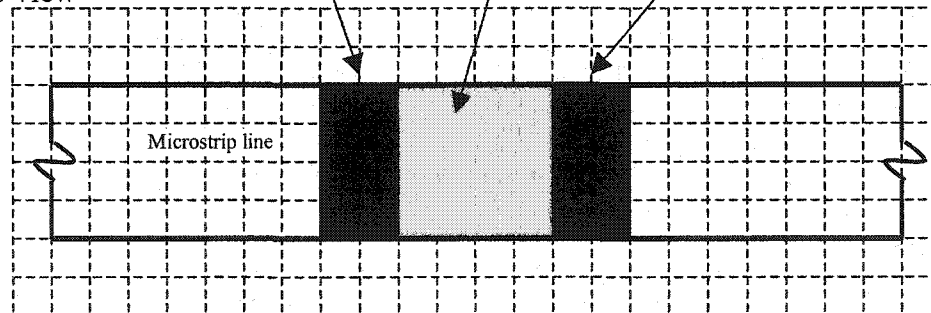


Figure 6.1: Typical device configuration in FDTD simulation

An important aspect in the implementation of device equations in the FDTD technique is the stability of the algorithm. Stability is easily achievable if the modifications to the fields in the standard FDTD algorithm are minimal, that is if the device equation modifies only one field component. This type of implementation is observed in [1], where the device equation is used for modifying only the x component of the E -field at the point in space where the device resides. In this implementation, the FDTD algorithm incorporates the device equation as an additional source, which does not change the rest of the structure. We carry out a similar implementation in our scheme, except that more than one source point is used.

6.2 Formalism of Current and Voltage in the FDTD Method

The formulation of active and passive devices in the FDTD method was initially reported in [4], while an extensive development is given in [1]. In this formulation, the modification to the standard FDTD algorithm is the inclusion of the conduction current in addition to the displacement current of the magnetic curl equation of Maxwell's equation. The conduction current is the device current and it becomes an excitation source in the computational domain of the electromagnetic field. Therefore, at these excitation points, the Maxwell's equations used in the FDTD algorithm need modification to include the device current I_D , whose mathematical form is

$$\varepsilon \frac{\partial \vec{E}}{\partial t} = (\nabla \times \vec{H}) - \vec{J} \quad (6.1)$$

where the device current I_D will satisfy

$$I_D = \int_s \vec{J} \cdot \hat{n} \, ds \quad (6.2)$$

In the FDTD algorithm, due to the nature of the leapfrog scheme, the locations of the electric and magnetic field components are at different points in space and time. Since the device current is included in the FDTD algorithm via equation (6.1), in space, the device current has to be calculated at either one of the field points; for which the most convenient location is that of the electric field. This is because the calculation of the device current is carried out with the knowledge of the device voltage at specific instants of time. In the FDTD scheme, the current density is obtained at the same time-step as the magnetic field. This is expressed clearly in the discretized form of (6.1):

$$E^{n+1} = \left[E^n + \frac{\Delta t}{\varepsilon} \nabla \times H^{n+\frac{1}{2}} \right] - \frac{\Delta t}{\varepsilon} J^{n+\frac{1}{2}} \quad (6.3)$$

The derivation is carried out for one component. They can be easily extended to any other two components. By fixing the orientation for the device, e.g., if the current through the device is along the x -direction, the current density is expressed as

$$J_x = \frac{I_{Dx}}{\Delta y \Delta z} \quad (6.4)$$

The substitution of (6.4) into (6.3) results in

$$E_x(i, j, k)^{n+1} = E_x(i, j, k)^n + \frac{\Delta t}{\varepsilon} \left[\frac{H_z^{n+\frac{1}{2}}(i, j, k) - H_z^{n+\frac{1}{2}}(i, j-1, k)}{\Delta y} - \frac{H_y^{n+\frac{1}{2}}(i, j, k) - H_y^{n+\frac{1}{2}}(i, j, k-1)}{\Delta z} \right] - \frac{\Delta t}{\varepsilon \Delta z \Delta y} I_{Dx}^{n+\frac{1}{2}} \quad (6.5)$$

In all device equations, the current through the device is a function of the voltage across the device at the same time instant. However, in the field equation, the definition of the current is at time steps $n+1/2$, and therefore the voltage, which results from the electric

field, should be defined or calculated for time steps $n+1/2$. To complicate matters further, the electric field at time step $n+1/2$ is unknown, and one needs to calculate it from the electric field at time steps n and $n+1$. The expression of the electric field at $n+1/2$ depends on the device current as a function of time, and this requires the solution to the individual device equation.

In the FDTD algorithm at time step $n+1$, the value of electric field at time step n and the value of magnetic fields at time step $n+1/2$ are known. The only unknown is the electric field at time step $n+1$. By setting X as:

$$X = E_x(i, j, k)^n + \frac{\Delta t}{\epsilon} \left[\frac{H_z^{n+1/2}(i, j, k) - H_z^{n+1/2}(i, j-1, k)}{\Delta y} - \frac{H_y^{n+1/2}(i, j, k) - H_y^{n+1/2}(i, j, k-1)}{\Delta z} \right] \quad (6.6)$$

equation (6.5) can be rewritten as

$$E_x^{n+1}(i, j, k) = X - \frac{\Delta t}{\epsilon \Delta z \Delta y} I_{Dx}^{n+1/2} \quad (6.7)$$

In implementing equation (6.7) in the FDTD algorithm, the only unknown is E_x^{n+1} . If the device current $I_{Dx}^{n+1/2}$ is split into two in the time domain as I_{Dx}^{n+1} and I_{Dx}^n , with these currents coinciding to the electric field with E_x^{n+1} and E_x^n , then (6.7) can be written as:

$$E_x^{n+1}(i, j, k) + \frac{\Delta t}{\epsilon \Delta z \Delta y} I_{Dx}^{n+1} = X - \frac{\Delta t}{\epsilon \Delta z \Delta y} I_{Dx}^n \quad (6.8)$$

In (6.8), E_x^{n+1} depends on I_{Dx}^{n+1} , which is a function of E_x^{n+1} only, and it in turn depends on the device equation. In some cases, this may lead to transcendental equations.

Figure 6.2 shows, the block diagram for the implementation steps of the FDTD algorithm.

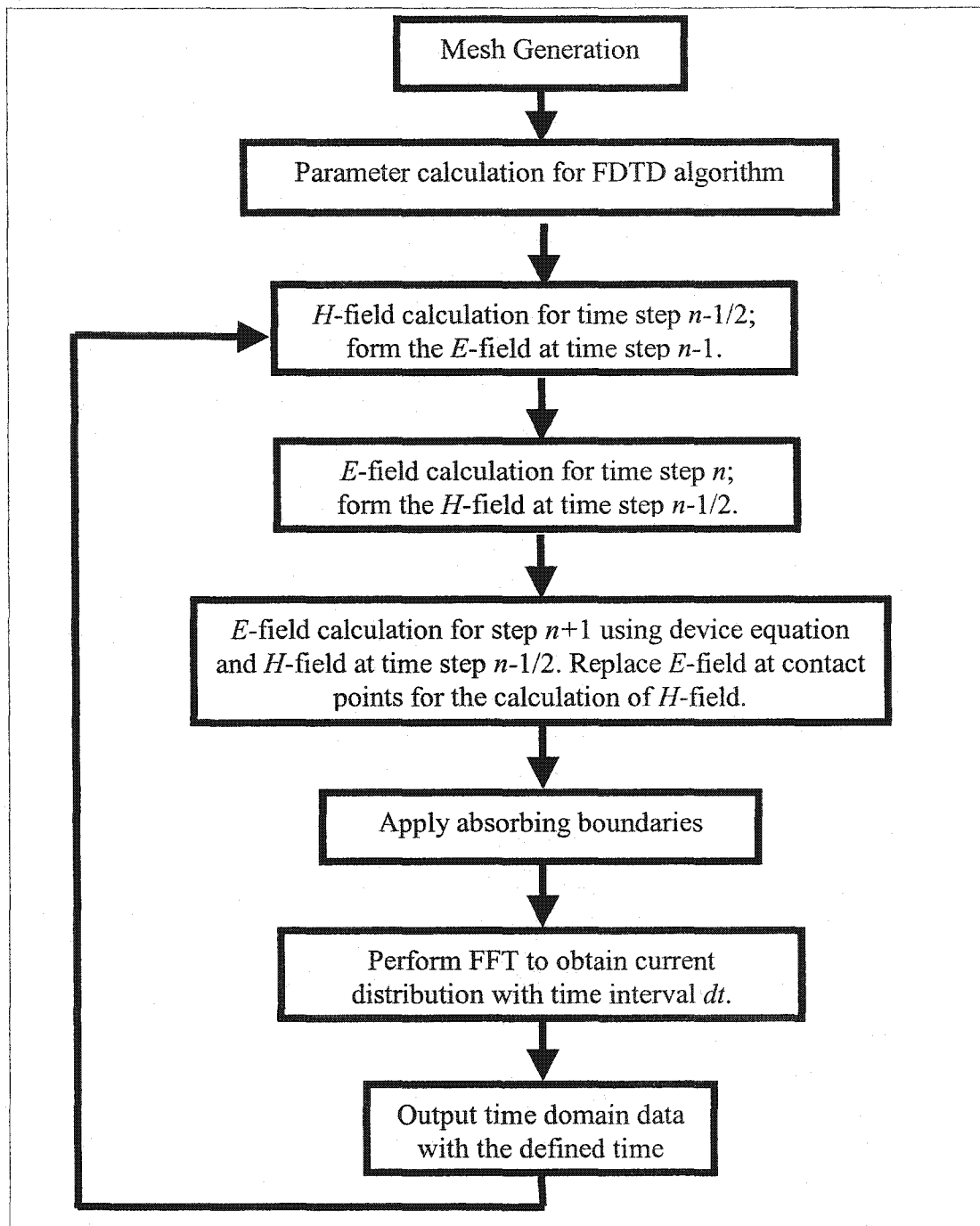


Figure 6.2: Block diagram for device equation in the FDTD algorithm.

6.2.1 Resistor

The device equation for the resistor that has to be integrated with the field equation is

$$I = \frac{V}{R} \quad (6.9)$$

In order to incorporate this device equation into FDTD algorithm, the device current should be defined at time step $(n+1)$. The expression for the current in discrete form is:

$$I_{Dx}^{n+\frac{1}{2}} = \frac{\Delta x E_x^{n+\frac{1}{2}}}{R} \quad (6.10)$$

For a resistor, since there is no time dependence in the device equation, the following approximation is made.

$$E_x^{n+\frac{1}{2}} = \frac{E_x^{n+1} + E_x^n}{2} \quad (6.11)$$

By defining the current at a given time step, we could write the current in the following form.

$$I_{Dx} = I_{n+1} + I_n \quad (6.12)$$

where the current at a given time step is given by

$$I_{n+1} = \frac{\Delta x E_x^{n+1}}{2R}, \quad I_n = \frac{\Delta x E_x^n}{2R} \quad (6.13)$$

With equations (6.12) and (6.13), for a resistor equation (6.8) can be written as

$$E_x^{n+1} = \frac{X - \frac{\Delta t}{\varepsilon \Delta z \Delta y} I_n}{1 + \frac{\Delta x \Delta t}{2 \varepsilon \Delta z \Delta y R}} \quad (6.14)$$

The FDTD algorithm will incorporate equation (6.14).

6.2.2 Capacitor

For a capacitor, the device equation is as follows.

$$I_c = C \frac{dV}{dt}, \quad (6.15)$$

The current at time step $(n+1/2)$ can be written as:

$$I_{Dx}^{n+\frac{1}{2}} = C \frac{\Delta x}{\Delta t} [E_x^{n+1} - E_x^n] \quad (6.16)$$

In addition, the current at a given time step is defined as

$$I_{n+1} = C \frac{\Delta x}{\Delta t} E_x^{n+1}, \quad I_n = -C \frac{\Delta x}{\Delta t} E_x^n \quad (6.17)$$

Using equations (6.16) and (6.17), for a capacitor equation (6.8) can be written as

$$E_x^{n+1} = \frac{X + \frac{C \Delta x}{\varepsilon \Delta y \Delta z} E_x^n}{1 + \frac{C \Delta x}{\varepsilon \Delta y \Delta z}}. \quad (6.18)$$

6.2.3 Inductor

The device equation for an inductor is:

$$I_L = \frac{1}{L} \int_0^t V dt \quad (6.19)$$

The current at time step $(n+1/2)$ can be written in the following manner.

$$I_{Dx}^{n+\frac{1}{2}} = \frac{\Delta x \Delta t}{2L} \left[\frac{1}{2} E_x^{n+1} + \sum_0^n E_x^n \right] \quad (6.20)$$

and the current at a given time step is defined as

$$I_{Dx}^n = \frac{\Delta x \Delta t}{2L} \sum_0^n E_x^n, \quad I_{Dx}^{n+1} = -\frac{\Delta x \Delta t}{4L} E_x^{n+1}, \quad (6.21)$$

With equations (6.21) and for an inductor, equation (6.8) becomes:

$$E_x^{n+1} = \frac{X - \frac{\Delta x (\Delta t)^2}{2L \varepsilon \Delta y \Delta z} \sum_0^n E_x^n}{1 - \frac{\Delta x (\Delta t)^2}{4L \varepsilon \Delta y \Delta z}}. \quad (6.22)$$

6.2.4 Diode

For a diode, the device equation is as follows:

$$I_d = I_0 \left[\exp \left(\frac{qV_d}{kT} \right) - 1 \right] \quad (6.23)$$

where the current at time step $(n+1/2)$ can be written as

$$I_{Dx}^{n+\frac{1}{2}} = I_0 \left[\exp \left(\frac{q \Delta x E_x^{n+1} + q \Delta x E_x^n}{2kT} \right) - 1 \right] \quad (6.24)$$

By defining the current at a given time step as:

$$I_{Dx}^{n+1} = I_{Dx}^n \exp \left(\frac{q \Delta x E_x^{n+1}}{2kT} \right) - I_0 \quad (6.25)$$

and

$$I_{Dx}^n = I_0 \exp\left(\frac{q\Delta x E_x^n}{2kT}\right), \quad (6.26)$$

the expression for the electric field at time $n+1$ can be written as

$$E_x^{n+1} + \frac{\Delta t}{\epsilon \Delta y \Delta z} I_{Dx}^{n+1} = X \quad (6.27)$$

Using Newton-Raphson, the solution to the above equation is

$$E_x^{n+1} = E_x^n - \frac{E_x^n - X + \frac{\Delta t}{\epsilon \Delta y \Delta z} [I_0 \exp(\frac{q\Delta x E_x^n}{kT}) - I_0]}{1 + \frac{q\Delta x}{2kT} \frac{\Delta t}{\epsilon \Delta y \Delta z} I_0 \exp(\frac{q\Delta x E_x^n}{kT})} \quad (6.28)$$

In deriving this expression, the initial approximate value for the root was E_x^n .

6.2.1 Voltage/Current Sources

The device equation for a voltage source V_s with series resistance R is as follows.

$$V = IR - V_s \quad (6.29)$$

In the FDTD notation (6.29) becomes:

$$I_{Dx}^{n+\frac{1}{2}} = \frac{\Delta x (E_x^{n+1} + E_x^n) - 2V_s^n}{2R} \quad (6.30)$$

where V_s^n is the voltage source defined at time step n . The voltage source could be a dependent source, which can be obtained from the field value at the desired point in space:

$$E_x^{n+1}(i, j, k) = \frac{X - \frac{\Delta t}{2R\epsilon \Delta z \Delta y} (\Delta x E_x^n(i, j, k) - 2V_s^n)}{\left(1 + \frac{\Delta t \Delta x}{2R\epsilon \Delta z \Delta y}\right)} \quad (6.31)$$

A similar expression can be obtained for a current source with shunt conductance G and current source I_s^n , as in equation (6.32).

$$E_x^{n+1}(i, j, k) = \frac{X - \frac{G\Delta t}{2\epsilon \Delta z \Delta y} (\Delta x E_x^n(i, j, k) - 2I_s^n)}{\left(1 + \frac{G\Delta t \Delta x}{2\epsilon \Delta z \Delta y}\right)} \quad (6.32)$$

The construction of models for active devices such as a bipolar junction transistor and field effect transistors, can utilize the equations (6.31) and (6.32).

6.2.4 Transistor

A bipolar junction transistor can be modelled with two diodes and two dependent current sources. The section above includes the required derivation for the individual components. Similar detailed derivations of device equations for transistors are given in [4].

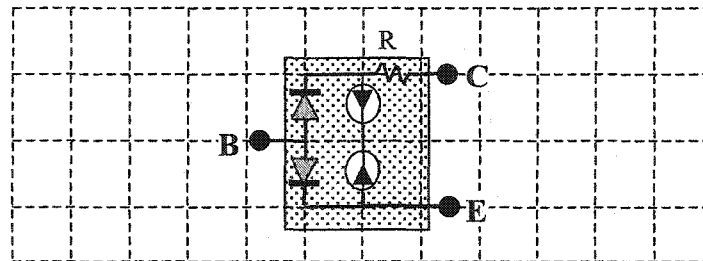


Figure 6.3: A simple model for transistor

In the above model, four cells represent a transistor. Similar models can be built for other active devices.

6.3 Simulation of Microwave Devices

Almost every practical problem with integrated circuits involves devices placed in two-dimensional space. In this section, we demonstrate a very simple form of such a circuit. The Figure 6.4 shows this circuit and in it, we have used coaxial ends to connect the microstrip lines, which connect the device under test.

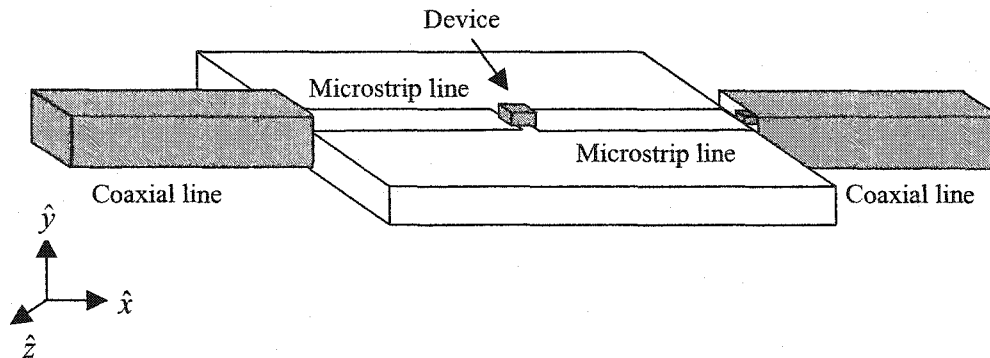


Figure 6.4: A simple structure for device simulation

The substrate used for the microstrip line has relative dielectric constant of 4.00, the substrate height is 1.8 mm, and the other dimensions are given in Figure 6.5. This figure shows the plane containing the device and the mesh used in the simulation. The devices for the simulation are capacitors of different values, an inductor, and a diode to demonstrate the non-linear effect in FDTD simulation.

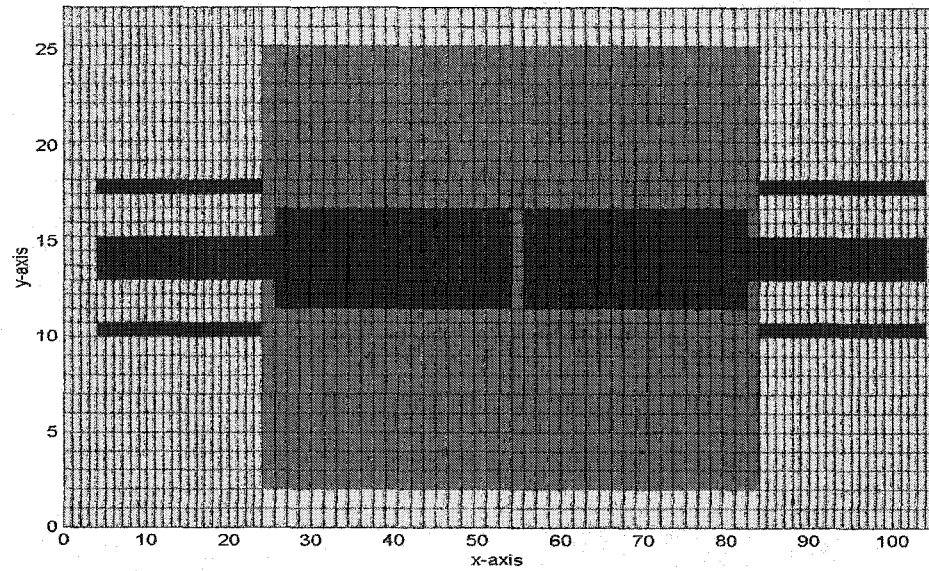


Figure 6.5: The planar view of device and the mesh.

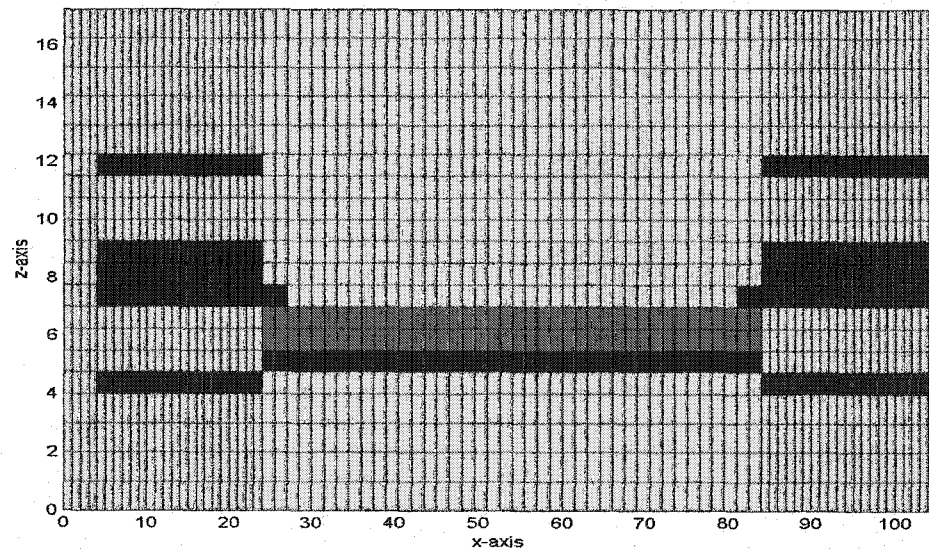


Figure 6.6: The side view of device and the mesh.

It is shown in Figures 6.5 and 6.6 that the mesh used is non-uniform. The use of non-uniform mesh is to observe the effects of non-uniform mesh in the overall simulation. In the simulation, we used capacitor values of 100 pF and 2 pF. Figures 6.7 to 6.10 show the simulation and measurement results. The simulation is with a board size of 100 mm by 50 mm by 2 mm, which is enclosed in a volume of size of 100mm by 50mm by 30mm with mesh size of 85 by 30 by 20. The pulse width of the excitation source was 20ps and the pulse duration was 200ps. The sampling points for S_{11} and S_{12} are 10 cells from the respective ends of the coaxial line. In the simulation, the device is characterised using one cell, and the device equation was constructed using two edges of the cells on the device plane. The simulation was carried out with real-valued terms representing the field's components, thus any dielectric loss is ignored.

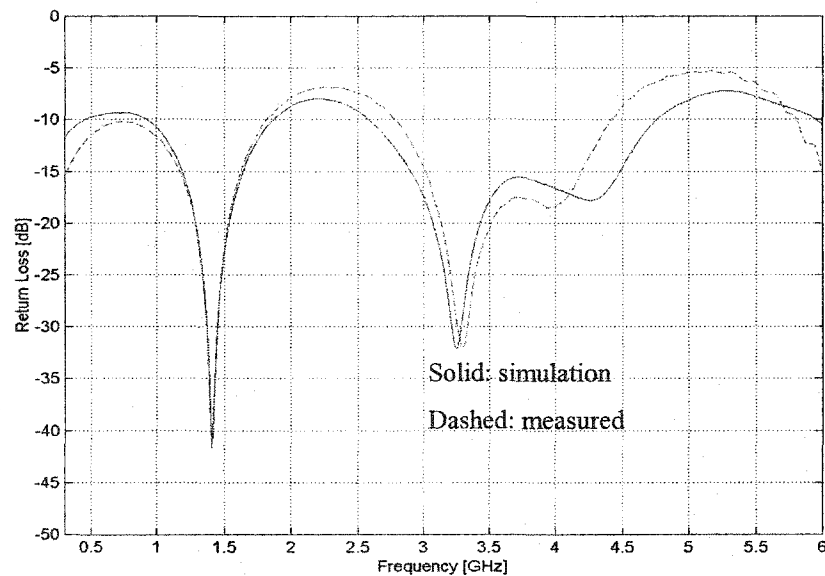


Figure 6.7: Return loss for capacitor of value 100 pF

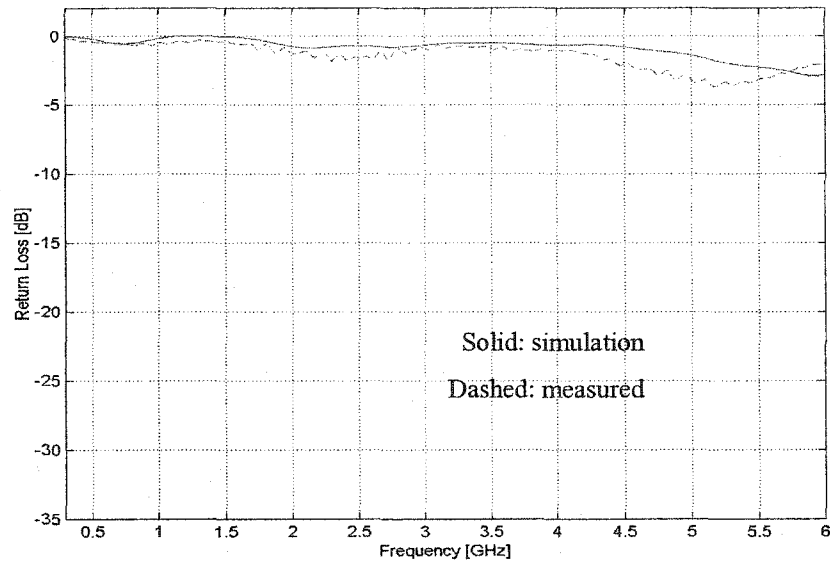


Figure 6.8: Insertion loss for the 100 pF capacitor.

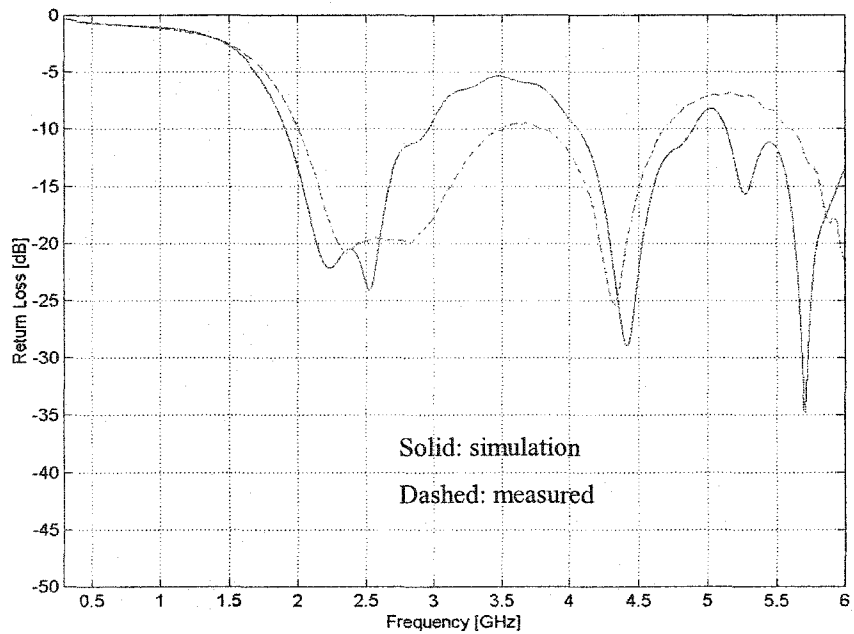


Figure 6.9: Return loss for the 2 pF capacitor.

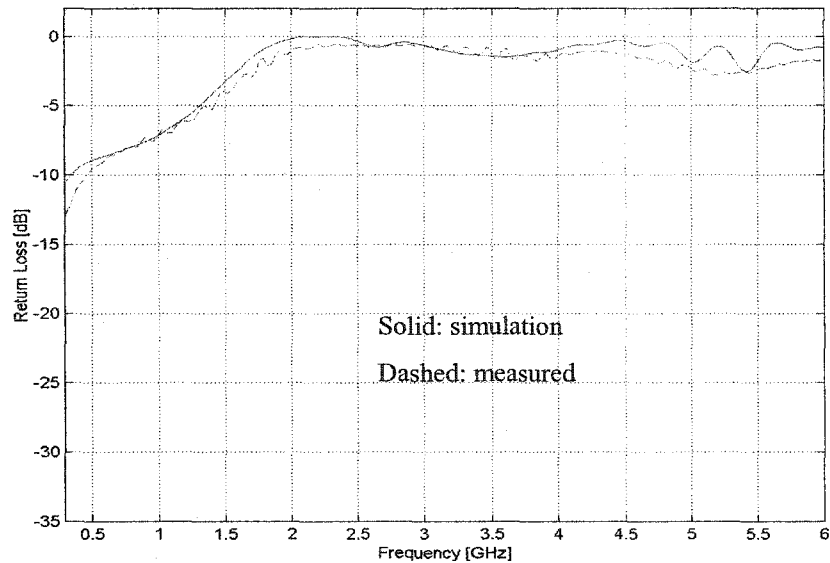


Figure 6.10: Insertion loss for the 2pF capacitor.

The simulation and measurements is repeated with a 10nH inductor. The Figures 6.11 and 6.12 show the results. These results show a greater discrepancy than those with the capacitor. This is attributed to the use of a component of lower tolerance. This means that the component values specified by the manufacture have larger percentage error. Since these component values are used in the device equations, the overall error in the simulation is expected to be higher.

A similar simulation was carried out with a diode. The results are shown in Figure 6.13. In this simulation, a sinusoidal excitation source of frequency 1GHz and amplitude 10V is used. In addition, a simulation was carried out to show the effect of non-linearity of the diode, in that two sinusoidal sources of frequencies 1 GHz and 4GHz were used and both signals were of amplitude 10V. The result of this simulation is shown in Figure 6.14. In the plots, the dashed line is the spectral domain representation of the input signals, and the solid line is the sampled signal at the output terminal.

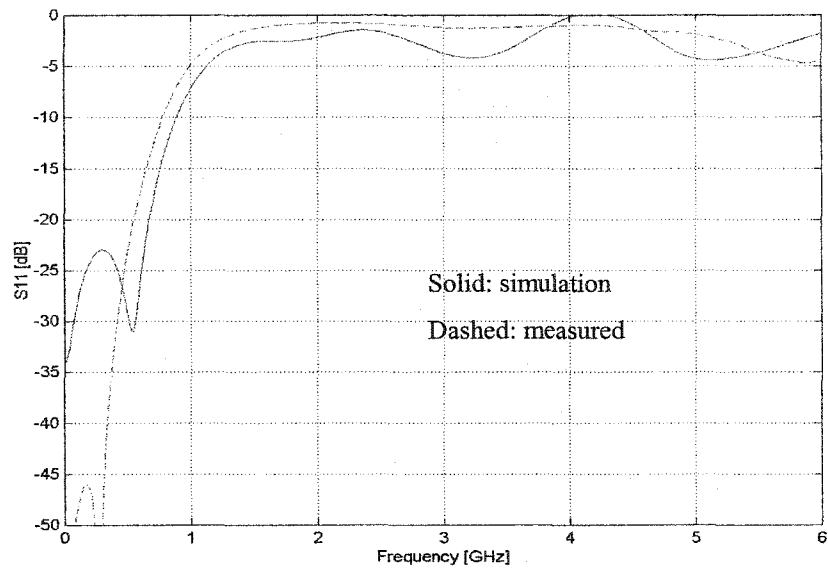


Figure 6.11: Return loss of 10nH inductor.

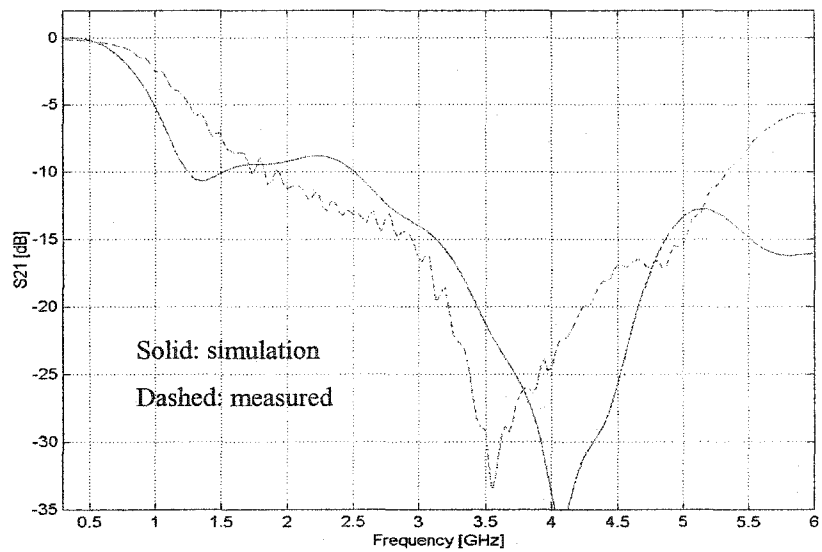


Figure 6.12: Insertion loss of 10nH inductor.

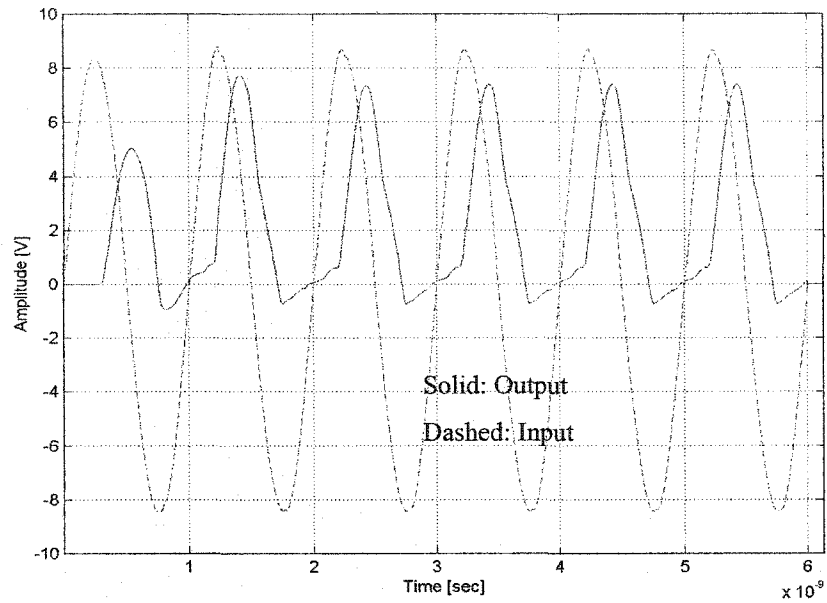


Figure 6.13: Time domain response of a diode.

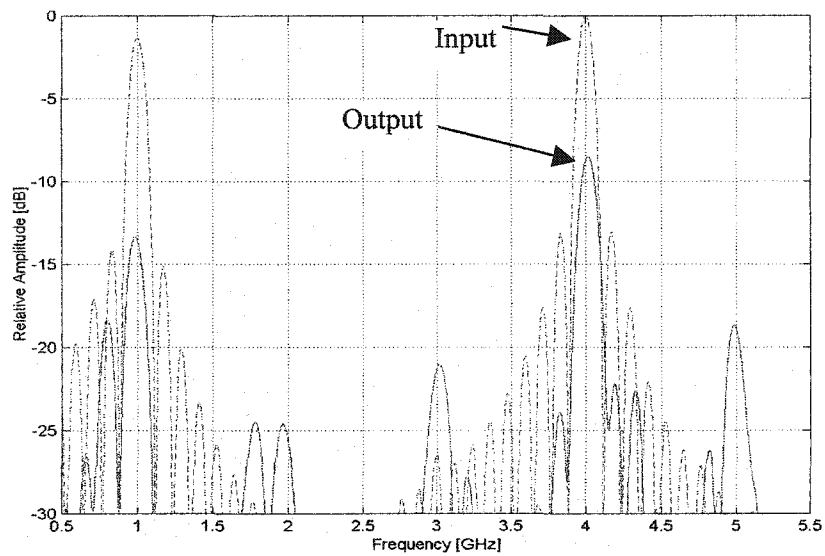


Figure 6.14: Spectral domain response of a diode.

All simulations are carried out using the programs developed by the author. The main program is written in the language C++, and the interface is written in MATLAB®. The Figure 6.15 shows the shell of the interface program, and the Figures 6.16 and 6.17 show the three-dimensional views of a typical structure. As an example, the current distribution in different planes for the case of a 2 pF capacitor on a microstrip transmission line are shown in Figures 6.18 through 6.25. Detailed instruction on the use of the simulation package can be found in the manual [5].

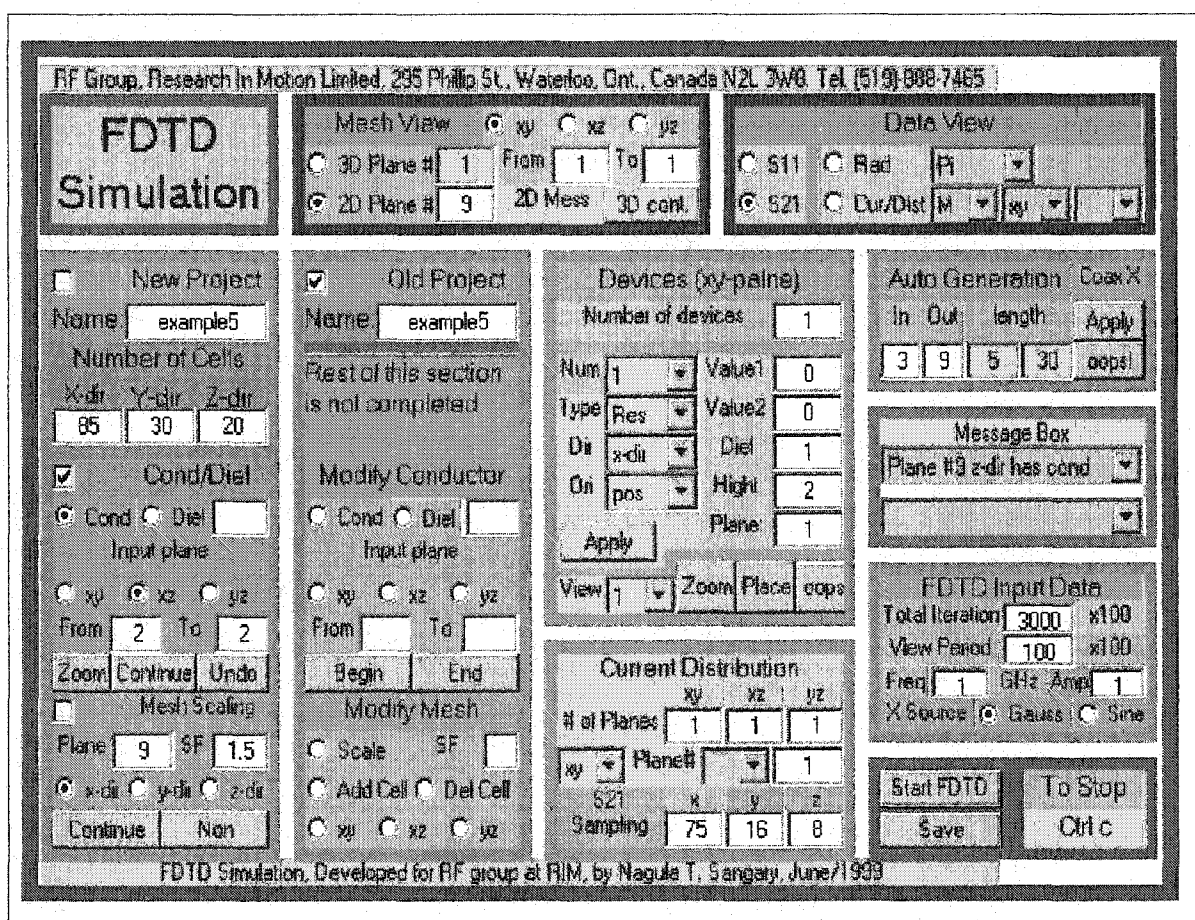


Figure 6.15: The interface program shell.

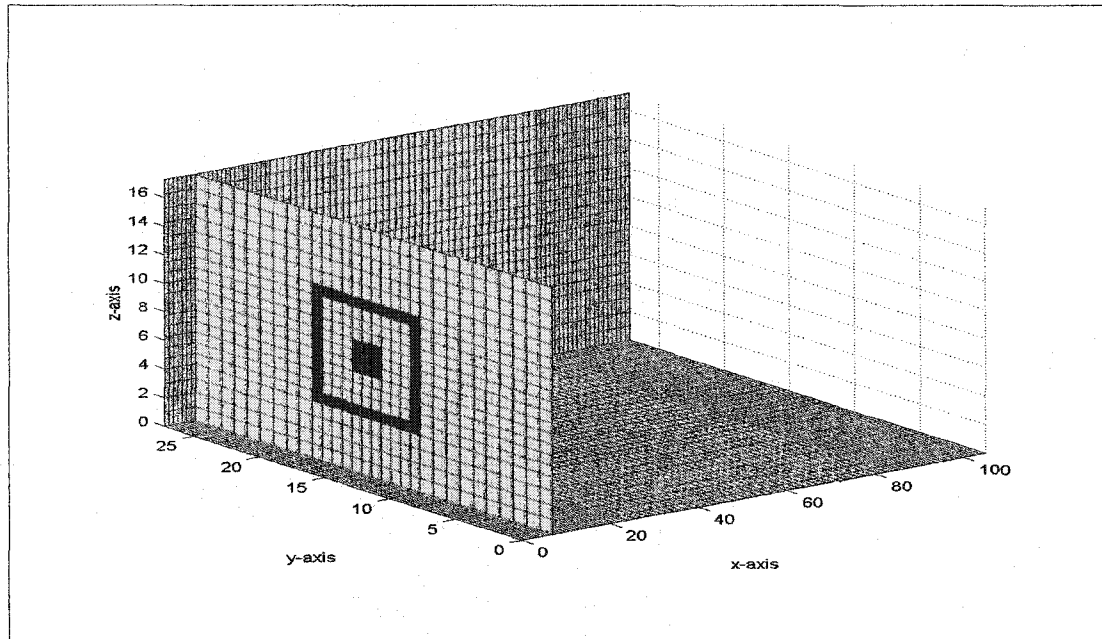


Figure 6.16: Three-dimensional view of the mesh with yz plane cut.

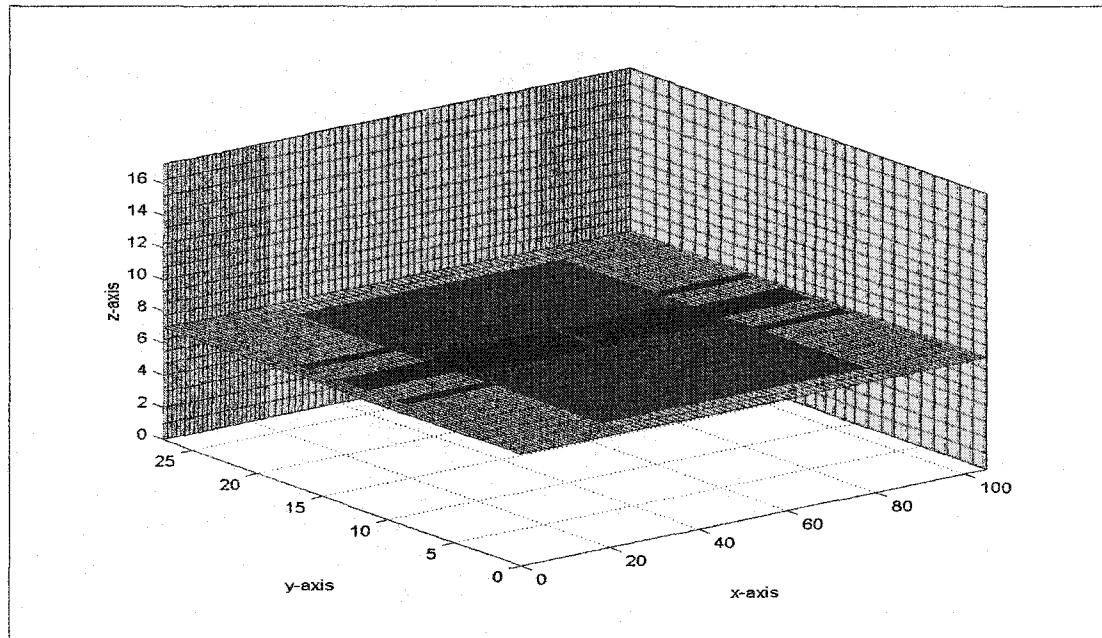


Figure 6.17: Three-dimensional view of the mesh with xy plane cut.

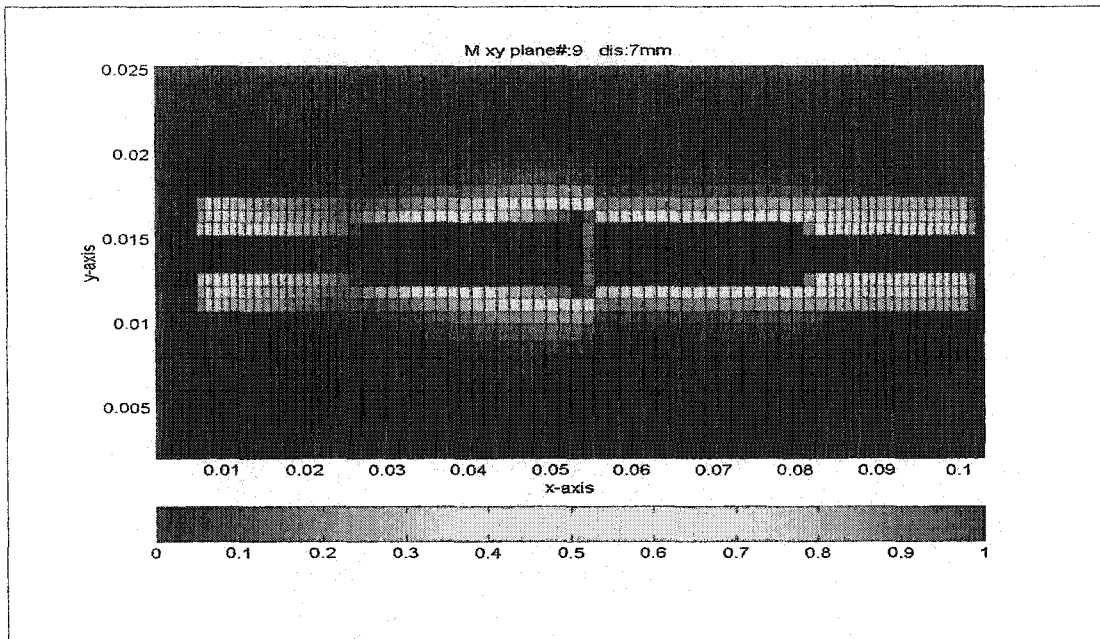


Figure 6.18: Electric current distribution on xy plane for capacitor (2 pF).

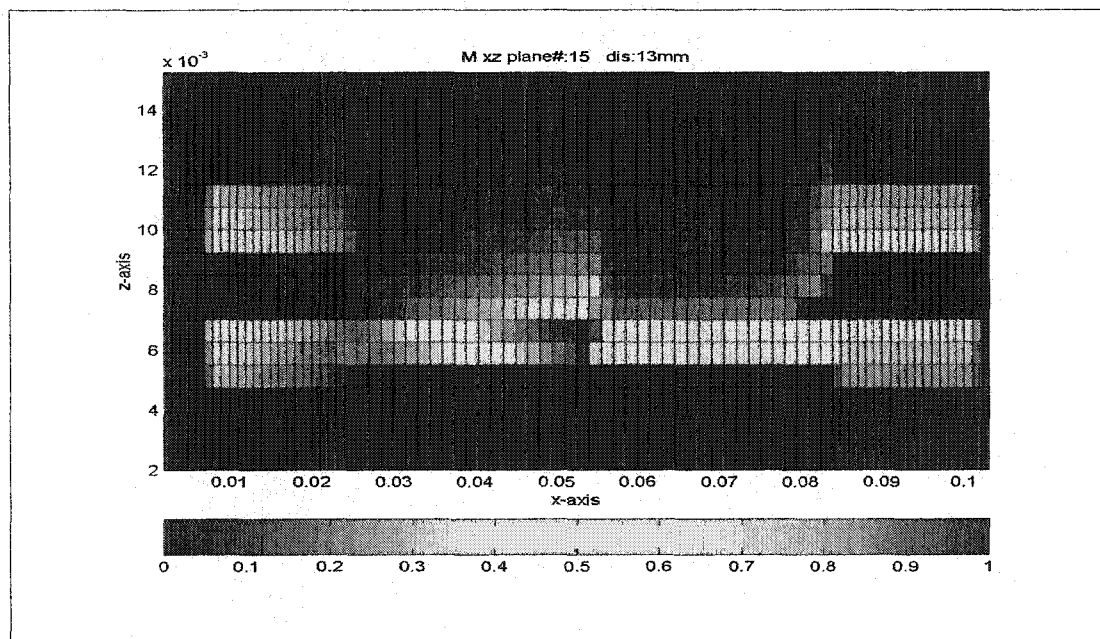


Figure 6.19: Magnetic current distribution on xy plane for capacitor (2 pF).

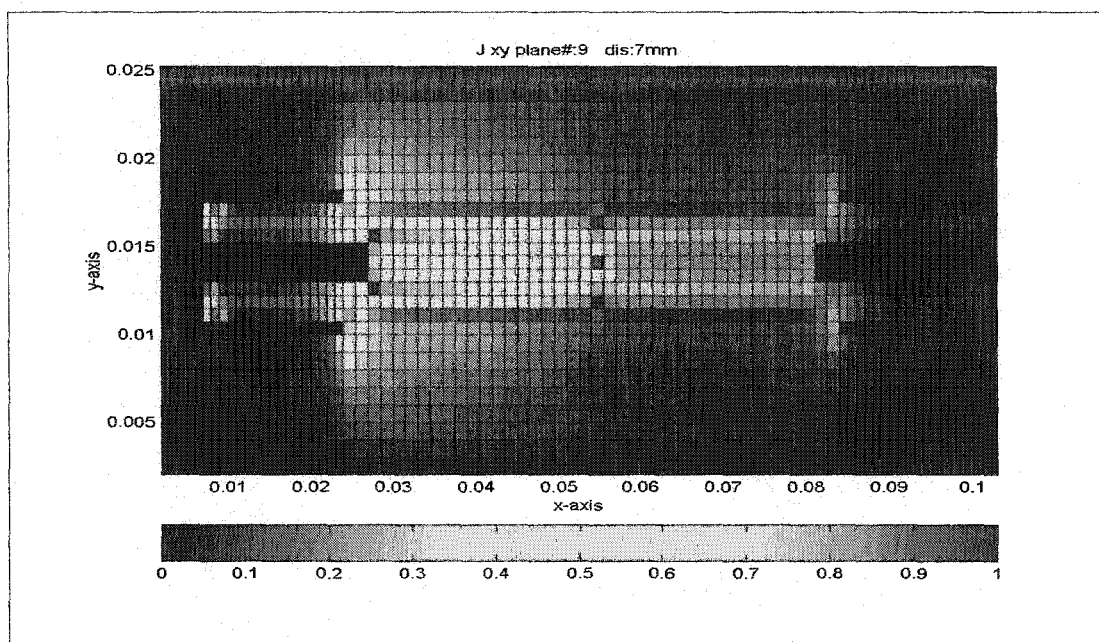


Figure 6.20: Electric current distribution on xz plane for capacitor (2 pF).

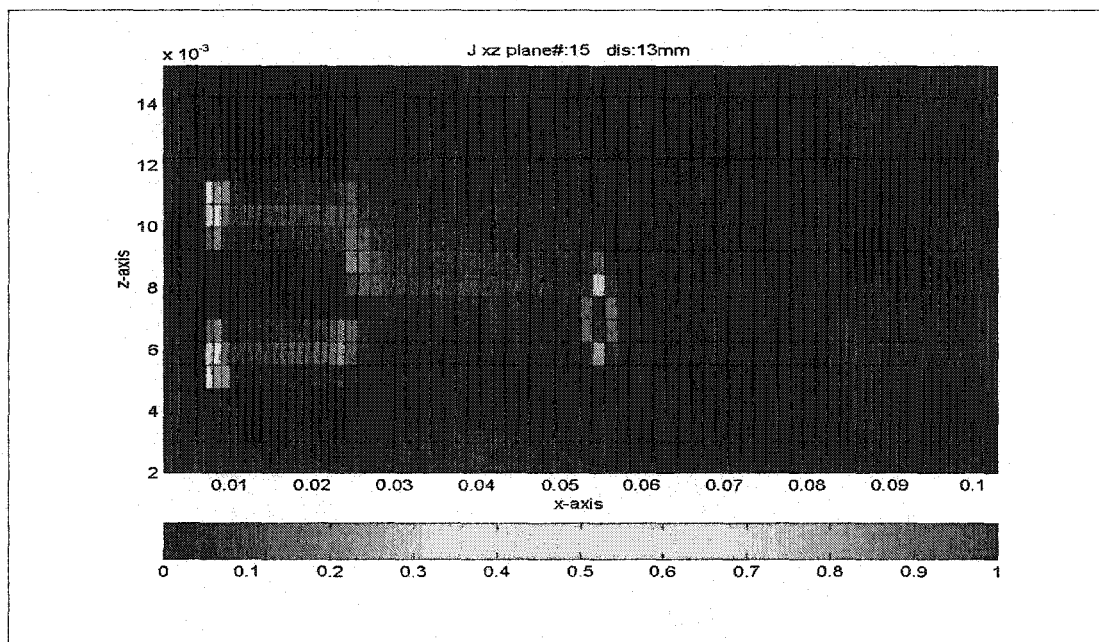


Figure 6.21: Magnetic current distribution on xz plane for capacitor (2 pF).

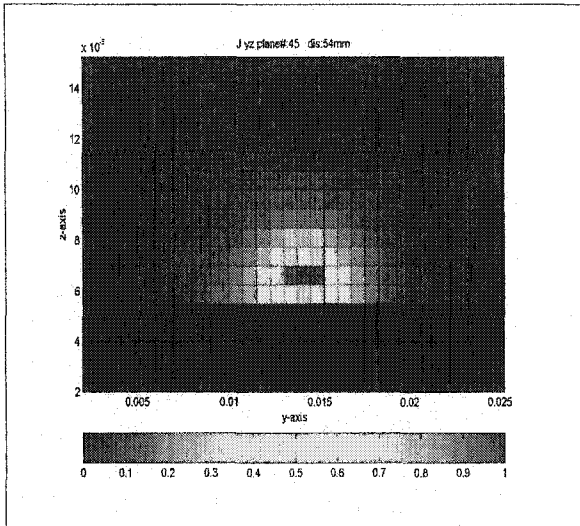


Figure 6.22: Magnetic current distribution on yz plane (#10) for capacitor (2 pF).

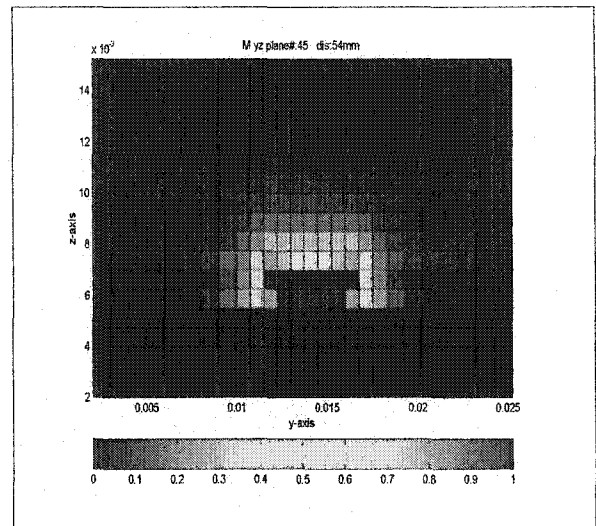


Figure 6.23: Electric current distribution on yz plane (#10) for capacitor (2 pF).

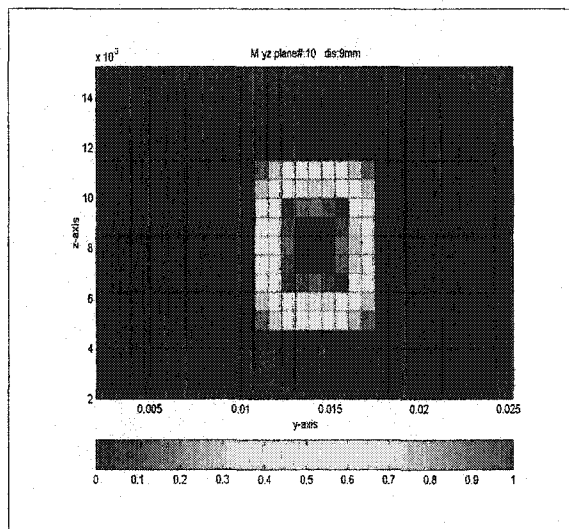


Figure 6.24: Electric current distribution on yz plane (#45) for capacitor (2 pF).

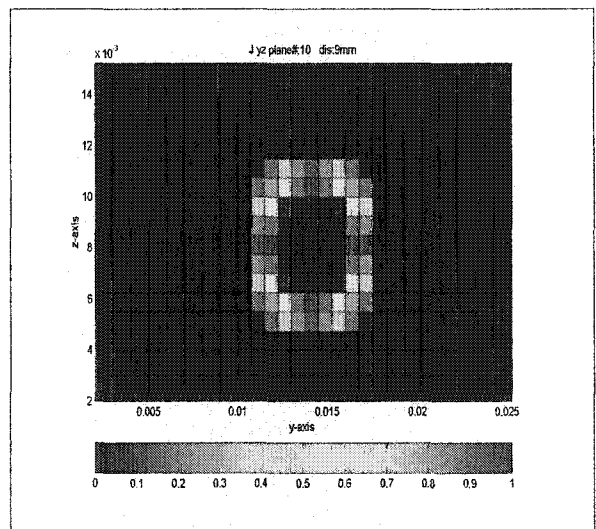


Figure 6.25: Magnetic current distribution on yz plane (#45) for capacitor

6.4 Comparison between Single and Dual Source Excitation

As discussed in Section 6.1, in our scheme of implementing the device equation in FDTD simulation, each contact point of the device (see Figure 6.1) contains an excitation source. With this new scheme, the stability of the FDTD algorithm is unchanged, and we demonstrate this using FDTD simulation with an example that contains a capacitor in a microstrip line. The simulation is with a capacitor of value 2 pF and the two cases of simulation are single and dual source excitation. The Figure 6.26 shows the top view of the two simulation cases; one is with non-uniform mesh and two excitation sources and the other is uniform mesh with single excitation source. For the dual source point simulation, a non-uniform mesh with the ratio of size between the adjacent cell of as high as two was used, and the same physical dimension of the capacitor is maintained for both cases. These simulation results are compared to measurement data and are contained in Figures 6.27 and 6.28.

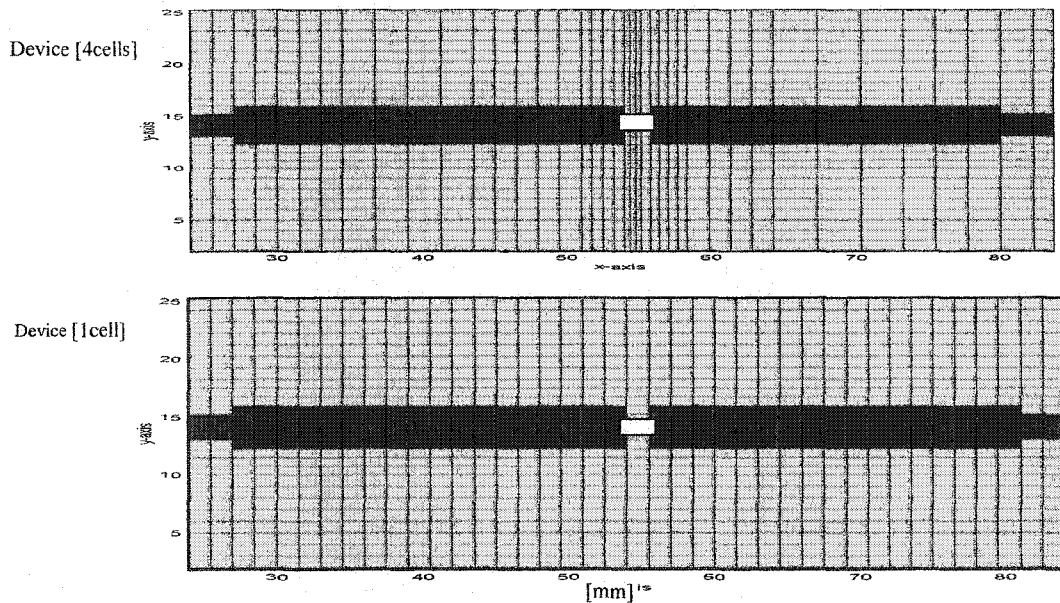


Figure 6.26: The planar view of two different cases for simulation with 2 pF capacitor.

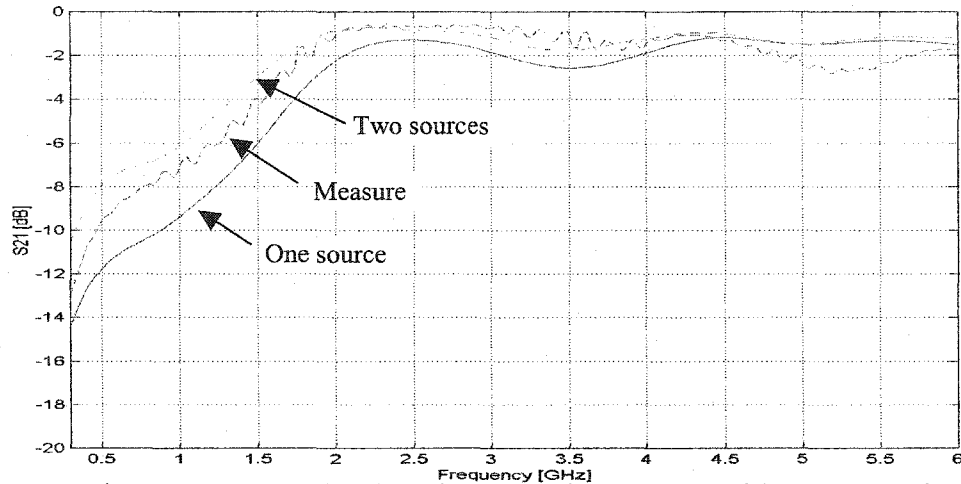


Figure 6.27: Insertion loss for the different cases with 2 pF capacitor.

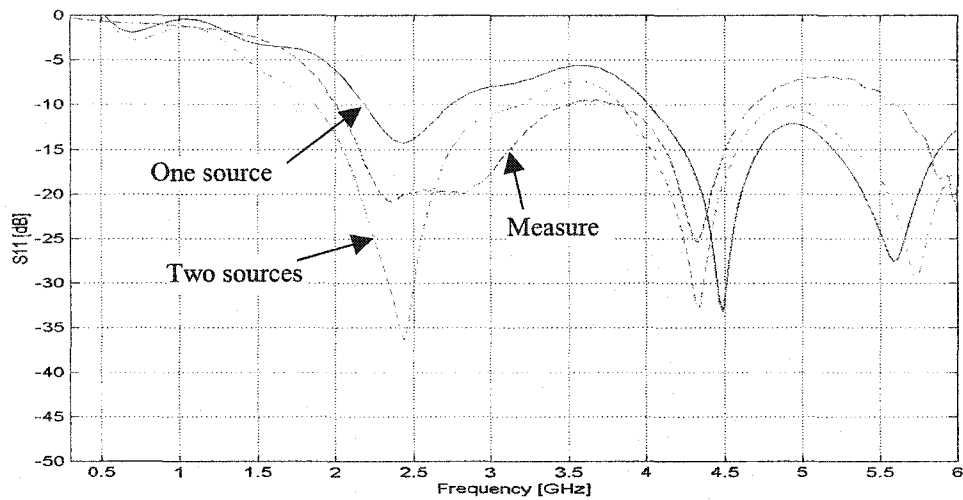


Figure 6.28: Return loss for the different cases with 2 pF capacitor.

The simulation and measurement of return and insertion loss for these the two different conditions are shown in Figure 6.27 and 6.28. In these figures, the corresponding curves for different cases are labeled. For the simulation of dual source excitation we chose a worst case, the device was modeled with sixteen non-uniform cells. The simulation and measurement results are in good agreement even under this worst case, and this proves the validity of the new scheme.

6.5 Summary

In this chapter, the application of the FDTD technique to active and passive devices was presented and a few simple circuit simulations were carried out to demonstrate its effectiveness. Simulation results presented in this chapter show very close agreement with measurement results. The simulation results include examples of passive and active devices, and the simulations demonstrate the stability of the FDTD algorithm with device equations. In addition, this chapter includes the new type of implementation using double-source point excitation for devices, which facilitates accurate simulation of larger packaged devices in high-speed integrated circuits. In order to contain the scope of this thesis, many other possibilities and simulations have been left for future work in this area.

6.6 References

- [1] Piket-May, M. J., A. Taflove, and J. Baron, "FD-TD modelling of digital signal propagation in 3-D circuits with passive and active loads," *IEEE Trans. Microwave Theory and Techniques*, vol. 42, pp.1514-1523, 1994.
- [2] Ko, W.L., and R. Mittra, "A combination of FD-TD and Prony's methods for analysing microwave integrated circuits," *IEEE Trans. Microwave Theory and Techniques*, vol. 39, pp.2176-2181, 1991.
- [3] Becker, W. D., P. H. Harms, and R. Mittra, "Time-domain electromagnetic analysis of interconnects in a computer chip package," *IEEE Trans. Microwave Theory and Techniques*, vol.40, pp.2155-2163, 1992.
- [4] Sui, W., D.A. Christensen, and C. H. Durney, "Extending the two-dimensional FD-TD method to hybrid electromagnetic system with active and passive lumped elements," *IEEE Microwave and Guided Wave Letters*, vol. 40, pp.141-143, 1992.

Chapter 7

Conclusion

In this thesis, we have demonstrated the effectiveness of the FDTD techniques when applied to microwave device analysis. This is achieved mainly by reducing the computer memory requirement and by improving the accuracy of the technique. The reduction in computer memory is achieved with techniques including 1) the use of non-uniform FDTD algorithm, 2) the use line-of-sight equivalence principle and 3) by incorporating the feed structure into the computational domain. The accuracy is improved by using appropriate mesh scaling and by incorporating device equations into the FDTD algorithm with dual-source excitation. All analyses were carried out on practical problems and they are supported with simulation and measurement results. The measurement results were in good agreement with simulation results, thus leading to the conclusion that all stipulated theories are accurate. In addition to the device analysis, new antennas were developed for the application in PCS. As the final product of the thesis work a simulation tool was developed.

The simulation tool includes all the enhancements to the FDTD technique developed in this thesis and it has a user-friendly interface developed on a commercially available platform. This simulation tool can be used in the analysis of microwave devices such as antennas, passive and active integrated circuits. The current version of the simulation tool is at the initial stage of the development and will be improved with later releases.

The “Line-Of-Sight” approach to the equivalence principle introduced in this thesis has addressed a major shortfall in FDTD technique; the computational time requirement for

radiation pattern calculation, this is reduced to one sixth of the standard equivalence. With LoS approach one can carryout antenna pattern synthesis, that has eluded the FDTD simulation. This principle can also be applied to a variety of problems outside the domain of the FDTD technique.

In this thesis, four new antennas that have applications in telecommunication industry were presented. The Coupled Patch Antenna was designed for a product developed at Research In Motion. The Printed Sleeve Antenna, the Window Antenna, Sandwich Antennas are for general applications in PCS and due to their unique physical characteristic and good performance they will become useful in the wireless industry. In the antenna analysis, the use of non-uniform FDTD and the incorporation of the feed structure, allowed the modelling of physical structure with a smaller number of cells, thus improving the efficiency. In addition, the use of new equivalence principle and PML absorbing boundary condition made the FDTD technique more effective.

In order to examine the increased error due to non-uniform mesh in the FDTD technique a detailed error analysis was carried out in this thesis. It was shown that the non-uniform FDTD algorithm exhibited global second-order accuracy that is similar to the uniform FDTD algorithm. Also, in the error analysis some special considerations needed in mesh generation for better accuracy were outlined and supported with simulation.

In the application of FDTD technique to microwave devices, a new type of implementation of using two excitation source points was introduced and the validity of this technique was tested. All the basic electronic components in microwave device gave very stable results when used in the FDTD algorithm. The simulation results of devices used as examples in the thesis were in very good agreement with the measurement results thus further solidifying the usefulness of the FDTD technique in device analysis.

In this thesis, a good balance between theoretical and experimental investigation into the application of the FDTD technique was presented. With this, the FDTD technique has been taken to a higher level in EM simulations.